Neurovascular coupling in the healthy and inflamed brain

By

Marek Lech Kowalski Allen, MSc

A Thesis submitted to the School of Graduate Studies
in Partial Fulfilment of the Requirements for the Degree
Doctor of Philosophy
Cardiff University

Doctor of Philosophy (2016) Cardiff University
(Psychology) Cardiff, Wales
TITLE: Neurovascular coupling in the healthy and inflamed brain
AUTHOR: Marek L.K. Allen, MSc
SUPERVISORS: Prof. Richard G. Wise, Dr. Valentina Tomassini
NUMBER OF PAGES: 15 (Roman),175 (Arabic)

Declaration form

The following declaration is required when submitting your PhD thesis under the University's regulations.

Declaration

This work has not previously been accepted in substance for any degree and is not concurrently submitted in candidature for any degree.

. . . .
Candidate Date

Statement 1
This thesis is being submitted in partial fulfilment of the requirements for the degree of PhD.

. . . .
Candidate Date

Statement 2
This thesis is the result of my own independent work/investigation, except where otherwise stated. Other sources are acknowledged by explicit references.

. . . .
Candidate Date

Statement 3
I hereby give consent for my thesis, if accepted, to be available for photocopying and for inter-library loan, and for the title and summary to be made available to outside organisations.

. . . .
Candidate Date

Statement 4: Previously approved bar on access
I hereby give consent for my thesis, if accepted, to be available for photocopying and for inter-library loans after expiry of a bar on access previously approved by the Graduate Development Committee.

. . . .
Candidate Date

Acknowledgements

I would like to thank everyone who has supported me throughout my PhD. Firstly, I'd like to thank my supervisors Professor Richard Wise and Doctor Valentina Tomassini for their continued help even when two new additions to their family came along. I'm very grateful for all the help and guidance you have both given me, particularly when time was tight and deadlines were looming.

I'd like to thank everyone who helped during my scanning sessions, and were willing to stay behind to ensure I could collect as much data for my studies as possible. Without everyone at CUBRIC helping I'm not sure I'd have completed the final year.

Finally, I'd like to thank my parents for their continuous support throughout my academic career, tolerating the short tempers, hunger-induced sarcasm, and helping wherever they could. or when they could. I'd also like to thank Rosalind Scott, without whom this final writing-up year would not have been possible to complete.

Dziękuję

Summary

The structural and functional integrity of the brain relies on a close balance between the metabolic demands of neurons and supporting glia, and substrate delivery in the form of blood flow. Disruption of the communication of neural cells and vascular smooth muscle, controlling the dilation and delivery of blood to specific brain regions may exacerbate the negative consequences of neurodegenerative and neuroinflammatory conditions. However, there has been little research done to measure the relationship between neural activity and changes in blood flow, or neurovascular coupling. Disruption of neurovascular coupling could lead to hypoxic conditions in the brain, or more precisely 'virtual hypoxic' conditions. Conditions such as these, if severe enough can go on to cause apoptosis or necrosis; particularly during periods of increased metabolic stress such as inflammation.

In this thesis, I begin by exploring how cerebrovascular reactivity, the process behind normal neurovascular coupling, is affected in the neuro-inflammatory condition – multiple sclerosis (chapter 5). I use this as the basis for beginning my attempt to empirically define neurovascular coupling in the healthy brain, using non-invasive neuroimaging techniques. I begin to define neurovascular coupling in the 6th chapter, using a multiple methods of measuring neural activity and blood flow changes using a graded visual task in MEG and fMRI environments. In the 7th chapter I focus on refining this protocol, and assess the repeatability of my empirical neurovascular coupling measure. Finally, using this protocol, I examine if and how this crucial process is altered during an inflammatory disease like multiple sclerosis.

List of abbreviations

20-HETE	20-Hydroxyeicosatetraenoic acid
25FW	25 Foot walk
9HPT	9 Hole Peg Test
AD	Alzheimer's Disease
ALS	Amyotrophic Lateral Sclerosis
AMPA(r)	α-amino-3-hydroxy-5-methyl-4-isoxazolepropionic acid (receptor)
ANOVA	Analysis of Variance
ASL	Arterial Spin Labelling
ATP	Adenosine Triphosphate
BBB	Blood Brain Barrier
BH	Breath Hold
BOLD	Blood Oxygenation Level Dependent
CBF	Cerebral Blood Flow
CBV	Cerebral Blood Volume
CIS	Clinically Isolated Syndrome
CMRO2	Cerebral Metabolic Rate for Oxygen
CNS	Central Nervous System
CRP	C-Reactive Protein
CSF	Cerebrospinal Fluid
CVR	Cerebrovascular reactivity
DIS	Disseminated in Space
DIT	Disseminated in Time
DMD	Disease Modifying Drugs
DMF	Dimethyl Fumarate
DMT	Disease Modifying Treatment
EAE	Experimental Autoimmune Encephalitis
EC	Endothelial Cell
ECOG	ElectroCorticography
EDSS	Expanded Disability Score
EEG	Electroencephalography
EET	Epoxyeicosatrienoic
eNOS	Endothelial Nitric Oxide Synthase
EPI	Echo Planar Imaging
EPSP	Excitatory Postsynaptic Potential
ERF	Event Related Field
ERP	Event Related Potential
ERS	Event Related Synchronisation
ET-1	Endothelin-1
ETaR	Endothelin Receptor A
ETbR	Endothelin Receptor B

EtCO2	End Tidal CO2
FA	Fractional Anisotropy
FSPGR	Fast Spoiled Gradient Echo
fMRI	Functional Magnetic Resonance Imaging
FOV	Field of View
GA	Glatiramer Acetate
Gd	Gadolinium
GLM	General Linear Model
GM	Grey Matter
GRE	Gradient Echo
Hb	Haemoglobin
HLA	Human leukocyte Antigen
HRF	Haemodynamic Response
ICC	Intraclass Correlation Coefficient
IFN-β	Interferon Beta
IFN-γ	Interferon Gamma
IgG	Immunoglobulin G
IL	Interleukin
iNOS	Inducible Nitric Oxide Synthase
LFP	Local Field Potential
MAb	Monoclonal Antibody
MEG	Magnetoencephalography
mGluR	Metabotropic Glutamate Receptor
MRI	Magnetic Resonance Imaging
MS	Multiple Sclerosis
nAM	Nano-Amp Meters
NAWM	Normal Appearing White Matter
NMDA(r)	N-methyl-D-aspartate (receptor)
nNOS	Neuronal Nitric Oxide Synthase
NO	Nitric Oxide
NOS	Nitric Oxide Synthase
ON	Optic Neuritis
NVC	Neurovascular Coupling
PASAT	Paced Audio Serial Addition Test
PASL	Pulsed ASL
PET	Positron Emission Tomography
PGE	Prostaglandin
PICORE	Proximal Inversion with Control for Off Resonance Effects
PING	Pyramidal-Interneuron Gamma
PPMS	Primary Progressive MS
QUIPSS II	Quantitative Imaging of Perfusion using Single Subtraction version 2

RETROICOR	Retrospective Correction of Physiological Motion Effects
RF	Radio Frequency
ROI	Region of Interest
ROS	Reactive Oxygen Species
RRMS	Relapsing Remitting MS
S1P	Sphingosine-1-Phosphate
SAM	Synthetic Aperture Magnetometry
SE	Spin Echo
SNR	Signal to Noise Ratio
SPMS	Secondary Progressive MS
SQUID	Superconducting Quantum Interference Device
TBSS	Tract Based Spatial Statistics
TE	Time to Echo
TNF-α	Tumour Necrosis Factor-a
T-VEF	Transient VEF
TR	Time to Repetition
VBM	Voxel Based Morphometry
VEF	Visual Evoked Field
VEP	Visual Evoked Potential
VSMC	Vascular Smooth Muscle Cell
WI	Weighted Image
WM	White Matter

Contents

Chapter 1: General Introduction

The structural and functional integrity of the brain relies on the close balance between energy demands and substrate delivery in the form of blood flow. While the energy demands of the brain are extremely high, there is little capacity for energy storage. Therefore, increases in neuronal activity must be matched with local increases in cerebral blood flow (CBF), referred to as functional hyperaemia. The link between changes in neuronal activity and associated increases in CBF is termed neurovascular coupling (NVC) and underlies the functional hyperaemic response. It is not just blood flow to be affected by changes in neuronal activity. Vessel dilation also leads to a change in cerebral blood volume, which is known to have an impact on certain MRI measures used to investigate blood flow; particularly Blood Oxygenation Dependent (BOLD)-weighted imaging. Decoupling of NVC has been seen in both acute and chronic conditions such as stroke and Alzheimer's disease (AD). There is a large body of evidence investigating how blood flow and neuronal responses are characterised in healthy adults and in pathological states. However, in humans what is often called neurovascular coupling is rarely more than task-induced increases in blood flow, or coupling a neuronal measure with blood flow changes at a single stimulus intensity. In vivo work using invasive murine or primate test subjects have been able to establish more representative measures of NVC, but which vary depending on the method of measuring neuronal activation (i.e. local field potentials (LFP) vs. spike recording). The work presented here aims to provide a non-invasive method for determining NVC in humans across a wide stimulus intensity, and to demonstrate how this can be affected in an inflammatory disease state such as multiple sclerosis.

In this thesis, I aim to obtain BOLD- and perfusion-weighted images using MRI and magnetoencephalography (MEG) to measure CBF and neuronal activation, to assess the relationship between these two modalities in humans. The motivation behind this stems from an initial study using data collected from the Sapienza Institute in Rome, and described in chapter 5, suggesting an alteration to cerebrovascular reactivity (CVR) in an inflamed brain. This study also revealed a difference in the vascular reactivity of patients demonstrating acute inflammation, who were noted to have increased vascular reactivity compared to healthy controls. Patients without acute

inflammation, however, were found to have a larger reduction in their vascular reactivity compared to controls. I will determine the extent NVC is altered using a visual task known for eliciting graded neural, and blood flow responses.

Chapter 2 contains an overview of both the gross pathophysiology of multiple sclerosis, its clinical presentations, along with an overview of the molecular markers and histological alterations found in both living and post mortem tissues. The aim is to provide some background to the disease, along with allowing some conclusions to be drawn from any alterations in vascular reactivity or NVC that might be seen later in this thesis.

Chapter 3 provides an overview of cerebral vascular architecture, the components of the neurovascular unit, and finally explaining the molecular mechanisms underlying the communication between neurons and blood vessels. The overall aim here is to give some background to the principles of cerebrovascular reactivity and neurovascular coupling, as these are the two mechanisms I focus on in this thesis. I also want to demonstrate the complexity of the signalling mechanisms between neural tissue and blood vessels to illustrate what can be disrupted during a pathological process like inflammation.

The experimental imaging methods used in this thesis are summarised in chapter 4. The two process of measuring blood flow using Blood Oxygenation Level Dependent (BOLD) contrast and arterial spin labelling (ASL) – for a qualitative or semi quantitative, and quantitative means of assessing blood flow respectively – are explained here. This chapter also covers the principles of magnetoencephalography (MEG) and how it is used for measuring neuronal activation, via evoked responses and neuronal oscillations as well as describing the mechanisms behind these measures.

In chapter 5 using data collected from the Sapienza Institute in Rome vascular reactivity is investigated in multiple sclerosis, along with the effects the administration of anti-inflammatory disease modifying treatments has in restoring the vasodilatory response to CO_2. This chapter underlies the rationale behind the need to search for a reliable measure of NVC. Attempting to determine if and how coupling

between neurons and blood flow is affected in disease states would provide extra insight into the efficacy of new treatment options, as well as possibly allowing for a new measure of disease activity.

Establishing and refining the protocol for measuring NVC is provided in chapters 6 and 7. An initial pilot is described in chapter 6, with chapter 7 aiming to build and refine the protocol, along with testing the new measure's repeatability. In chapter 6, two stimuli are used; a reversing checkerboard and a moving grating. Both are shown in MEG and fMRI settings at 6 contrast levels. In MEG, the reversing checkerboard is used to gather visual evoked field (VEF) responses, whereas the grating was used to elicit gamma oscillatory event related synchronisations (ERS). During the MR sessions, BOLD- and perfusion-weighted images were collected to assess cerebral blood flow responses (CBF). Regression is used to compare neural signals recorded in MEG to CBF responses for each task, with the aim being to empirically define neurovascular coupling.

Chapter 7 contains a refinement of this protocol, where the focus shifts to comparing VEF responses to gamma oscillatory power, and BOLD weighted images to ASL data for neural and blood flow measures respectively. Only one stimulus is used here, with a wider range of intensities to allow for a full characterisation of the NVC response. I also assess the repeatability of each component used in defining NVC, as well as the repeatability of the measure overall.

Without ensuring the repeatability of a measure it would have no clinical or research benefits. If variability of a response can be confounded with an uncontrollable variable such as time, diminishes the ability of comparing results between cohorts or study groups.

Chapter 8 is the final experimental chapter, where I apply the NVC protocol from chapter 7 to multiple sclerosis patients. Here I aim to establish the extent to which NVC is altered in this disease state by comparing patients' results to healthy volunteers. More specifically, I investigate the changes in gamma oscillatory power between healthy volunteers and patients, as well as BOLD and ASL-based CBF measures. Finally, a comparison is made between the overall NVC measure in healthy volunteers and patients.

The final chapter contains a summary of the results and findings of this thesis. Further developments are also discussed with further refinements to the NVC protocol and experimental design used in chapters 7 and 8.

Chapter 2: Multiple Sclerosis

2-1 Introduction

Multiple sclerosis (MS) is an autoimmune demyelinating disease, first described by French neurologist Jean-Martin Charcot in 1868[1]. The disease typically starts to present in the second and third decade of life, with a 2:1 ratio of women to men being affected[2]. While women are more likely to present with MS, the disease progression in men tends to be faster and more aggressive[3,4]. This disparity between the sexes only appears to occur in youth. Once over 50 years old, affliction rates tend to remain equal between men and women.

2-2 Symptoms

As MS is a demyelinating disease of the central nervous system (CNS), it is characterised histologically by a loss of the fatty myelin sheath that wraps around and protects neurons. Loss of myelin on T1 weighted scans shows as dark "holes" in the normally appearing white matter[5] (fig. 2-1). The main functions of myelin are the increased conduction speed of action potentials down axons, which is achieved by allowing action potentials to be propagated via salutatory conduction (fig. 2-2), the increased efficiency by reducing energy demands from repeated axonal firing and the protection of axons[1,6].

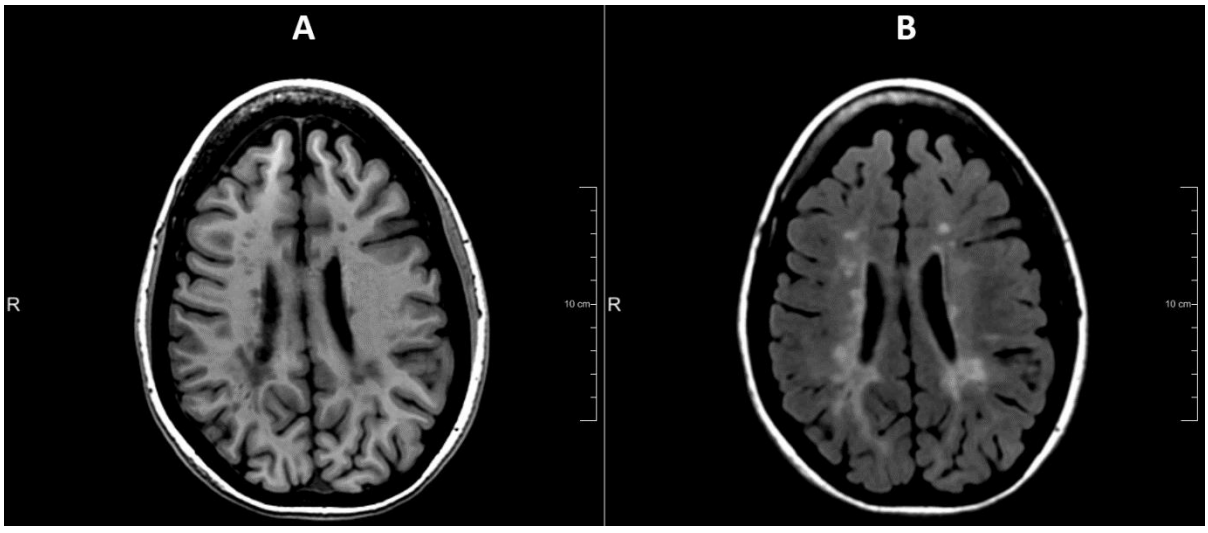

Figure 2-1 MRI showing lesions in a brain afflicted with MS. A) T_1 weighted scan showing dark "holes" in the white matter indicative axonal loss. B) A FLAIR image of the same patient showing larger volumes and numbers of lesions than the T_1 scan. Image taken from http://www.diagnijmegen.nl/images/d/db/Mriwebsite.png

The symptoms of MS are varied, ranging from visual and sensory disturbances, motor and sphincteric dysfunction, cognitive impairment and mood-related disorders. However, in many cases symptoms can appear and disappear along with 'relapses' of the disease. This is characterised clinically by a the development of new symptoms or the sudden worsening or recurrence of pre-existing ones[7]. Investigation of patients undergoing a relapse usually show an increase in circulating inflammatory markers, as well as an increase in the volume or number of lesions present on an MRI[7–9]. Normally the meninges, or blood-brain-barrier (BBB) provide an impermeable layer to large molecules and circulating cells through the use of tight interlocking epithelial cells. Breakdown of the connecting junctions during relapses leads to increased permeability of the BBB and allows diffusion of inflammatory molecules and other immune cells into the delicate environment of the CNS[10–12].

Gadolinium (Gd) is used as a contrast agent to assess the structural integrity of the BBB. As BBB

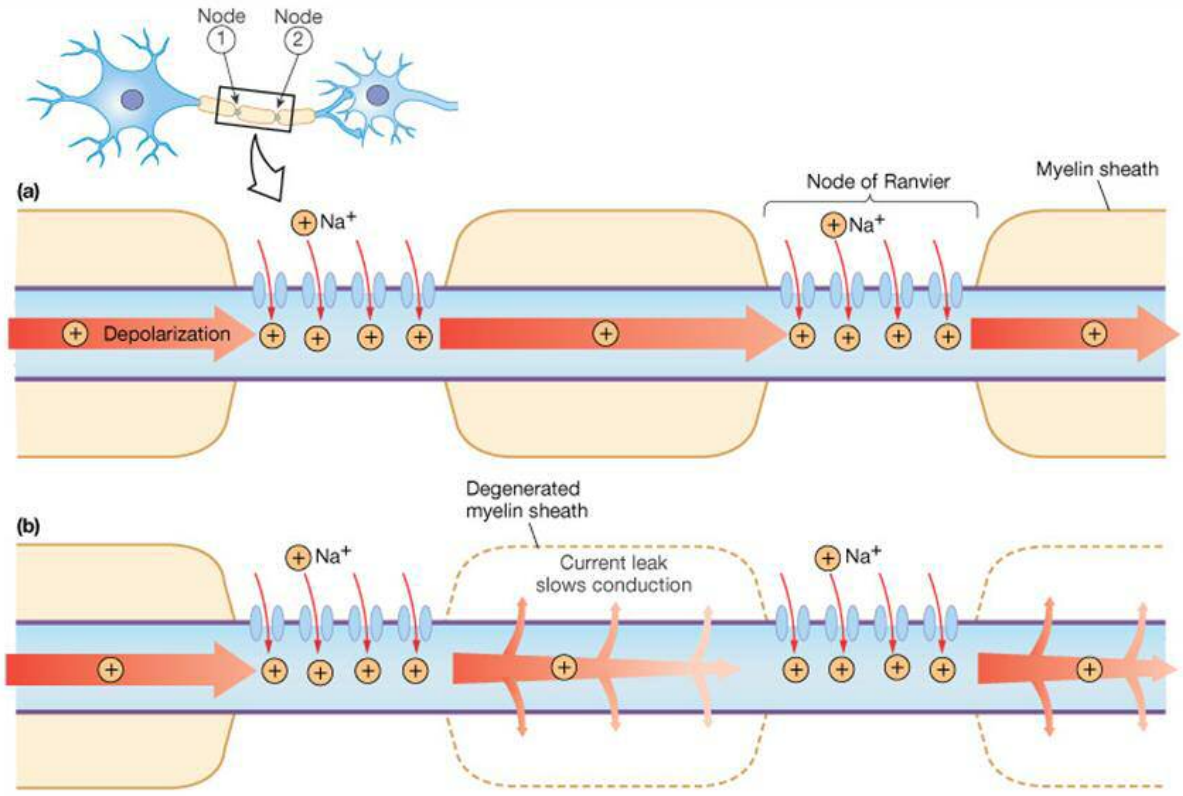

Figure 2-2 Schematic example of saltatory conduction. A) Influx of sodium ions (Na^+) depolarise the first node of Ranvier, myelin prevents any leak of Na^+ extracellularly allowing efficient diffusion to the next node. Movement of Na^+ causes an increase in the membrane potential, enough to trigger the activation of voltage gated sodium channels (Na_v) causing full depolarisation and propagation of the action potential. B) Loss of the myelin sheath slows conduction speed. The presence of Na^+/K^+ ATPases causes 'leakage' of Na^+ extracellularly meaning the time taken for sufficient diffusion of Na^+

permeability increases, intravenously injected Gd will diffuse into any sites of active inflammation in

the CNS and show as the hyper-intense lesions seen in fig.2-1b. Following cessation of the acute inflammatory attack the BBB can repair itself and reduce its permeability back to normal levels. Therefore, Gd only shows the presence of new sites of inflammatory activity, rather than all lesions present through the CNS. It is still unknown what causes the breakdown of the BBB, whether the slightly elevated levels of inflammation damages the epithelial layers, causes a positive feedback loop leading to more inflammation and injury, or if an external stimulus causes the damage, leading to the inflammation.

As the disease progresses, patients present with increasing physical and cognitive disabilities. In addition, disturbances such as depression, mental and physical fatigue, sleep disturbances and pain are also common[4,13,14].

The Kurtzke expanded disability score (EDSS) is used clinically to score disability of MS patients on a scale from 1-10. Scores below 6.0 represent patients who are still ambulatory[14,15]. These patients tend to present with:

- Stiffness or weakness in the limbs
- Sensory disturbances (numbness or tingling, as well as visual or auditory alterations)
- Ataxia (lack of coordination of voluntary muscle groups, arising from dysfunction in the nervous system rather than within the muscle itself).
- Problems with speech or swallowing
- Bowel or bladder dysfunction

Above 6.0, patients require assistance with day-to-day walking. While this test has often been criticised for its overreliance on walking as a measure of disability, it is still commonly used clinically.

2-3 Clinical courses

Initial presentations of MS are referred to as clinically isolated syndromes (CIS). For a diagnosis of MS to be made, the MacDonald criteria are often used:

- ≥ 2 attacks must be present, either evidence of 2 new lesions, or 1 lesion and historical evidence of another attack.
- ≥2 attacks and clinical evidence of 1 lesion
- 1 attack and clinical evidence of ≥2 lesions
- For a diagnosis of primary progressive MS, a follow up period of 1 year in which constant disease progression must be present.

However, revisions suggested by Polman et al. (2011) are now commonly used. The key points here are that a dissemination of both time (DIT) and space (DIS) of lesion presence i.e. new lesions must

Clinical Presentation	Additional Data Needed for MS Diagnosis
≥2 attacks ; objective clinical evidence of ≥2 lesions or objective clinical evidence of 1 lesion with reasonable historical evidence of a prior attack	None
≥2 attacks ; objective clinical evidence of 1 lesion	Dissemination in space, demonstrated by: ≥1 T2 lesion in at least 2 of 4 MS-typical regions of the CNS (periventricular, juxtacortical, infratentorial, or spinal cord) ; or Await a further clinical attack implicating a different CNS site
1 attack ; objective clinical evidence of ≥2 lesions	Dissemination in time, demonstrated by: Simultaneous presence of asymptomatic gadolinium-enhancing and nonenhancing lesions at any time; or A new T2 and/or gadolinium-enhancing lesion(s) on follow-up MRI, irrespective of its timing with reference to a baseline scan; or Await a second clinical attack
1 attack ; objective clinical evidence of 1 lesion (clinically isolated syndrome)	Dissemination in space and time, demonstrated by: For DIS: ≥1 T2 lesion in at least 2 of 4 MS-typical regions of the CNS (periventricular, juxtacortical, infratentorial, or spinal cord) ; or Await a second clinical attack implicating a different CNS site; and For DIT: Simultaneous presence of asymptomatic gadolinium-enhancing and nonenhancing lesions at any time; or A new T2 and/or gadolinium-enhancing lesion(s) on follow-up MRI, irrespective of its timing with reference to a baseline scan; or Await a second clinical attack
Insidious neurological progression suggestive of MS (PPMS)	1 year of disease progression (retrospectively or prospectively determined) plus 2 of 3 of the following criteria : 1. Evidence for DIS in the brain based on ≥1 T2 lesions in the MS-characteristic (periventricular, juxtacortical, or infratentorial) regions 2. Evidence for DIS in the spinal cord based on ≥2 T2 lesions in the cord 3. Positive CSF (isoelectric focusing evidence of oligoclonal bands and/or elevated IgG index)

Figure 2-3 Changes to the MacDonald criteria as suggested by Polman et al. (2011). The main additions relate to the need for a dissemination of lesion presence in both time and space. As other neurological disorders present in a similar manner to MS, in order for a diagnosis of MS to be made Polman suggests that new lesions must present in a different are of the CNS than current, or historical lesions have done. If new lesions present in follow up scans compared to baseline, this is classified as a dissemination in time. Image adapted from Polman et al. (2011).

present in different areas of the CNS or present during a follow up MRI scan compared to a baseline. Gadolinium is used as a contrast agent as it highlights areas of blood brain barrier (BBB) breakdown[15]. The revisions suggested by Polman et al. (2011) are shown in fig 2-3. Numbers of patients presenting with CIS going on to develop MS vary: anywhere between 30% to 70% of CIS patients have been reported to progress to MS[16,17].

There are 2 main ways of categorising MS, which can then be divided further into subcategories according to the revisions put forth by Lublin et al. 2014[18] and summarised in fig 2-4:

2-3-1 Relapsing remitting

Relapsing remitting MS (RRMS) is the most common form of MS. The name refers to the nature of patients exhibiting 'relapses'. Patients experience 'relapses', characterised by either worsening of existing symptoms or the presentation of new ones. These attacks then can go into remission with either a lessening of symptoms back to a level comparable to before the relapse, or disappearing altogether.

It is thought that the relapsing-remitting nature of this type of MS represents remyelination of damaged axons[19]. Other theories include adaptation of the brain to cope with myelin/neuronal loss, or just the removal of the inflammatory attack allows at least partial restoration of brain function[20]. Disease modifying treatments aimed at reducing inflammation have, in many cases, been shown to lengthen the time taken from initial CIS to full MS, or prevent it altogether[1,17,21]. RRMS can be divided into two categories – active, and non-active. Activity is determined by either clinical relapses or the addition of new or enlarging contrast-enhancing T_2 MRI lesions when assessed annually[18] (fig. 2-5).

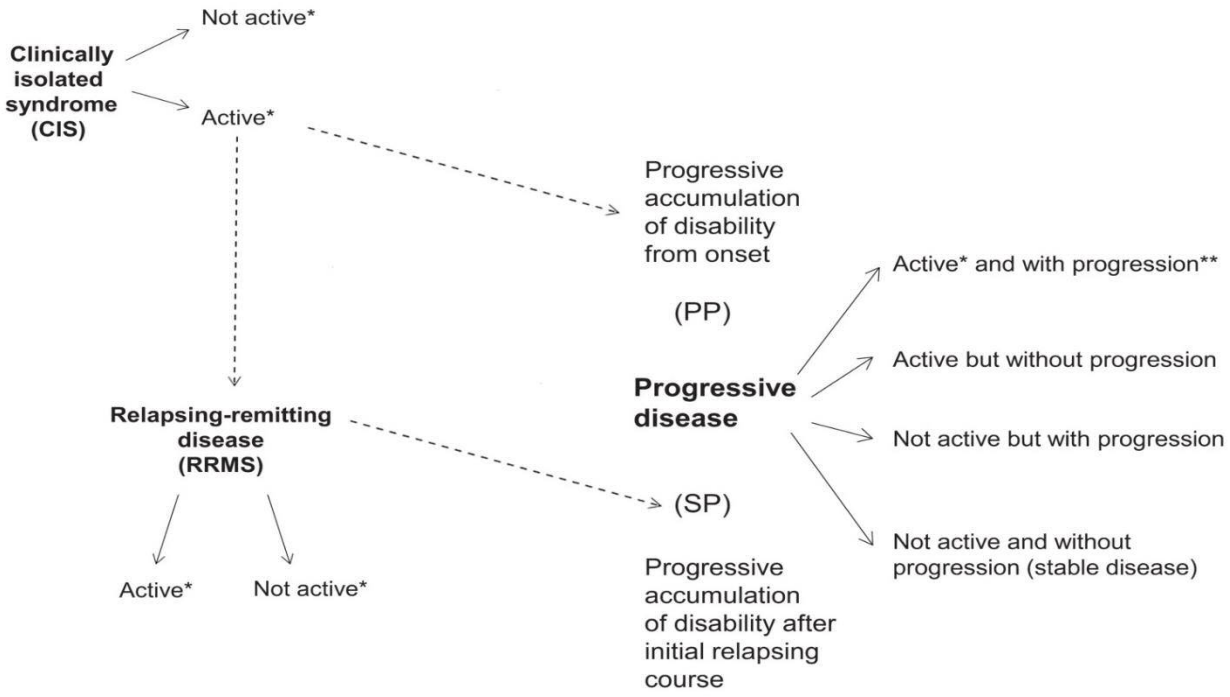

Figure 2-4 Schematic of disability progression in the two most common forms of MS. In relapsing remitting MS (RRMS) a pre-clinical period contains a clinically isolated syndrome precedes a period of relapses characterised by worsening of disability, or presentation of new symptoms associated with MS, followed by a remission. This is when patients are typically presented with treatment options. Disease modifying drugs/treatments (DMD/Ts) are used which take the form of interferon-β, glatiramer acetate, oral treatments or monoclonal antibodies. The RRMS stage can last from years to decades, 65% of patients form secondary progressive forms of the disease (SPMS), where the disease progresses, sometimes with relapses, but remissions do not result in a disappearance of symptoms like in the early phases of RRMS. Image modified from[167].

2-3-2 Progressive MS

Progressive MS is the second category MS phenotypes can take, which is broadly split into primary and secondary progressive forms. These are further split to define the disease activity and progression; these are summarised in fig. 2-4.

2-3-2-1 Secondary progressive

Defined as the progressive accumulation of symptoms or disability after a period of an initial relapsing phenotype. 65% of patients with RRMS will eventually move onto the secondary progressive form, about 5-7 years after CIS. Disability proceeds continuously[14,21]. It is thought that progression to SPMS represents the exhaustion in the brain's ability to repair or respond to new damage.

2-3-2-2 Primary progressive

Only 10%-20% of patients present with phenotype[14,22]. It differs from SPMS in that PPMS is not preceded by a relapsing-remitting form. As the disability progresses, continuously from the initial CIS, it is not surprising that patients with this subtype more quickly develop disability.

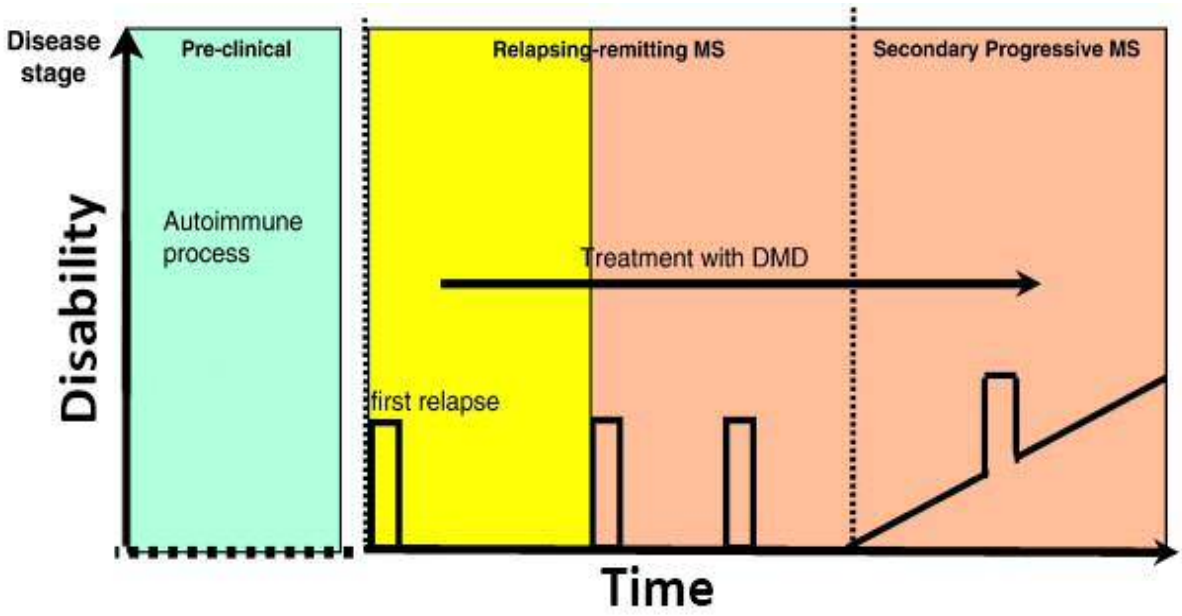

Figure 2-5 Schematic of defining MS phenotypes according to the revisions presented by Lublin et al. 2014. Active is defined as either a clinical relapse annually, or an increase in the number or size of T2 hyperintense lesions in MRI follow up scans. Progression

2-3-3 Causes

To date no single cause of MS has been found. Instead, many studies have concluded that a combination of genetic and environmental (infections, vitamin D deficiency etc.) factors. Geographically, MS is more common in northern latitudes, where lower levels of sunlight, causing decreased vitamin D level have been implicated[1,14,23]. Indeed, lower activation of vitamin D-associated genes has been linked to increased MS risk. Twin studies have noted a link between the place of birth and MS affliction rate, subjects who moved to new countries before the age of 15 had the same risk of developing MS as a subject born there[1,23,24].

Certain infections are also noted to cause an increased risk of MS. Oligoclonal bands in the cerebrospinal fluid (CSF) of patients, typical of viral infection correlated well with disease severity[13]. Several demyelinating diseases similar to MS are also known to be caused by viral infection. However, no person-person transmission has ever been proven.

As mentioned previously, a genetic factor is known to play a part. The incidence of MS rises along a family line. In non-identical twins, if one develops MS, the risk of the other also developing the disease increases by 5%. This rises to 30% in identical twins. Mutations affecting the human leukocyte antigen (HLA) on chromosome 6 have some commonality with MS diagnosis along with other autoimmune diseases. In total, mutations in 12 other genes on chromosome 6 outside of HLA also correlate highly with MS incidence.

2-4 Pathophysiology

The name multiple sclerosis means “many scars” in Latin. Histologically, the classic marker for MS has been the formation of ‘plaques’ or ‘lesions’ in the white matter. These have been found in anatomical MRI scans, where dark “holes” appear corresponding to the locations of axonal loss[25].

There have been many studies conducted surrounding the role that inflammation plays in MS. With this in mind a multitude of inflammatory markers have been shown to be elevated in MS, with the oxidative- and nitrosative-stress pathways both shown to play a role. Increases in interleukins (IL) -

1β, IL-4, IL-6 and IL-10, reactive oxygen species (ROS), nitric oxide metabolites (NO), C-reactive protein (CRP), tumour necrosis factor alpha (TNF-α) and interferon gamma (IFN-γ)[7,8,26–31].

Lymphocytes (particularly T-cells) infiltrating through a normally impermeable BBB recognise myelin as a foreign body, which must be removed. This attack on the myelin seems to start the inflammatory process that results in further BBB disruption and allows cytokines and antibodies to be released, as well as allowing other immune cells, most notably macrophages, to pass through the BBB[12]. Increased permeability of the BBB allows larger molecules to diffuse through, such as gadolinium (Gd) when contrast is administered for MRI. Gadolinium is used as a marker of BBB disruption. When used with a T_1 MRI scan Gadolinium shows bright white (hyperintense) on areas of the brain or spinal cord with enhanced BBB permeability, and therefore active inflammatory sites[5].

The mechanism through which BBB permeability first increases is still up for debate. It is unclear whether there is increased inflammation, which leads to BBB permeability, allowing infiltration of lymphocytes or whether the BBB gets damaged, causing infiltration and this leads to inflammation. MS can be characterised by two main aspects:

1. Destruction of myelin in the CNS
2. Inflammation

Which order these steps occur in is still unclear.

Myelin is key for normal neuronal function, as it allows for more efficient action potential transmission. By wrapping around axons in sections, leaving only small sections of axons exposed (nodes of Ranvier), myelin causes action potentials to propagate through salutatory conduction. This increases the speed of transmission while reducing energy demands on neurons[32]. Resting membrane potentials are maintained through the actions of a variety of channels and pumps, but the sodium/potassium ATPase (Na^+/K^+ ATPase) is by far the most numerous. It acts to remove intracellular sodium ions (Na^+_i) in exchange for extracellular potassium ions (K^+_o) against their respective

concentration gradients using the energy released through ATP hydrolysis to assist[32]. During salutatory conduction, only the nodes of Ranvier become depolarised, meaning Na^+/K^+ ATPases only need be concentrated around these sections.

Following demyelination conduction speed slows. To compensate, neurons up-regulate voltage gated sodium, potassium and calcium channels (Na_v, K_v and Ca_v respectively) along with the associated ATPases to remove the ions and restore proper resting membrane potentials[33–37]. The increased ATP demand puts a strain on neuronal mitochondria to produce more ATP to run these enzymes. It is unclear how detrimental this reduction in ATP generation is on its own, but when compounded with the effects of inflammatory mediators, a significant strain is put on normal neuronal functions.

Nitric oxide inhibits respiratory chain enzymes, reducing ATP generation and causing increases in ROS[37,38]. The increased levels of ROS help set up a positive feedback loop, as ROS increase damage of mitochondria, further inhibiting their ability to keep up with increased ATP demand. Eventually, as ATP becomes scarce, ATPases can no longer maintain appropriate concentrations of intracellular sodium ($[Na^+]_i$), potassium ($[K^+]_i$) or calcium ($[Ca^{2+}]_i$). Calcium is very important in neurotransmission, but is also toxic to cells and as such its intracellular concentration is kept under strict regulation. However, upregulation of Na^+ channels (particularly $Na_v1.6$ – known for causing large and persistent currents)[33,37] leads to large rises in $[Na^+]_i$ which cannot be cleared via the Na^+/K^+ ATPase, resulting in reversal of the Na^+/Ca^{2+} exchanger. The reversal causes large influxes of Ca^{2+}, inhibiting mitochondrial function further leading to excitotoxicity and neuronal cell death.

It has been noted that white matter lesion count, or volume correlates poorly with disability in PPMS, SPMS and to some extent RRMS. It is becoming clear that grey matter (GM) demyelination is playing a greater role in determining disease severity than canonical WM lesions volume, but has been hard to characterise using conventional MRI[4,39,40]. Techniques such as 3D-FLAIR and double inversion recovery (DIR) have proved key to demonstrating cortical lesions. RRMS tends to be characterised by WM periventricular lesions. Grey matter pathology becomes far more extensive in progressive forms

of the disease, where demyelination of axons in the cortex is met with increasing levels of perivascular and BBB inflammation[4]. As GM demyelination appears to occur more readily in primary and secondary progressive forms of MS compared to RRMS, it could be that GM pathology might instead be occurring secondary to WM damage. This is part of the 'virtual hypoxia' hypothesis proposed by Stys et al. It postulates that degradation in cortical GM may be the results from WM degeneration and inflammation combined with increased energy demand from the upregulation of Na^+ channels [31,33–35,37] (fig. 2-6). For the virtual hypoxia theory to be the sole cause of damage seen in MS, cerebral perfusion would need to be maintained. 'Traditional' hypoxia or ischaemia is where a reduction in cerebral blood supply restricts oxygen and glucose delivery to neurons. However, the virtual hypoxia theory stipulates that a normal level of blood supply is maintained to the neurons, but due to the increased energy demands imposed by the upregulation of ATPases and other ion channels glucose and oxygen delivery cannot be maintained as blood is diverted to other areas currently undergoing use.

In the early stages of MS, lesions appear to form due to a combination of low perfusion and oxidative stress. During these stages neurons exhibit an accumulation of oxidative lipids and mitochondrial injury[41–43]. Neurons that exhibit these morphological changes tend to show signs of acute injury, characterised by axonal and dendritic fragmentation and either controlled (apoptosis) or uncontrolled (necrosis) death of the neuron. These alterations tend to be found in actively demyelinating lesions, implying that in early MS at least, acute oxidative injury appears to start the demyelinating process. Another type of injury, one associated more with axonal transection is also present. This type of damage tends to appear more in areas directly overlaying subcortical demyelinating lesions[44]. Neurons showing the type of degradation associated with axonal transection tend to be localised in cortical areas and sulci, but also contain a high number of mitochondria with DNA deletions. A phenotype commonly associated with high levels of oxidative stress[45]. When damaged, mitochondria are transported to the cell body, which may amplify further damage due to electron leakage. These data imply that the formation of demyelinating lesions lead to further increases in oxidative stress and

axonal damage. The resolution of this inflammation and the removal of oxidative stress helps to partially resolve this, and could give rise to the RRMS subtype[45]. In progressive forms of MS, accumulation of oxidative damage and axonal transection could cause apoptosis or necrosis of whole neurons leading to the cortical lesions associated with disease progression and disability.

There is overwhelming evidence that cerebral blood flow is altered in MS. Several studies have reported increases in nitric oxide synthase (NOS) activity, along with increases in NO metabolites in cerebrospinal fluid (CSF). As NO is a potent vasodilator, this would point to MS patients being cerebrally hyper-perfused, which would reflect the expected hyper-perfusion of tissues during an inflammatory response. Current evidence indicates however, that MS sufferers are chronically hypoperfused, particularly in WM, as an increase in the expression of hypoxia-related genes has been noted in histological samples[46–50]. It is unclear though, whether the hypoxia-related genes are being activated due to the virtual hypoxia mechanism mentioned previously, or is instead being caused by MS patients being chronically hypoperfused.

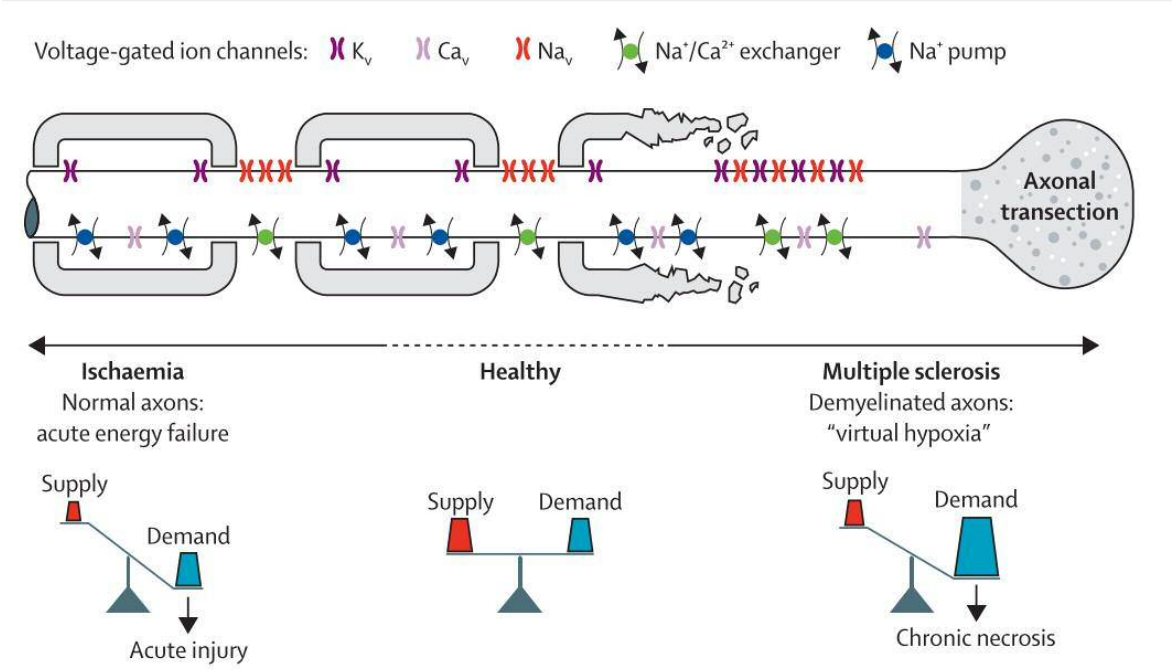

Figure 2-6 Virtual hypoxia hypothesis of multiple sclerosis. In 'normal' ischaemia, the demand for substrates such as oxygen and glucose by neurons is no different from in a healthy brain, but a reduction in blood supply causes a reduction in delivery causing hypoxia, neuronal stress and apoptosis/necrosis. In 'virtual hypoxia' demyelination leads to an upregulation of Na_v channels (particularly Na_v 1.2 and 1.6) as well as Na^+/K^+ and Na^+/Ca^{2+} ATPases. Increases in the latter lead to a vastly increased demand for ATP, glucose and oxygen. The demand cannot be met with a 'normal' supply leading to 'virtual' hypoxia, where blood flow appears unaffected but tissues remain hypoxic due to increased demand. Image taken from[34]

Endothelin-1 (ET-1) is a potent vasoconstrictor secreted by endothelial cells in response to release of TNF-α and IL-1b[47]. The actions of ET-1 are mediated through two receptors; ET-a and ET-b. ET-1 levels have been found to be increased in cerebral ischemia, traumatic brain injury and subarachnoid haemorrhages, with circulating plasma levels of ET-1 being correlated with higher incidence of stroke[51]. The vasoconstrictory effects of ET-1 are mediated through the ET-a receptor (ET-aR) found on vascular smooth muscle cells. In addition to the actions on smooth muscle cells, ET-1 also inhibits the production of NO via endothelial nitric oxide synthase (eNOS)[51,52]. Under normal circumstances tonic action of eNOS regulates blood flow through many parts of the body. However, the actions of ET-1 to inhibit eNOS activity, as well as increasing vasoconstriction of vascular smooth muscle cells (VSMCs)[51,52]. This would support the evidence that MS patients are chronically hypoperfused, with hypoperfusion exacerbating damage caused by lymphocyte infiltrations and mitochondrial dysfunction, but does not offer any explanation for the hyperperfusion seen by some studies.

Endothelial NOS is not the only producer of NO. However, two other isoforms; inducible NOS (iNOS) and neuronal NOS (nNOS) are also present in the brain, of which iNOS is of particular relevance. While ET-1 has inhibitory actions on eNOS, iNOS is unaffected and indeed some studies suggest iNOS activity is enhanced via interactions with ET-1[53,54]. TNF-α and IFN-γ - the same inflammatory cytokines that elicits production of ET-1 also stimulates iNOS, further increasing acitivity[55,56]. This means that while tonic actions of eNOS might be halted in MS, vasodilatory actions of NO produced via iNOS might still continue, and lend some explanatory mechanisms to the possible hyperperfusion seen[57].

Overproduction of NO via iNOS is not without problems. Acutely, NO severely inhibits mitochondrial function. Nitric oxide has a high affinity for the cytochrome C oxidase enzyme, where it outcompetes O_2 for binding and leads to ROS generation[37]. As NO is a highly diffusible, lipid soluble gas its half-life is usually tightly controlled through its reaction with oxyhaemoglobin (oxy-Hb) in red blood cells, where it is converted to nitrate[30,58,59]. As we have seen previously, ROS are produced as a consequence of the inflammatory response and mitochondrial dysfunction. When NO and ROS interact they

produce a powerful oxidant, peroxynitrite[52]. Under inflammatory conditions the rate of peroxynitrite production can increase up to 1,000,000-fold[30]. Luckily peroxynitrite reacts quite slowly with biological molecules, but can diffuse far from its production site. Sustained increases in peroxynitrite have been found to cause irreversible damage to mitochondria, disrupt signalling pathways and the induction of cell death through apoptosis and necrosis[37,38,52].

Neuronal activation is well known to lead to an increase in blood flow to the region being activated – known as the functional hyperaemia. Disruption here leading to hypoperfusion (through the actions of ET-1) would in the short term causes extreme stress to neurons as they are not able to respire anaerobically.

In the longer term, significant increases in peroxynitrite production would result, as insufficient levels of oxy-Hb would be available to break down NO into nitrate. Neurons already under significant strains from inflammation, mitochondrial dysfunction, and decreased oxygen and glucose delivery would be put under further pressure and lead to their death. Indeed, increases in peroxynitrite are found to be abundant in lesions of acute experimental autoimmune encephalomyelitis (EAE) animals, along with increases in both CBF and cerebral blood volume (CBV) preceding lesion formation[60–62]. This suggests that excessive NO production plays a significant part in lesion formation and disease progression. Treatments with IFN-β1a reduces NO production and slow lesion formation and disease progression[59,63].

So far I have discussed changes in neuronal activity and cerebral blood flow (CBF) individually, with no association being made between synaptic activity and functional hyperaemia. With both neurons and blood flow being affected, it would be rash to assume the link between neurons and CBF would be unaffected in this disease. It is not clear whether the basal hypoperfusion seen in normal appearing white matter (NAWM) is due to the primary actions of circulating ET-1, or if it is in fact secondary to decreased neuronal firing. Using a link between neuronal activation and changes in CBF could prove

extremely useful in improving our understanding of the pathophysiology of MS, establishing new biomarkers disease evolution and identify targets for treatments.

2-5 Treatment

As MS is an inflammatory autoimmune disease of the CNS (central nervous system), there is a limited number of approved treatments available. During acute relapses, inflammation is initially controlled using corticosteroids with the aim of limiting the inflammatory damage. Following from this, additional disease modifying treatments are available to slow disease course and aim to reduce further relapses:

- Interferon-beta 1a (IFN-β1a) and 1b (IFN-β1b)
- Glatiramer acetate
- Oral treatments (dimethyl fumarate, teriflunomide, fingolimod)
- Humanised monoclonal antibodies (hmAbs) (natalizumab, alemtuzumab)

While IFN-α and IFN-γ are both inflammatory mediators IFN-β acts to reduce inflammation through reduction of tumour necrosis factor-α (TNF-α) and interleukins-4 and -6 (IL-4 and IL-6). The interferons' efficacy has been well documented in slowing the progression from CIS to MS, as well as in reducing relapse rate in RRMS patients by 30%[64]. Unfortunately, these treatments are not particularly effective in slowing disease progression, once patients reach the secondary progressive phase, nor are they effective in treating primary progressive forms of MS.

Glatiramer acetate (GA) comprises of 4 amino acids found in myelin basic protein, namely lysine, tyrosine, alanine and glutamic acid. It is not clear on the exact mechanism of action of GA, but there is evidence to suggest that GA shifts the population of lymphocytes from Th1 (pro-inflammatory) to Th2 (regulatory), thereby reducing inflammation. It is also thought that by using amino acids found in myelin basic protein, these will act as a decoy for the immune system, thereby slowing the disease

course. However, studies have demonstrated that while the number of relapses does decrease with the administration of GA, disability progression does not slow in RRMS disease types.

Dimethyl Fumarate (DMF) is the methyl ester form of fumeric acid which has been found to reduce relapse rate and time to progression of full MS. As such it is marketed in the EU under the name Tecfidera and is generally only prescribed to patients who do not have a highly active form of RRMS. Like the interferons, DMF inhibits the production of pro-inflammatory cytokines to aid slowing of disease progression. Teriflunomide is another oral DMT which has been shown to reduce relapse rate by 30% with less severe side effects compared to DMF. While the mechanism of action of Teriflunomide is not completely understood, it is thought that as it inhibits rapidly dividing cells such as activated T-cells thereby reducing the relapse rate in RRMS patients. Finally, Fingolimod is a sphingosine-1-phosphate (S1P) receptor modulator. S1P1 is used in lymph nodes to help with egress of lymphocytes out into the circulation. Fingolimod causes internalisation of the S1P1 receptor and thereby sequestering lymphocytes to the lymph nodes and preventing them from taking part in an ongoing immune reaction.

Humanised monoclonal antibodies have been available for the treatment of MS since 2004, when Natalizumab was first introduced followed by Alemtuzumab. They work with extreme specificity, from reducing immunoreactivity of $CD4^+$ lymphocytes and marking CD52 antigen-carrying lymphocytes for destruction (Natalizumab and Alemtuzumab, respectively)[14,65]. By reducing immunoreactivity of T-cells, Natulizumab helps to prevent activated T-cells from crossing the BBB, further worsening inflammation, while destruction of lymphocytes with Alemtuzumab helps to reduce overall immunoreactivity. From their mechanisms of action, however, use of mAbs tends to be reserved as a treatment option for aggressive forms of MS. The suppression of vital parts of the immune system by mAbs opens patients up to opportunistic infections, notably progressive multifocal leukoencephalopathy.

Chapter 3: Neurovascular Coupling

3-1 Introduction

The structural and functional integrity of the brain relies on the close balance between energy demands and substrate delivery in the form of blood flow. While the energy demands of the brain are extremely high, there is little capacity for energy storage. Therefore increases in neuronal activity must be matched with local increases in cerebral blood flow (CBF), referred to as functional hyperaemia[66]. Breakdown of signalling between neural or glial cells and blood vessels, and the resulting hypoxia have been implicated in several other CNS disorders such as stroke, Alzheimer's and amyotrophic lateral sclerosis (ALS)[67–70]. This effect has been extensively studied in Alzheimer's disease (AD), where hypoxia leads to altered ATP synthesis, Na^+/K^+ ATPase activity, pH alterations and electrolyte imbalances. All these lead to the accumulation of proteinaceous toxins – like hyperphosphorylated tau and amyloid-β - know to be associated with AD, but also white matter lesions and oedema, two classic symptoms of MS[67].

fMRI has provided some insight into brain activity through non-invasive measurement of task-related blood flow changes, however, this still relies on the communication between neurons/glia and arterioles. As functional hyperaemia appears to be involved and altered in the pathophysiology of many disease states, establishing a method of measuring this coupling would be extremely useful to aid diagnosis and treatment. First, the signalling methods underlying this response need to be established and examined more closely.

3-2 Neuronal regulation of local blood flow

Arterial supply to the brain can be considered at several levels (fig. 3-1). Pial arteries branching off large suppling arteries split further into penetrating arteries. These burrow down into brain tissues and eventually split again into capillary beds where oxygen exchange can occur with surrounding parenchyma. The largest increases in vascular resistance is found in the penetrating arteries, where smooth muscles cells surrounding the vessel provide regulation of luminal diameter, and therefore CBF to the underlying regions[71,72]. As these vessels are found in areas of synaptic activity these

arterioles are likely to be targets of local pathways regulating the functional hyperaemic response. The individual network of neurones and supporting glial surrounding a penetrating artery/capillary cells is called a neurovascular unit (fig. 3-2).

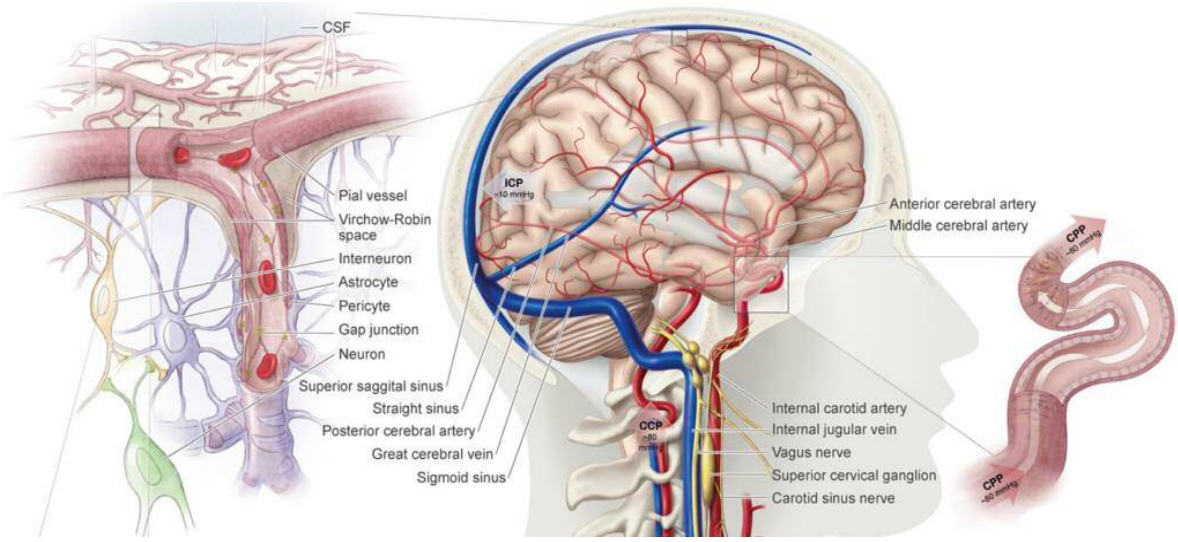

Figure 3-1 Schematic of levels in the brain vasculature. Large arteries splitting off the Circle of Willis pass over the cortical surface, these split into penetrating arteries that burrow into the cortex where they begin to be surrounded by interneurons and astrocytes. As no oxygen exchange takes place at these larger arterioles, vascular smooth muscle surrounds the vessel walls, regulating luminal width and being a key regulator of local CBF. Finally, these split again to form capillary beds where oxygen exchange can take place. As capillaries are too small to be surrounded by vascular smooth muscle, they instead have pericytes which are slightly contractile and provide an extra level of regulation for CBF. Image taken from[227]

Initially it was thought that coupling was mediated by an increase in metabolic demand from neurons, or that neurons could directly signal and control vascular smooth muscle. Increases in haemodynamic activity occur within 1-3 seconds following task onset, far faster than any meaningful increase in the production of oxidative metabolic products[73,74]. Increased arterial CO_2 also causes basal hyperperfusion. Recent studies investigating the effects of inspired CO_2 to induce hypercapnia in healthy volunteers found a reduction in percentage change in CBF during a graded visual task, compared to the responses measured during normocapnia[75]. However, no change in absolute CBF was detected between normo- and hypercapnic challenges at any contrast of the visual task. So, while the metabolic demands of neurons remain the same between normo- and hyper-capnia during the visual task, absolute CBF is maintained depending on the stimulus strength. Hypercapnia also results in a reduction in broadband neuronal rhythmicity (and therefore neuronal metabolism) and blood flow in the resting default mode network and during tasks[76–79]. The increase in arterial CO_2 decreases pH and

causes the release of adenosine – a molecule shown to reduce cortical excitability as well as causes vasodilation[80–82]. This implies that CBF alteration might be occurring through a range of intermediaries (such as calcium and potassium ions, lipid soluble gases like nitric oxide, pH, and purines such as adenosine) rather than being directly affected by metabolic signalling.

Formation of the blood brain barrier (BBB) ensures the isolation of the delicate CNS from circulating substances, including those that could potentially be harmful, such as bacterial or viral infections, or metabolic products that could interfere with normal neuronal signalling. This is done through the use of tight adherens junctions which prevents the transfer of any molecule between cells. Any signalling

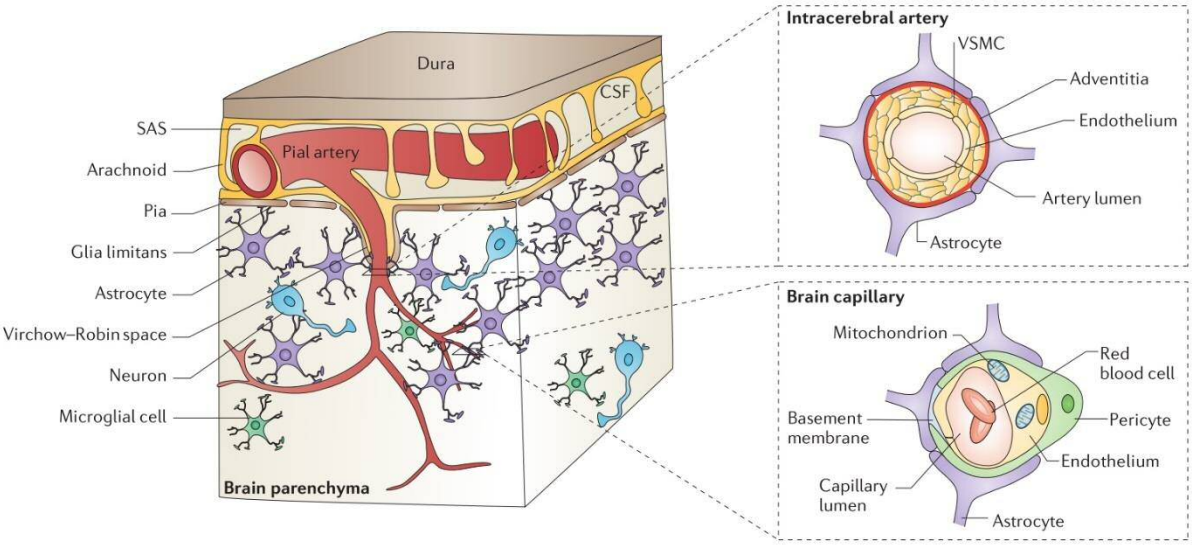

Figure 3-2 A similar schematic to figure 3-1, but with the neurovascular unit shown on the right. Larger arterioles are surrounded by vascular smooth muscle which helps support vessel integrity against intra-luminal pressures from blood flow. These vessels are surround by astrocytic end feet which provide trophic support as well as being key regulators of myogenic tone for VSMCs. Further down at the capillary level, pericytes take over the role of VSMCs and provide some level of contractility and therefore micro control over CBF. Pericytes are similarly surrounded by astrocytic end feet which again provide signals passed through from neurons as to the amount of CBF required. Image taken from[67].

used to elicit NVC must therefore pass via endothelial cells (ECs) forming the BBB before acting on vascular smooth muscle cells (VSMCs). Neurons do not form a direct connection with the ECs making up the BBB[83]. Astrocytes, while lying abluminally to ECs do form numerous connections to the BBB through their end feet, which are known to be able to excrete many substances for altering vascular smooth muscle contractility and BBB permeability[81,84–86].

Several studies have indicated that neurotransmitter release might be crucial to signalling for increases in CBF, particularly the excitatory neurotransmitter glutamate[8,34,81,87,88]. Ionotropic glutamate receptor activation may mediate some CBF increases through the action of calcium-activated synthesis of nitric oxide (notably via the inducible isoform of the nitric oxide synthase enzyme – iNOS but some brain areas use neuronal NOS – nNOS), as well as the release of prostaglandins (PGE_2) and epoxyeicosatrienoic acids (EETs)[81,82,86,89,90]. Presynaptic release of glutamate, while having a main purpose of transmitting action potentials to a neighbouring neuron, would also cause the activation of astrocytes with endfeet lying close to any synapse. Neuronally derived NO is also produced during action potential firing (although which isoform of the synthase responsible appears to differ depending on the brain region[87,91]). Being such a lipid soluble gas, but with a short half-life, it would have direct vasodilatory control over nearby vessels. This method of functional hyperaemia is not the complete story, however[67,90,92,93]

Histological studies have concluded that many processes of vascularly active interneurons, especially those expressing noradrenaline, synapse onto astrocytes rather than directly onto the vascular smooth muscle cells (VSMCs) of blood vessels. Indeed, vascular smooth muscle is rich in inwardly rectifying potassium channels (K_{ir} 2.1 and 2.2) and purinergic receptors, the former of which has been demonstrated to be crucial to the alteration of luminal diameter[94]. The morphological set up of the neurovascular unit examined here suggests that all signalling molecules required for vascular control must first pass through astrocytes before an effect on the vasculature can occur – the most notable exception of course, being gaseous transmitters such as NO.

3-3 Astrocytic responses

Astrocytes unlike neurons are electrically unexcitable, meaning they cannot convey information through the use of action potentials like neurons. Instead astrocytes rely on the release of Ca^{2+} as a means of controlling and communicating information to other cells. Brain slice studies have shown that astrocytes, when excited through either an external influence, or through neuronal firing trigger

the release of calcium from internal stores, resulting in the dilation or constriction of surrounding vessels[85,95].

Whether an astrocyte causes the dilation or constriction of vessels is determined by the secondary messengers released during the brief increase in intracellular calcium ($[Ca^{2+}]_i$). Dilation it seems, is mediated through the actions of metabotropic glutamate receptors (mGluR) resulting in the release of either cyclooxygenase related compounds, or the combined effects of the K_{ir} channels causing local changes to the concentration of extracellular potassium ($[K^+]_o$) mentioned previously. Constriction of vessels appears to be a little more complex, with several other messengers having been found to cause this effect. The conversion of arachidonic acid to 20-hydroexyeicosatetraneoic acid (20-HETE) by the cytochrome P450 enzyme has been found in smooth muscle cells around vessel walls found to cause vasoconstriction. Other studies have suggested the release of NO to be important in determining whether a vessel dilates or constricts (indeed this has been mentioned previously in chapter 2, the tonic actions of endothelial NOS – eNOS – is well known to be crucial to the maintenance of vascular tone, with stimulation of iNOS also having the resultant dilatory effect).

In vivo studies looking at the time course of intracellular calcium concentrations of astrocytes have been able to determine that both sensory stimulation, or direct electrical stimulation of neurones elicited transient increases in astrocytic $[Ca^{2+}]_i$ in cortical layer II. Astrocytic responses also appear to modulate in response to local synaptic input. Stronger neuronal firing (as determined through LFP recordings) resulted in higher astrocytic responses[96]. The timing of these responses appears to differ depending on the study and the region of interest. The changes in $[Ca^{2+}]_i$ vary between 1-6s from stimulus onset, with functional hyperaemia is known to take approximately 2s from stimulus onset. Delays of peak calcium concentration in the visual cortex were found to be on the order of 3-4s, a higher latency than that of functional hyperaemia. It is known that quantitative dyes used to measure changes $[Ca^{2+}]$ have trouble detecting modest changes in $[Ca^{2+}]$ due to the dual-wavelength nature of these dyes[97,98]. Dyes loaded within neurons are also known to accumulate in the cell bodies, or

sometimes larger processes meaning the area where Ca^{2+} would be taking effect; i.e. astrocytic endfeet are likely to have a lower concentration of dye and be unable to detect subtle shift in $[Ca^{2+}]$[99]. Finally, as calcium is such an important signalling molecule, its concentration is kept under strict control. Therefore, all cells have a significant buffering capacity for free calcium which would reduce a dye's ability to accurately report changes in $[Ca^{2+}]_i$. This means that early, modest rises in $[Ca^{2+}]_i$ could go undetected for some time, but may be of a significant level to cause the functional hyperaemic response[98].

Another scenario is possible, however, astrocytic $[Ca^{2+}]_i$ rises might indeed be slower than the functional hyperaemic response. The presence of extra-astrocytic vasoactive substances such as NO, released from interneurons which are known to occupy a similar space to astrocytic endfeet, but not to the same concentration, could be responsible for an initial rise in CBF. This initial rise would present itself as the functional hyperaemic response seen within 1-2s of stimulus onset, astrocytes however are required to maintain the response and their effects come into play 3-6s after stimulus onset, releasing less potentially toxic and damaging substances such as NO[84].

3-4 Astrocytic activation

The excitatory neurotransmitter glutamate has been shown to be the only relevant neuron-derived substance that can elicit both an increase in astrocytic $[Ca^{2+}]_i$ and is released following sensory stimulation in vivo. Glutamate released by neurons acts on metabotropic glutamate receptors found on astrocytes (namely mGluR1 and mGluR5) to mediate the functional hyperaemic response. The blockade of these receptors leads to attenuation of calcium rises in astrocytes as well as local increases in CBF without affecting either pre- or post-synaptic activity. These instead rely on the ionotropic NMDA and AMPA receptors.

The contribution of synaptic glutamate to astrocyte activation is still under discussion. Recent results looking into the role that ionotropic glutamate receptor activation plays in astrocyte activation showed blockade of NMDA and AMPA receptors (NMDAr and AMPAr respectively) to have no effect

on astrocytic calcium levels, contradicting early results showing postsynaptic glutamate to have a large contribution to astrocytic signalling[100,101]. Further work has led to the possibility that two mechanisms exist to mediate functional hyperaemia depending on stimulus strength. Studies using rodent olfactory bulbs revealed a predominate role of presynaptic glutamate release to be mediating local CBF changes when low concentration odorants were used. A following study noted that stronger and more widespread activation relied heavily on postsynaptic glutamate release as global – but not local – blockade of postsynaptic responses ameliorated CBF responses[84,101].

This differing method of activation could be in response to altering metabolic trends. Postsynaptic receptor responses account for just 0.3% of the brain energy budget when activation is low, but increases to 33% when under heavy utilisation[100].

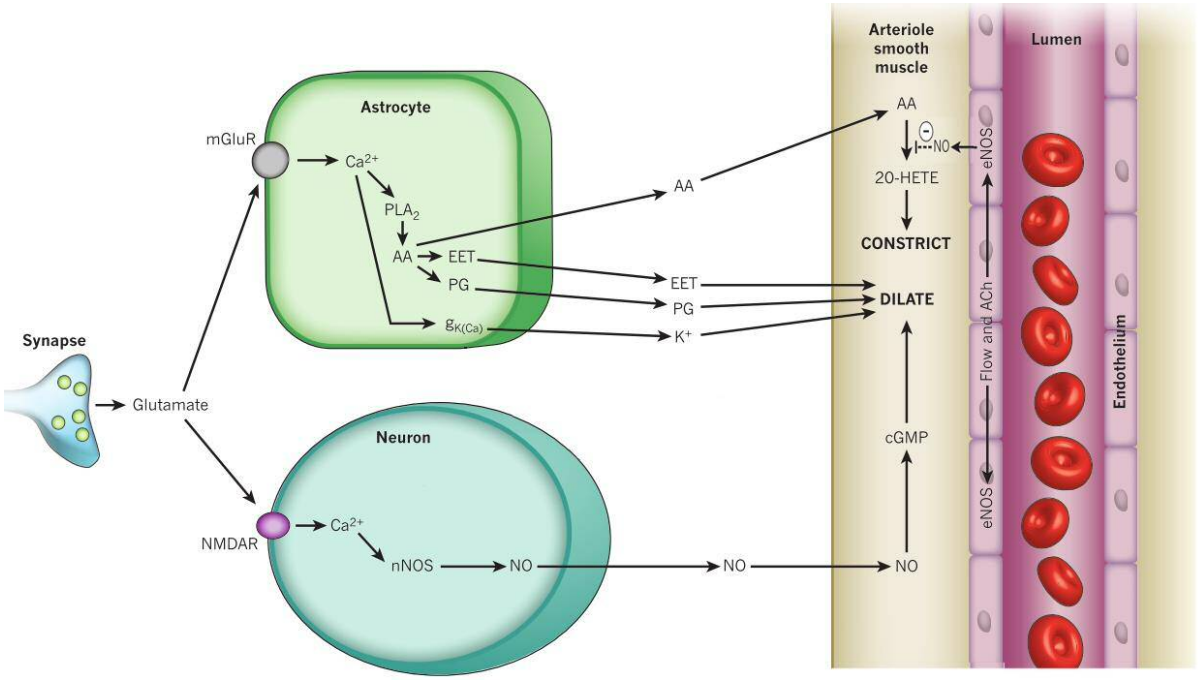

Figure 3-3 Summary of the role astrocytes and neurons play in NVC. Activation of astrocytic mGluRs cause a rise in intracellular calcium. This results in the generation of AAs by phospholipase A (PLA) and the activation of membrane B_k channels. AAs quickly converted to EET and PGE_2 where, along with rises in extracellular K^+ they cause relaxation of vascular smooth muscle and vasodilation. Activation of post synaptic neurons through AMPArs and NMDArs causes the activation of either iNOS or nNOS depending on the brain region in question. This highly diffusible gas has a direct effect on local vascular smooth muscle and pericytes, causing relaxation and vasodilation. Shear stress generated by the flow of red blood cells (RBCs) through the vessel leads to the release of acetylcholine (ACh) and the activation of endothelial NOS (eNOS). This tonic action of eNOS constantly generates low levels of NO and provides very low levels of vascular homeostasis, independent of neuronal or astrocytic control. When constriction is required, such as during high O_2 episodes, AA is transported to VSMCs where it gets converted to 20-HETE. This is a vasoconstrictor and is the main method of astrocytes to induce this response. NO inhibits the production of 20-HETE, as does the production of lactate, meaning that levels of 20-HETE are always kept to a minimum unless more than enough oxygen and glucose is being supplied. Image adapted from[86].

3-5 Signalling for a higher blood flow

It has been established that neuronal activation leads to $[Ca^{2+}]_i$ rises in astrocytes. I have not yet discussed how these calcium rises result in a change in smooth muscle contraction. Using brain slice preparations, it was determined that during low $[O_2]_o$ Ca^{2+} rises, triggered via an mGluR agonist, lead to vasodilation. During high $[O_2]_o$ the same stimulus lead to constriction of local blood vessels (fig.3-3 and 3-4).

Rises in astrocytic $[Ca^{2+}]_i$ through mGluR activation causes production of arachidonic acid (AA) in a phospholipase A (PLA)-mediated manner. Arachidonic acid then converts to prostaglandin-2 (PGE2)

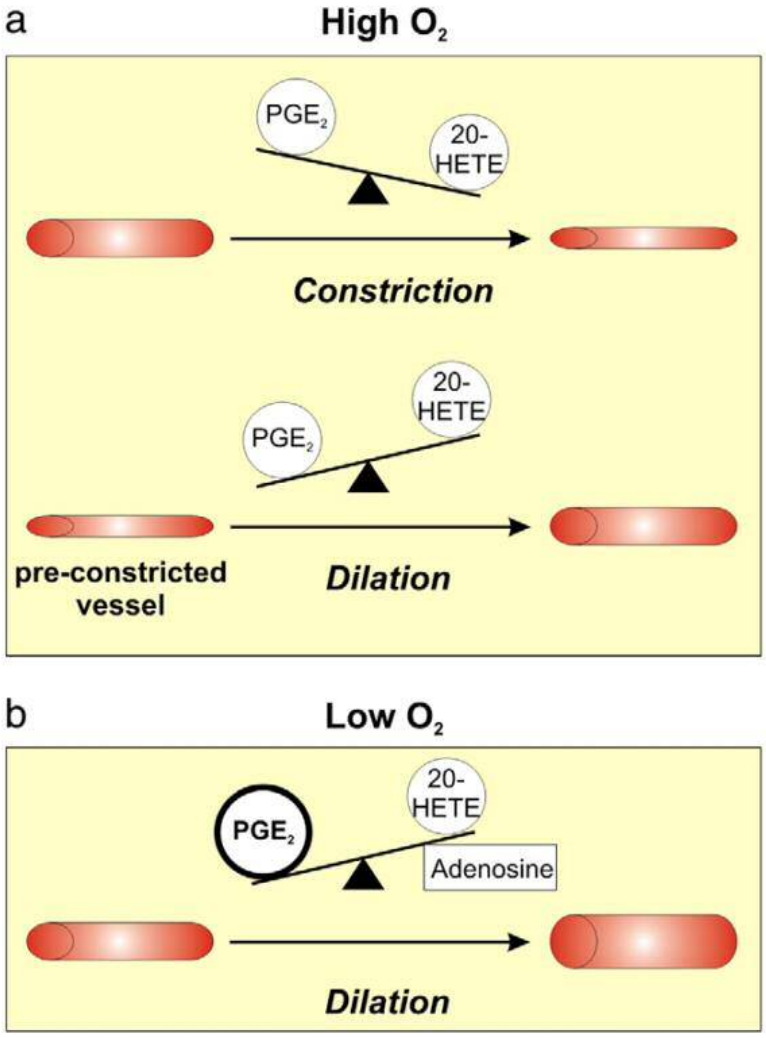

Figure 3-4 During high O_2 periods, 20-HETE is produced leading to constriction of dilated vessels. In vitro studies using pharmacological pre-constriction of vessels noted that astrocytic activation lead to the production of PGE_2 instead, resulting in vasodilation. A feedback mechanism is in place the prevents vessels from over dilating, even when O_2 is in high supply. During periods of hypoxia however, the production of lactate also causes adenosine production. This inhibits the conversion of AA to 20-HETE, instead favouring the PGE_2 route. This then leads to maximal dilation. Image taken from[89].

and epoyeicosatrienoic acids (EETs) through cyclooxygenase-1 and cytochrome P450 enzymes respectively. Both of these vasoactive compounds, when released from astrocytes they exert their effects on VSMCs to cause vasodilation[67,81,86,102]. Oxygen levels themselves are not sufficient to switch between dilatory or constrictive effects of astrocytes. During hypoxia, the production and accumulation of extracellular lactate and adenosine helps tip the balance of PGE_2 to exert a larger vasodilatory effect on vessels by blocking prostaglandin transporters in astrocytes. Finally, rises in intra-astrocytic Ca^{2+} levels cause the activation of calcium-activated potassium (BK) channels located in astrocytic endfeet wrapped around vessel walls[81,94]. Potassium ions released here are allowed to enter through K_{ir} channels mentioned previously, located in vascular smooth muscle, influx of K^+ leads to relaxation of muscle cells[89].

In high O_2 environments lactate and adenosine are not produced in significant quantities, making inhibition of prostaglandin transporters negligible. Therefore, when activated, the increases in astrocytic [Ca^{2+}] result in the production of 20-HETE via the same PLA-dependent mechanism by which AA is produced. As PGE2 and EETs are not able to enter the perivascular space in large quantities as they would during hypoxia, the vasoconstrictive effects of 20-HETE are able to proceed[103].

In vitro studies into the regulation of vessel tone have limitations however. Many are performed on brain slice preparations, which have the notable lack of any blood flowing through the vessels in question. It is well known that vessels used in these kinds of preparations are maximally dilated as any myogenic tone that would be present due to intraluminal pressure is missing[104]. To counter this, studies tend to use a pharmacological method for pre-constricting vessels, but this comes with the caveat that substances used to artificially constrict vessels could interfere with the timing or strength of any vessel response. Finally, the length of time taken for vessels and astrocytes to respond to a stimulus comes with another major confound; *in vitro* studies of brain slices rely heavily on assuming that the time taken for changes in vascular tone to been seen is equal to what would occur *in vivo.* They are unable to take into account any effects the lack of perfusion, temperature changes or the

possibility of interference from pharmacological pre-constriction/maximally dilated vessels might have on the experiment. It should be noted that the arguments and conclusions presented in this chapter on the role of astrocytes or the method for NVC relying on evidence gathered from brain slice preparations be subject to these confounds.

This differential selection of vascular responses being dependent on the concentration of O_2, or more specifically oxyhaemoglobin (oxyHb) lacks much *in vivo* support by the studies mentioned so far. Fortunately, the advent of functional neuroimaging techniques has allowed the qualitative (and more lately quantitative) measurement of CBF. Several studies have made mention to the initial alterations of [oxyHb] and [deoxyHb] around 300-500ms following stimulus onset, due to the activation of neurons and astrocytes[105–108]. The decrease in [oxyHb] following stimulus onset was first seen using blood oxygenation level dependent contrast (BOLD) fMRI, a technique still used to measure the relative changes in blood flow[105,108]. BOLD contrast will be discussed further in chapter 4, but it relies on the ratio between oxyHb and deoxyHb and the differing magnetic properties between the two. Thereby allowing a non-quantitative way of measuring blood flow and relative oxygen changes. BOLD fMRI studies revealed a bi-phasic response of blood flow to prolonged neuronal activation. Following on from the 'initial dip' in oxyHb, BOLD signal then increases sharply, representing an increase in [oxyHb] to the local area which could only be coming from an increase in CBF and presumed vasodilation.

So far this chapter has covered a brief overview of the current trends in neurovascular coupling along with evidence to support how the mechanisms could work in biological systems. There is growing evidence for the neurovascular unit, and therefore neurovascular coupling to be affected by loss of BBB integrity and permeability in other degenerative diseases such as AD and ALS[67,69,70]. In chapter 2 I proposed a hypothesis for how multiple sclerosis progresses along with some of the molecular and morphological changes occurring throughout the disease. It should be without question that there is disruption of normal vascular function in MS, as well as an alteration in normal neuronal function. A

direct link between the two however, has not been discussed or proposed. Being able to provide a marker that can measure neuronal activity, and couple this to a quantitative measure of CBF would be extremely useful for gaining further insight into NVC, and how this is affected in a neurodegenerative disease state such as MS.

Chapter 4: Imaging Methods

4-1 MRI

4-1-1 Principles of MRI

The main component of the MRI scanner is a large superconducting electromagnet. By cooling large loops of wire down to 4K, all electrical resistance is lost. Passing a current through the wire generates a perpetual, and large, magnetic field called B_0. Additional, smaller radiofrequency (RF) coils are situated throughout the bore of the scanner, allowing transmission and detection of RF pulses. These can temporarily induce a magnetic field at perpendicular to the main B_0 field, called B_1.

Magnetic resonance imaging (MRI) relies on the properties of atomic nuclei to create maps and images of organisms and objects. As the human body is composed of around 80% water, a molecule that contains two hydrogen and an oxygen atom, hydrogen is therefore the most abundant element in the body. 99.99% of all hydrogen in the human body is hydrogen-1 (^{1}H); and is composed of a single proton and electron, but more importantly exhibits a net 'spin'.

Under normal conditions spins are randomly orientated and therefore the magnetic components of these spins cancel each other out. When placed in the strong B_0 field, spins align either parallel, or anti-parallel to the B_0 direction. A greater proportion of spins (around 0.00001% more) align parallel, rather than anti-parallel to the magnetic field. Once aligned in a parallel fashion, atoms are in a lower energy state (as opposed to a 'high' energy state for those aligned anti-parallel), and gives the object (or tissue) a net longitudinal magnetisation (figure 4-1). When aligned in the B_0 field, ^{1}H atoms precess at the Larmor frequency. This is calculated through the multiplication of the gyromagnetic ratio of the atom (the ratio of the nuclear dipole moment to the angular momentum), with the strength of the B_0 field in tesla, hydrogen has a gyromagnetic ratio of 42.6MHz/Tesla, so the Larmor frequency in a 3 Tesla environment would be 127.5MHz.

Using transmitter coils RF pulses are rapidly switched on and off to create fields perpendicular to B_0. When emitted at an atom's resonant or Larmor frequency, spins align with the new magnetic field (B_1). The angle of the B_1 pulse (e.g. 90°) 'flips' the protons and changes the net magnetisation from longitudinal, to transverse. When B_1 is stopped, spins re-align back along the B_0 releasing RF energy as they do so. This process is known as relaxation and is quantified from the changes in voltage detected in receiver coils tuned to the Larmor frequency.

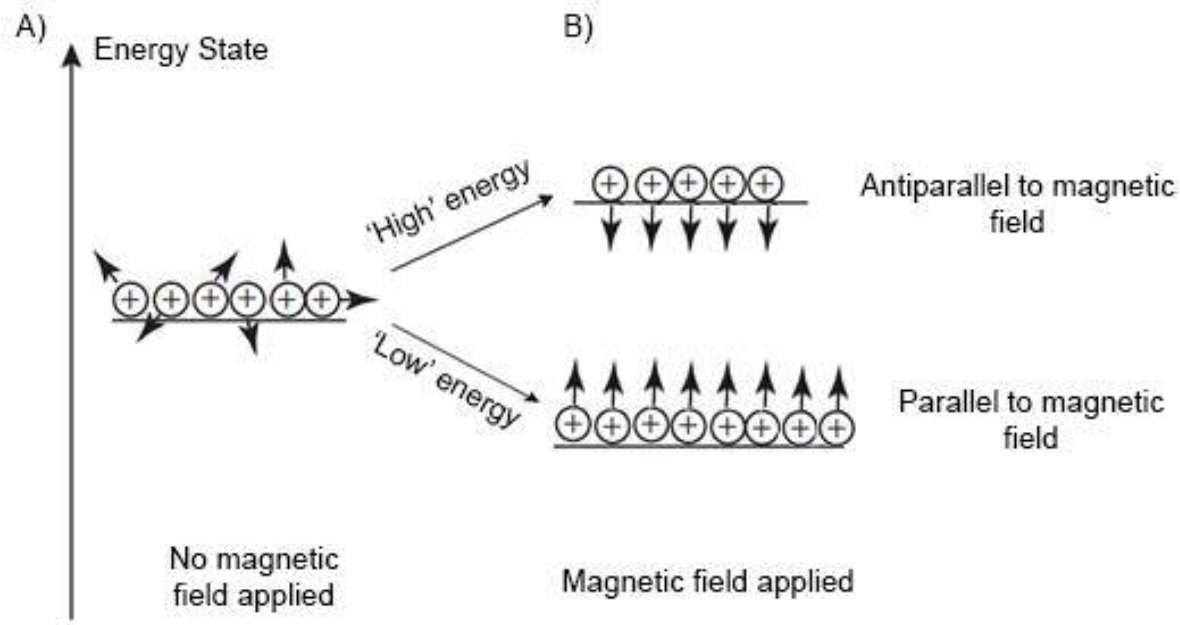

Figure 4-1 Schematic of hydrogen atoms and spin directions following application of a main B0 field. When spins are aligned parallel to the B_0 field they are said to be in a 'lower' energy state than those aligned anti-parallel. For this reason slightly more hydrogen atoms align parallel to the main magnetic field. Image adapted from: http://www.expertsmind.com/topic/proton-nuclear-magnetic-resonance-spectroscopy/external-magnetic-field-913940.aspx

4-1-2 Relaxation

After removing the B_1 field, net magnetisation returns along the longitudinal axis- following B_0 and therefore a lower energy state compared to being aligned transversely.

There are two relaxation process occurring here: the recovery of longitudinal magnetisation along B_0 (T_1); and the decay of transverse magnetisation provided by B_1 (T_2). Both have two very different times to relaxation. T_1 has a relaxation time on the order of seconds, whereas T_2 is generally orders of magnitude smaller (milliseconds). The rate of relaxation is also dependent on the type of tissue (due

to differing molecular compartments) and the B_0 field strength, but refers to the time taken for magnetisation to return to 63% of its original value.

In addition to creating transverse magnetisation, application of a radio frequency (RF) pulse along B_1 forces spins into phase. Loss of B_1 causes magnetisation to be lost quickly though dephasing of these spins (spin-spin relaxation) this is caused by interaction of protons with each other causing phase angles to alter leading to the loss of spin coherence or phase, and therefore transverse magnetisation. In spin echo readouts (SE), the initial 90° pulse is followed by a 180° refocussing pulse. This reverses the decay of transverse magnetisation causing spins to come back into phase at the same time delay as the interval between pulses. The refocussing of the net magnetisation is referred to as the echo. The time between the initial 90° pulse and the maximum echo amplitude is referred to as the echo time (TE). Spin-spin relaxation mentioned previously is not rephased following this refocussing pulse, so any transverse magnetisation will be affected by T_2 relaxation.

The interactions of protons with each other means dephasing is also reliant on thermal motions of the molecules within the tissue as well as imperfections in the B_0 field. By accounting for these, T_2* creates an additional form of contrast, however, T_2* dephasing occurs faster than normal T_2. For T_2* sensitive images to be acquired, a gradient echo (GRE) sequence is used. This differs from spin echo in that, rather than using a 180° refocussing pulse following the initial excitation, a bipolar gradient is applied instead. The initial gradient accelerates dephasing, the polarity of the gradient is quickly reversed thereby refocussing only those spins affected by the first gradient. The ability of GRE to detect changes in T_2* is used later in this thesis, as it forms the basis of functional MRI (fMRI), and the ability to detect changes in Blood Oxygenation Level Dependent (BOLD) signal.

4-1-3 Functional MRI (FMRI)

4-1-3-1 Blood oxygenation dependent (BOLD) signal

An endogenous contrast can be obtained using the differing magnetic properties of haemoglobin according to levels of oxygenation. When deoxygenated (deoxy-Hb), haemoglobin is paramagnetic;

meaning it interferes with magnetic fields. However, when oxygenated (oxy-Hb) haemoglobin is diamagnetic therefore does not cause field inhomogeneities. Using these properties; it is possible to measure the relative changes in oxy-Hb levels in the tissue, increases in local deoxy-Hb concentration creates a less homogenous magnetic field, thereby decreasing T_2*.

BOLD fMRI can be used to indirectly identify regions of enhanced neural activity. As previously mentioned in chapter 3, activation of neurons results in a rise in metabolic demand for substrates such as glucose and oxygen. It would be assumed that this would lead to an increase in deoxy-Hb and a decrease in T_2* signal. However, regions of activation show an increase in T_2*- weighted signal[109,110]. This is due to the previously mentioned haemodynamic response. Regions of activation have a large increase in cerebral blood flow (CBF), far above the rise in oxygen extraction of surrounding local tissue, because of this the ratio of oxy-Hb outweighs that of deoxy-Hb, reducing magnetic field inhomogeneity and increasing T_2*-weighted signal. As BOLD signal relies on the total amount of deoxy-Hb in an imaging voxel, anything that alters this can affect BOLD signal, including changes in cerebral blood volume (CBV), CBF and cerebral metabolic rate of oxygen consumption (CMRO2). BOLD is therefore an indirect, non-quantitative measure of neural activity. While a quantitative measure of CBF would be far more useful clinically, BOLD represents the combination of CBF, CBV and CMRO2 and can therefore be argued to represent a more complete but complex picture of the vascular and metabolic changes occurring in a region rather than focussing solely on CBF. The BOLD response has been shown to have correlations with changes in certain neural oscillatory bands, and local field potential recordings (described further in section 4-1-2) and appears to be primarily affected by changes in the excitation-inhibition balance of different neuronal populations[106].

4-1-3-2 Arterial spin labelling (ASL)

Instead of using the innate contrast afforded by haemoglobin, exogenous contrast can also be applied. By selectively sensitising or labelling blood coming into the tissue within a region of interest maps of perfusion-weighted signal can be obtained. When blood is labelled magnetically this is a technique

called arterial spin labelling (ASL). Here ^{1}H of blood is labelled at a lower point away from the imaging plane, usually in the neck. Labelling is done through either inverting, or saturating the longitudinal magnetisation of ^{1}H in blood water before it flows into an imaging plane. After a period of time (transit time) has passed to allow the magnetically labelled blood to perfuse the region of interest, labelled blood water exchanges with water already present in the tissues. This alters the tissue magnetisation, reducing it and thereby altering MR signal in a perfusion-dependent manner[111,112].

A minimum of three images must be taken to achieve a quantitative measure of CBF; a tag and a control image as well as a calibration (M_0) image containing a map of longitudinal tissue magnetisation (fig. 4-2). The tag image is taken in the presence of labelled blood; the control image is taken when no labelling is performed. The M_0 image is required to calibrate both images to a normalised, standard scale and therefore is essential for perfusion quantification and inter-subject comparisons. The difference between these two images is proportional to tissue perfusion, and therefore CBF. Additional calculations need to be performed to get a measure of cerebral blood flow (CBF) as ml/100g of tissue/minute. Figure 4-3 shows the change in signal in an ASL-acquired image over time also known as the kinetic curve. It is important to note that there are 3 stages to this figure:

1. No signal change is present before the arrival of labelled blood.
2. After a transit time of δt labelled blood water starts to arrive and reaches a peak at τ tag width.
3. Signal starts to dissipate as blood is cleared through venous drainage, and longitudinal relaxation.

This has a mathematical representation and has been described in[113]. Throughout these calculations there is the assumption that each voxel only contains tissue and that exchange of labelled hydrogen occurs immediately with the arrival of labelled blood water. In conventional spin-echo sequences the first 90° flip is followed by a 180° refocussing pulse which leads to the formation of the echo at time TE. Inversion recovery sequences contain an initial 180° inversion pulse before that first 90° flip. This

initial 180° pulse inverts the longitudinal magnetisation of all tissues to the opposite direction of B_0, following which the affected tissues begin to undergo T_1 relaxation. The time between the first 180° pulse and the 90° flip is called the inversion time (TI). Throughout this thesis when CBF is quantified, a multiple inversion time (MTI) sequence is used to calculate resting CBF. This is done because there are four unknown parameters when fitting the equation stated in[113,114] – arterial blood volume, transit time (the time taken for labelled blood to reach the imaging plane), arterial input and CBF. Therefore, to fit the kinetic curve correctly, sampling must be performed in at least 4 points. To do this multiple inversion times are used which allows sampling at different points along the kinetic curve (fig. 4-3).

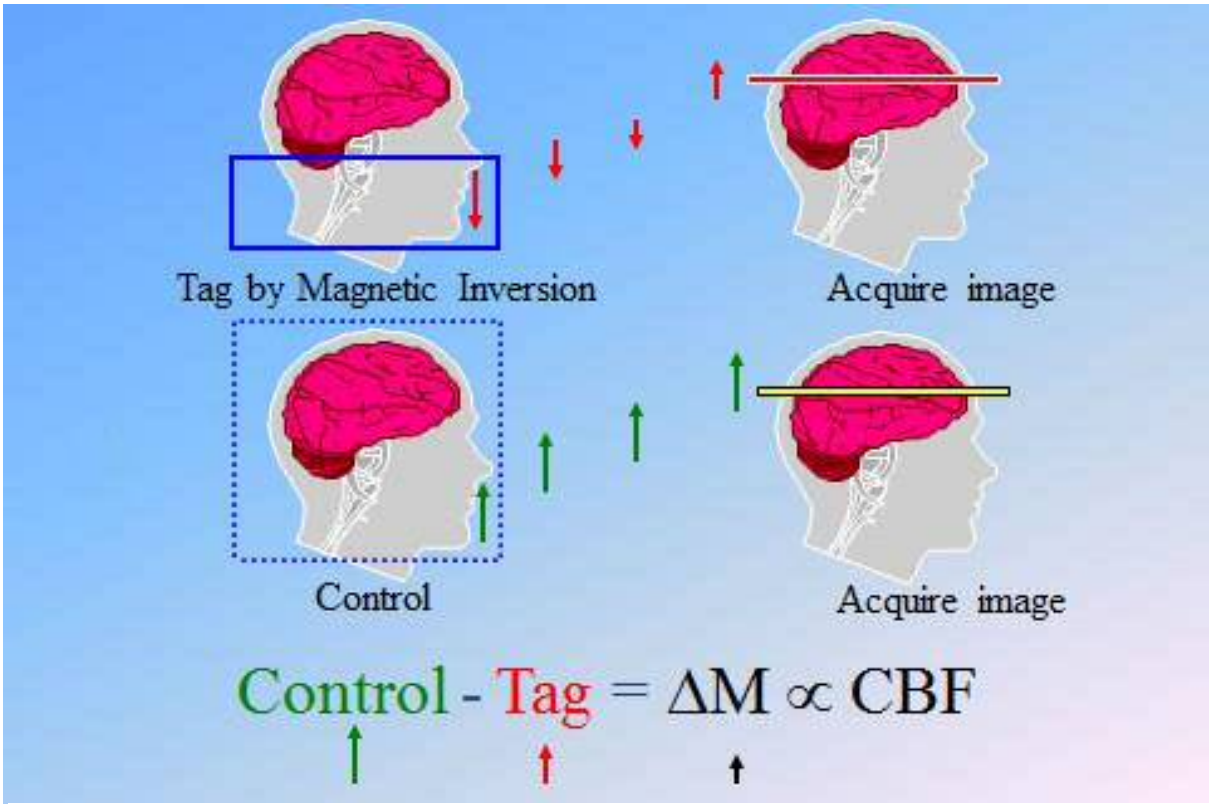

Figure 4-2 Example schematic of the principles of ASL. First by tagging blood entering through the neck either saturating or inverting the magnetisation of blood water reduces the net magnetisation in the imaging plane. After a time delay allowing blood to flow into the region of interest, and blood water to mix with tissue water, imaging of that slice is performed. For results to be meaningful a control image must be taken to get a baseline magnetisation of the tissue. Subtracting the two tag/control images results in a perfusion-weighted map of tissue magnetisation. Image taken from http://fmri.ucsd.edu/Research/whatisfmri.html

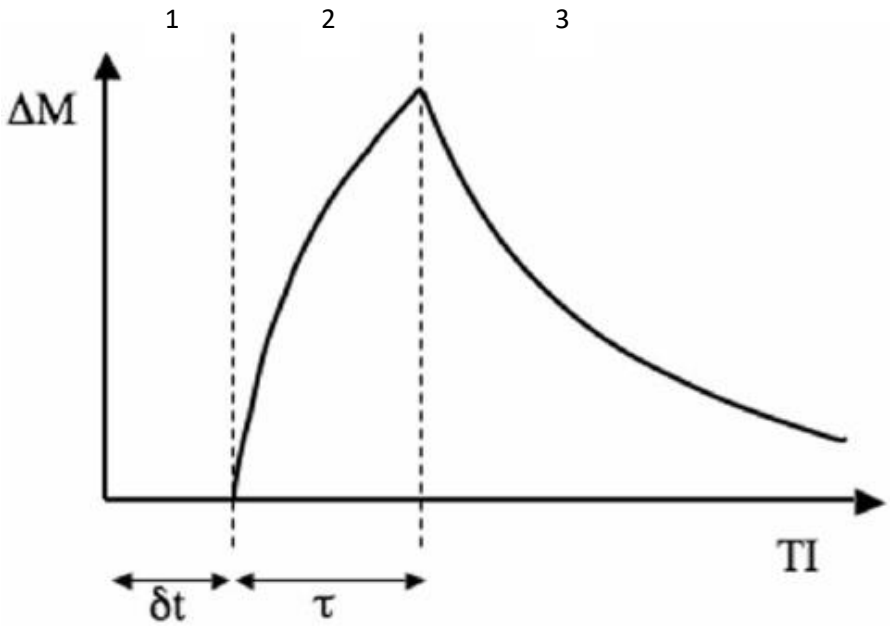

Figure 4-3 Kinetic curve for a pulsed arterial spin labelling dataset. 1) No signal change is detected during arterial transit time. 2) After transit time (δt) labelled blood arrives in the imaging plane where signal increases as labelled hydrogen atoms are exchanged with the tissue. 3) As blood clears through venous drainage and through longitudinal relaxation, the signal tapers off again. Image taken from https://www.researchgate.net/profile/Patricia_Figueiredo11/publication/7835906/figure/fig1/AS:277673537490972@1443213938526/Figure-1-Definition-of-the-arterial-transit-delay-t-and-the-tag-width-in-a.png

4-2 MEG

MRI is useful for detecting changes in cerebral blood flow, but whether using BOLD or ASL imaging techniques MRI can only be used for indirect inferences of neuronal activity. Changes in blood flow co-localise with areas of neuronal activation, but cannot be used by itself to directly measure the level of local neuronal activity. If decoupling exists between neuronal activation and the haemodynamic response, either through an altered stimulus parameter or in disease states, this will not be evident from MRI alone.

All forms of electrical current generate magnetic fields. Post synaptic currents generated by apical pyramidal cell dendrites have been proposed to be the principle source of measurable magnetic fields outside the scalp. Recording magnetic fields generated from neuronal populations has the advantage over measuring electrical activity directly through electroencephalography, as magnetic fields are not blurred during transmission through the scalp. This allows for a potentially better source localisation

solution due to the larger number of detectors available, along with added sensitivity to subtle changes in event-related potentials/fields (ERP/ERFs).

Under resting conditions neurons can fire spontaneously and without any synchronicity. Asynchronous firing means local magnetic fields are either far too small to detect, or easily cancel out one another and no net magnetic field can be detected. When a stimulus is applied, large volumes of

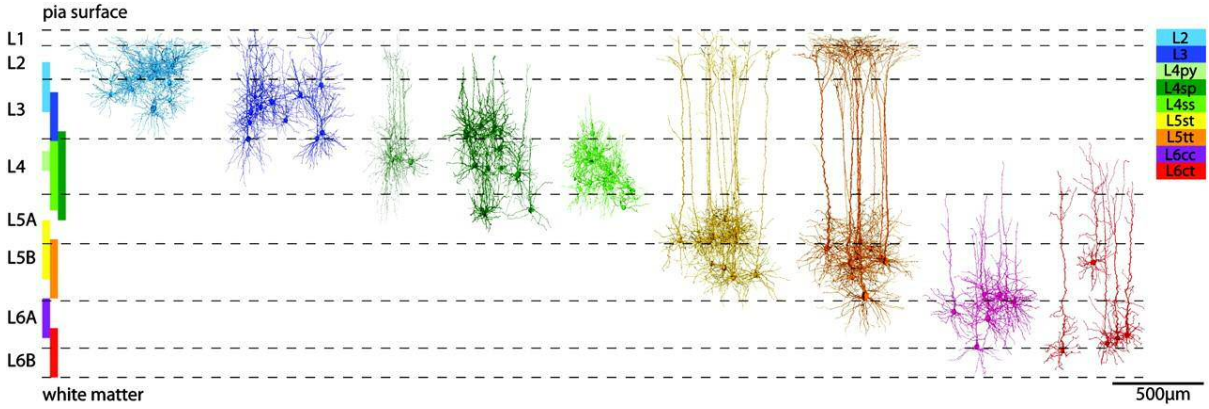

Figure 4-4 Examples of the changes in morphology of neurons at different layers. Layer I and IV contain irregular stellate cells, meaning no net magnetisation is detected on the scalp. Pyramidal cells in layers II, III, V and VI show a regular shape with long axons projecting to more superficial layers. Image taken from http://changelog.ca/quote/2013/09/02/many_types_of_neurons

neurons start firing together. Propagation of local spiking activity is achieved through neurotransmitter release – in the case of visual stimulation from superficial layers of the cortex, to deeper layers – to pyramidal cells where local inhibition (provided by inhibitory interneurons) is overcome to allow propagation of excitatory post synaptic potentials (EPSPs). Due to the regular morphology of pyramidal cells, EPSP firing creates dipole, rather like a bar magnet. Stellate cells and other interneurons with no regular morphology have no net magnetisation during firing due to the random orientation of electrical activity (figure 4-4). Pyramidal cells lying parallel with each other, and in close proximity cause summation of individual dendritic magnetic fields, magnifying the effect of the synchronous firing and appear as a single dipole on the scalp. Indeed, it has been estimated that between 10,000-50,000 synchronous synaptic currents from individual dendrites are required to generate a sufficient magnetic field to be detectable.

These magnetic fields can be detected using superconducting quantum interferences devices (SQUIDs). These are loops of wire with a small gap or junction, which when cooled sufficiently to allow

superconduction to take place the passing of an external magnetic field (perpendicular to the SQUID) generates a detectable current. Modern magnetoencephalographs have between 100-300 SQUIDs; this helps produce a better estimate the magnetic field's source compared to EEG as these tend to be limited to the number of electrodes that can be reliably placed. MEG signals are on the order of <100 fT, to make sure the signals detected are not due to environmental noise MEG systems are housed in magnetically shielded room (MSR). This in addition to loops of wire larger than the SQUIDs suppresses high, and low frequency noise respectively. Pickup coils tend to be either magnetometer, or gradiometers. The latter is used in modern MEG systems, which itself is split into two varieties; axial and planar. Magnetometers and gradiometers differ in that whilst magnetometers have a single loop of wire in their detectors, gradiometers have an additional loop wound in the opposite direction. The additional loop confers a higher sensitivity, along with superior noise rejection, compared to magnetometers.

4-1-1 Event related potentials/fields

With the advent of MEG, resulting data has often been compared to EEG literature. In this respect, there is a slight difference in the nomenclature, when referring to electrical activity measured using EEG we tend to refer to the potentials generated in these recordings (i.e. event related potentials – ERPs). However, in MEG these potentials are not measured; instead the magnetic field activity is detected and therefore the presence/strength of the field is referred to (i.e. event related field – ERF).

The visual system has been thoroughly studied in both EEG and MEG. This is mostly due to the ease with which non-invasive but simple stimuli can be applied to generate a reliable, graded response. The primary visual cortex (V1) is separated into 6 layers by the types of cells it contains (represented by the roman numerals I-VI). Input from the lateral geniculate nucleus arrive into layer IV, containing stellate cells, which have connections to pyramidal cells in layers II, III and V. Pyramidal cells tend to have two sets of dendrites: one large apical dendrite, branching up into higher levels in the cortex; as

well as a large number of basal dendrites, originating below the cell body. As these types of cell only have one axon, which can be very long, they are outputs to other parts of the cortex.

Much of the MEG/EEG signal is composed of apical dendrite activity in layers II, III, V and VI. It is these connections and dendritic currents that sum and magnify the magnetic field to appear as a single dipole. Evoked fields have several components, denoted as either being positive (P) or negative (N), followed by the average latency in milliseconds. In the case of visual evoked fields (VEFs) there are 3 main components: the first, N70, is a negative deflection at 70ms- a positive peak around 100ms; P100; and finally another negative peak at 140ms, N140[115]. Event related potentials/fields are generated following the onset of a brief, sharp stimulus, or stimulus change. For example, an audible tone, or the presentation/reversal of a visual checkerboard. There is a general separation of ERFs into those occurring <100ms from stimulus onset and those after 300ms. Early ERFs are thought to represent only sensory processing, whereas those after 300ms instead represent cognitive processing. The nature of ERFs mean they are highly transient[116–118]. However, they are also phase- and time-locked to the onset of a stimulus, because of this trials can be merged and averaged over time. This is particularly useful for establishing magnitude and latency values attached to ERFs.

4-1-2 Neuronal oscillations

Two types of neuronal oscillations have been noted; evoked and induced oscillatory activity. Evoked oscillations are time-locked to the onset of a given stimulus. Induced (or sustained) oscillations continue after the onset of the stimulus, and remain for as long as the stimulus is present. These differ because the initial spike in evoked activity is thought to represent overcoming the initial inhibition of neuronal firing. Induced oscillatory activity has been thought to participate in the modulation of attention, memory and multisensory integration.

Oscillations are referred to as either showing synchronised or desynchronised behaviour with respect to stimulus presentation. This is because some responses are not phase locked to the stimulus onset, meaning that averaging trials can result in a ‘flattening out’ of the peaks and troughs making averaged

responses appear reduced compared to averaging of a time- and phase-locked stimulus. Therefore, for these types of responses time-frequency estimation within a certain bandwidth is required to determine the power of each bandwidth prior to averaging. Increases in power are referred to as event-related synchronisation (ERS), with reductions in power called event-related desynchronization (ERD).

Neural oscillations occur at a wide range of frequencies, from 1-200Hz, split into several bands; θ (4–8Hz), α (8–13 Hz), β (13– 30 Hz), γ (>30 Hz)[119]. Several groups have demonstrated that a positive BOLD response is correlated to an increase in event-related gamma synchronisation, as well as desynchronisation in the alpha and beta bands[105,120–123]. Gamma power has an interesting property that the others do not appear to share; the level of synchronisation (power) recorded in the gamma band correlates to the strength of the stimulus i.e. in a visual task, the amount gamma power increases by is dependent on the contrast of the visual task[124–127]. Indeed, Stevenson et al (2011) found no correlations with the level of β-band desynchronization and contrast of a visual checkerboard, nor were any correlations found to the strength of the post stimulus β-rebound observed after the cessation of the stimulus. During tasks, there also appears to be increased synchronisation recorded in the theta band along with the increases in gamma power. But while alpha, beta and gamma bands have been shown to be somehow related to the BOLD signal (whether positively or negatively), theta band activity does not appear show any correlation[124].

BOLD has been thought of as representing an indirect measure of enhanced neuronal activity due to previous studies performed by Logothetis et. al (2001), among others, where local field potential (LFP) recordings were found to be a more reliable predictor of the BOLD response than single or multi-unit activity (MUA)[105,124,128,129]. Cortical LFPs have been thought to reflect the average of synchronised pyramidal synaptic signals which are also the basis of the oscillatory recordings in MEG/EEG[124]. Other groups have built on the work done by Logothetis using simultaneous EEG/fMRI as well as offline correlations of neuronal oscillatory activity to explore the neural basis of the BOLD signal. As I

mentioned in the previous paragraph some MEG studies have suggested that event related desynchronisations (ERDs) in the α and β are closely associated with increases in BOLD signal[123,130,131]. This gives rise to the idea that the idling β-band activity seen during rest represents cortical inhibition which needs to be released, stimulation to cortical inputs therefore need to be strong enough to overcome this inhibition and lead to increases in output in the γ band and therefore exhibits a strong on/off property not exhibited by γ band synchronisations[131–133]. Gamma band event related synchronisations (ERS) have been found to be highly spatially correlated with the BOLD response giving further support to the evidence that γ oscillatory activity is at least partially responsible for the BOLD response[124,131,134,135].

For this thesis, I will be focussing on γ band oscillatory activity for one of my neuronal measures to define NVC. Unlike the other bands, it has shown to be robust in its presentation, the level of synchronisation can be manipulated by stimulus strength, and finally, increases in γ synchronisation are known to be positively correlated with the BOLD response. Gamma oscillations are thought to play a crucial role in sensory processing, and are elicited in several sensory paradigms including visual stimulation, but also modulated by attention[136,137]

Gamma oscillations are thought to arise from fast firing interactions between pyramidal cells and inhibitory interneurons, known as the pyramidal interneuron gamma (PING) network[128,138]. These neurons both utilise AMPA and $GABA_A$ receptors as these are fast acting ionotropic channels capable of supporting high frequency spiking activity. Gamma frequency and power of this network is thought to be reliant on the excitatory/inhibitory balance between pyramidal cells and interneurons. Initially an external excitatory drive (from a stimulus for example) overcomes the inhibition imposed by interneurons to allow the propagation of EPSPs, but these are quickly shut off again by the inhibitory activity of interneurons. As stimulus intensity increases, so does the excitatory drive, meaning the time between EPSP firing, inhibition and firing again is reduced. This cycling of events creates the γ band oscillations, as well as increasing power with increasing stimulus intensity.

Models of the PING network have shown that pyramidal cells alone are not capable of supporting the high frequency oscillations seen in the γ band. Adding an external high frequency stimulus directly to modelled pyramidal cells results in a brief increase in γ band activity, but was not sustained in a way that is shown in MEG recordings[139,140]. The addition of inhibitory interneurons in a ratio of 4:1 (pyramidal cells:interneurons) caused the formation of sustained γ band activity[138]. Several studies have suggested the types of interneurons that can be at work in this model. Optogenetic studies have shown interneurons expressing a calcium binding protein (parvalbumin) are the only ones capable of supporting the high frequency firing seen in γ oscillations[140].

4-1-3 MEG signal analysis

MEG experimental designs tend to be trial based. This means they are either a repeating stimulus or task given to participants, trials response signals can then be averaged over time. A notable exception however is in resting state scans, where no trial is provided, and one continuous block of data is collected instead. Averaging poses a challenge to analysing data however. If data collected is in phase i.e. the peaks and troughs of the response waves are locked to the stimulus onset, then when each trial is averaged the resulting waveform is similar to individual response waveforms. However, if responses are not phase locked to the stimulus onset then averaging of trials will result in a flattening out of the waves, and averaging to the baseline recording. These types of responses are instead time-locked to the stimulus onset, and therefore are called induced responses (as opposed to evoked responses, when waveforms are phase-locked to a stimulus). Two types of analysis must be performed to measure each type of activity; time-frequency analysis and event-related field (ERF) analysis (or event related potential – ERP – in EEG studies) respectively. For time-frequency analysis a measure of the power in a certain frequency bandwidth can be obtained prior to averaging. Techniques such as the Hilbert transform allow this, and is done by plotting a line over the peaks of responses at a given frequency bandwidth, meaning the phase of responses does not affect resulting power estimations during averaging.

Following collection, a number of procedures must be taken to make use of the data generated by the SQUID array. Generally, studies need to localise the source of any data collected to make sense of where the signals that have been measured are coming from. To do this a 3D reconstruction must be made from an essentially 2D array of sensors. It is here that we encounter the forward, and inverse problems. The forward problem is: given a known source of signal – its position, strength and orientation – in this case neuronal currents, how would this be recorded by the SQUID array given the conductivity of the subjects' scalp. The inverse problem is more difficult to solve, and is required for source localisation. Given an external magnetic field, such as the ones recorded from the SQUID array, what is the source of the underlying current? As the possible combinations of any current source generating a particular magnetic field is infinite, any solution is constrained using apriori knowledge[141–143].

The technique used in this thesis to solve the inverse problem is a spatial filtering technique known as beamforming, specifically synthetic-aperture magnetometry (SAM) beamforming using a multiple spheres model to solve the forward problem[142,144]. Beamforming is a technique that acts to localise sources by comparing two states, active and baseline. In SAM beamforming, an attempt to solve the inverse problem is approached by matching dipoles within a grid containing source locations while attempting attenuating signals from all other sensors. SAM is different from other beamforming methods in that the algorithm attempts to match a dipole orientation that delivers the maximal source to noise power ratio by applying a weighting to each sensor individually, altering the contribution this makes to any statistical map. Weighting is calculated using a series of covariances from each sensor and the covariance matrix between sensors[142]. Statistical parametric maps are generated to differentiate between active and rest/control periods (pseudo-T statistic).

From this a 'virtual sensor' can be created over a region of interest (ROI) with a high pseudo-T statistic i.e. a region which has been calculated to have a high signal and dipole orientation solution from the available data, data is then generated according to this ROI.

A 3D anatomical T_1 MRI image is used to spatially constrain the SAM beamformer[144]. This is done by estimating the shape and conductance of the scalp at each sensor, by registering sensor locations to the anatomical MRI image. This helps to solve the forward problem mentioned earlier and aids in the generation of weights for any possible source of magnetic field measured.

Chapter 5: Impaired cerebrovascular reactivity in Multiple Sclerosis and its restoration with immunomodulation measured using breath-hold functional MRI

Disclaimer: Data shown in this chapter was collected by a collaborating research group, along with supervisor Dr. Valentina Tomassini at the Sapienza institute in Rome. The trial design was developed by Valentina. Patients were recruited, and the breath hold task were all performed and recorded by the collaborating group. The data was analysed by me (Marek Allen) to test my hypothesis that cerebrovascular reactivity is altered in multiple sclerosis patients.

5-1 Abstract

Cerebrovascular reactivity (CVR) is the ability of blood vessels to dilate in response to a vasoactive stimulus, resulting in an increase in cerebral blood flow (CBF). Preserved CVR is crucial to maintaining proper neurovascular coupling in healthy brains. There have been some studies to suggest that vascular function may be compromised in multiple sclerosis (MS), but to my knowledge none has investigated the effects of treatment on CVR in these patients. Here I aimed to use a hypercapanic challenge (breath holding) to observe how CVR is altered in MS patients compared to healthy volunteers, as well as assessing how CVR is altered in MS patients both before and after commencement of treatment with interferon-beta 1a (IFN-beta). Patients were scanned twice prior and once after commencement of IFN-beta 1a treatment. CVR was calculated as a percentage increase in BOLD response /mmHg during a series of breath holds, with end-tidal CO_2 being recorded throughout. Group analysis was performed for global and regional CVR alterations in patients compared to controls. A significant decrease in gray matter (GM) CVR was observed in patients' first scan compared to controls. Further analysis revealed patients with enhancing gadolinium lesions had a significantly higher CVR than those not currently exhibiting active inflammation ($p<0.05$). CVR was normalised in both patient groups (those with, and without gadolinium enhancing lesions), following commencement of IFN-beta 1a treatment. My findings suggest an impairment of vascular function in MS patients due to inflammation, and that this can be restored following treatment of an immuno-modulator.

5-2 Introduction

Multiple sclerosis (MS) is a chronic, inflammatory, demyelinating disease of the central nervous system (CNS). MS is generally considered a T-cell mediated disease, but macrophages, B-cells and monocytes all play a crucial role during inflammation. Degradation of the endothelial blood brain barrier (BBB) around blood vessels allows entry of immune cells into the brain parenchyma leading to demyelination and the classical lesions seen in post mortem tissue samples and 'black hole' lesions on T_1 MRI images[9,27,64]

Cerebrovascular reactivity (CVR) – a process essential for neurovascular coupling – is the capacity of blood vessels to alter flow within the brain in response to a vasoactive stimulus. Previous work by other groups has demonstrated disruption to CVR in inflammatory conditions, including multiple sclerosis[90,145–147]. Basal tonic action of endothelial nitric oxide synthase (eNOS) producing low levels of nitric oxide (NO) is crucial to maintaining vascular tone and regulation of vascular resistance in response to CO_2[52,148]. Disruption of the endothelium, as seen during inflammation, and breakdown of the BBB – primarily mediated by IFN-γ and TNF-α – causes a reduction in endothelial-derived NO, as well as an increase in endothelin-1 expression, a potent vasoconstrictor[52,149]. An inability to regulate vascular tone would lead to disruption of basal cerebral perfusion, as well as disruption of CVR. Without adequate supply of essential metabolic substrates during neuronal activity, further cerebral damage and cerebral degradation could ensue, because of this, maintenance of CVR is vital to reducing any damage caused during demyelination[36,47,51].

While the mechanism of CVR attenuation is unknown, there is the increasing evidence of inflammation playing a key role[48,150]. Alteration of CVR by an immunomodulator would provide evidence for inflammation being a cause of CVR attenuation, and can be assessed through several techniques such as hypercapnia elicited through either CO_2 inhalation, breath hold (BH) task or through administration of acetazolamide[28,146,151].

Here I investigated how CVR is affected in MS and if any attenuation can be linked to inflammation. This was done using a breath hold task to elicit hypercapnia-induced hyperaemia, through which CVR can be assessed in MS patients. Patients were administered with an immunomodulator as part of their treatment, and returned for an additional scan and a repetition of the breath hold task. CVR measures were compared to healthy controls to examine the effect MS has on CVR and if any attenuation is restored to normal levels following immunomodulator administration.

5-3 Methods

5-3-1 Participants

25 patients with a diagnosis of MS (mean age 36±7 years, range 29-46, mean EDSS 1.5 range 0-3, 5 males 20 females, disease duration 22±31 months, range 3-138 months) according to the revised diagnostic criteria (Polman C et al, 2005) and eligible to start IFN beta treatment, and 19 healthy volunteers (mean age 34±8 years, range 28-51, 6 males, 13 females) were recruited at Sapienza University of Rome (table 5-1). Steroid administration and relapse within 3 months were exclusion criteria. Patients were assessed using behavioural and MRI measures twice before (at session 1, week -6±1, and at session 2, baseline) and once after (at session 3, week +12±1) the beginning of IFN beta 1a treatment (44 mcg (Rebif®, Merck Serono) subcutaneously administered 3 times weekly). Age- and sex-matched healthy volunteers were assessed behaviourally and with MRI at baseline only. Participants were not asked to alter their lifestyle habits prior to scanning. Participants' consent was obtained according to the Declaration of Helsinki. All participants gave written informed consent according to the protocol approved by the local Ethics Committee.

5-3-2 MRI acquisitions

Functional and structural MR measurements were acquired using a Siemens Magnetom Verio 3T/70cm bore magnet (Siemens healthcare, Siemens, Germany). Whole brain functional images with BOLD (T2*) contrast during the breath-hold task were obtained using gradient echo echo-planar imaging during the breath-hold (BH) task (TR/TE = 3000/30ms, 64x64 matrix, 50 transverse interleaved 3mm slices, voxel size 3x3x3mm, FOV 192mm, flip angle 89°, 92 volumes). Field maps were generated (TR = 488ms, TE1 = 4.92ms, TE2 = 7.38ms, 3mm slice thickness, 36x3mm interleaved transverse slices, FOV 250mm, 64x64 matrix, flip angle 60°) for each individual to aid registration.

Patients underwent conventional MRI acquisitions that included T1-weighted images (T1-WIs) (TR = 550 ms; TE = 9.8 ms; FOV =240 mm; matrix=320×320; 25 axial slices, 4 mm thickness; 30% gap), acquired 5 minutes after the administration of Gd to detect the presence and quantify the number of

Gd-enhancing lesions; proton density and T2-WIs (TR= 3320 ms; TE1= 10 ms; TE2= 103 ms; FOV= 220 mm; matrix= 384 × 384; 25 axial slices; 4 mm thickness; 30% gap) to quantify T2-hyperintense lesions. High-resolution anatomical (1mm voxel size) T1-weighted scans (TR/TE = 1900/2.93ms, 256x256 matrix, FOV 260mm, 176 1mm sagittal slices, flip angle 9°) and whole brain diffusion images (72 interleaved slices at 2mm thick, FOV 192mm, TR/TE 12200/94ms, 30 directions, 96x96 matrix, b-value 1 = 9s/mm^2, b-value 2 = 1000s/mm^2) were also acquired to quantify grey and white matter integrity.

5-3-3 Acquisition and analysis of CO2 traces

During the fMRI, participants were asked to perform a breath-hold task. To ensure subjects performed the task adequately, participants were trained to perform it prior to scanning. The breath-hold task consisted of 5 repeats of 16s of end-expiration breath-hold alternated with 34s paced breathing as a recovery[152]. In the scanner, task instructions and pacing were visually presented using a MRI-compatible stimulus-presentation system with the use of goggles (VisuaStim Digital system from Resonance Technology Inc, Northridge, California). End tidal CO_2 ($EtCO_2$) was measured via nasal cannula (Veris monitor, Medrad).

The CO_2 traces (figure 5-1 shows average CO_2 traces for patients and controls) were used to model blood oxygenation level dependent (BOLD) functional MRI time courses to give the CVR maps. Individual CO_2 peak delays were calculated to determine how far each CO_2 trace had to be shifted prior to being used as a regressor in a later GLM analysis. This was done by extracting individual GM time series data using fslmeants (part of the FSL toolbox) from BOLD data and performing a cross correlation with corresponding end tidal CO_2 traces from that subject's scan session. Each delay was used to positively shift CO_2 traces before being added to a GLM model. In addition to this end tidal CO_2 traces were averaged across controls and patients to create an average time delay for patients and controls. If cross correlation could not find an optimal time delay or an individual subjects' delay was greater than 2 standard deviations away from the group mean, CO_2 traces were shifted using a delay within 2 standard deviations and with the highest correlation with the group average.

5-3-4 MRI analysis

fMRI data were analysed with FSL-FEAT[153]. Pre-processing of data was performed prior to model fitting of the participants' time series. This included: a high pass cut-off of 100s was used, motion correction using MCFLIRT [154], non-brain removal using BET [155] and B0 unwarping using PRELUDE and FUGUE (EPI echo spacing 0.53ms, EPI TE 30ms, unwarp in –y and signal loss intensity threshold of 10%). Functional images were linearly registered using FLIRT[154], first to subject's T1 structural scan limited to 6 degrees of freedom, then to the Montreal Neurological Institute (MNI) 152 space with 12 degrees of freedom. The time series was analysed using a general linear model (GLM) approach with local autocorrelation correction. To obtain a BOLD response map for each participant, shifted end tidal CO_2 traces were demeaned and entered as regressor in the GLM. Gamma convolution was applied to model haemodynamic response function (HRF) along with an additional temporal derivative (to represent a regressor of no interest) and temporal filtering. Group level analysis comparing healthy volunteers to patients at each time point incorporating GM density (by creating a 4D image containing each subjects' GM segmented masks) and the presence of gadolinium enhancing lesions (a marker of acute inflammation) as covariates was performed (appendix A). This allowed for the assessment of the effect GM density and the presence of active inflammation might have on CVR. All analyses used a corrected threshold of $p < 0.05$, $Z > 2.3$. GM density images were generated as part of FSL VBM structural analysis outlined below, these were included in the group analysis to account for GM density differences between patients and controls. Percent BOLD signal change was extracted using FEATQuery, part of the FSL toolbox[156].

Region of interest analysis (ROI) was performed to determine GM CVR values. Masks were created by overlaying MNI masks on to BOLD response maps generated as part of first level analysis. Masks were generated by transforming MNI masks to functional space to avoid interpolation errors. Registration was achieved using FSL-FLIRT, functional images were first registered to high resolution space, then to MNI space, resulting transformation matrices were inverted and applied to the registration[154]. Only non-empty masks were reported. Subject data were then divided into groups based on those with and

those without Gd enhancing lesions (determined using T2-WIs) to assess the extent inflammation altered CVR. All brain functional activations were labelled using the Harvard-Oxford Structural, and subcortical atlases (http://www.fmrib.ox.ac.uk/fsl/data/atlas-descriptions.html). Here I generated masks corresponding to the anterior and posterior cingulate, insula, thalamus, frontal, occipital, parietal and temporal lobes.

5-3-4-1 Structural analysis

We tested the relationship between grey and white matter integrity and changes in CVR in the patients. High resolution T1-WIs were analysed with FSL-VBM [157] with an optimised protocol[158]. T1 images were brain extracted, segmented using the FAST segmentation tool and registered to MNI152 standard space using non-linear registration. A grey matter (GM) template was created using all 19 controls and 19 randomly selected patients' session 1 or 2 scans. GM images were then registered to this template and corrected for local distortions due to registration. These were smoothed with an isotropic Gaussian kernel (σ=3mm). VBM was then performed on all subject datasets, comparing GM density of each patient's session scans to controls.

Voxelwise statistical analysis of the T2 images to extract FA values was carried out using TBSS (Tract-Based Spatial Statistics[159]), part of FSL[156] and was used to assess WM tract integrity. TBSS projects all subjects' FA data onto a mean FA tract skeleton, before applying voxelwise cross-subject statistics. Voxelwise GLM was applied, testing for differences in FA between healthy volunteers and patients at each time point, using permutation-based non-parametric testing set at a threshold of p<0.05 corrected for family-wise error.

Brain volume estimation at baseline (session 1) was performed using SienaX[160] part of FSL[153]. Following brain and skull extraction the brain was affine registered to MNI-152 space using the skull to determine scaling. Tissue was segmented using FAST and partial volume estimation was performed to calculate total volume brain tissue and allowing separate estimates for GM, WM and CSF. Gd lesion

volume and presence was assessed using T_2 images obtained following gadolinium administration, images were analysed using JIM software (Xinapse Systems Ltd, Essex, UK).

5-3-5 Statistics

A two-way ANOVA, modelling changes in GM CVR across time-points and presence of active inflammatory lesions was carried out to investigate CVR differences at a group level, the factors considered in these models were time and the presence of Gd-enhancing lesions. From this, a repeated measures one-way ANOVA was performed on each ROI, investigating the effect of time-point on GM CVR. Individual percent BOLD signal change values were used in each ANOVA. Pearson correlation between WM FA values and CVR values extracted from BH data was performed to investigate any correlations between WM FA, lesion volume, lesion presence, and time-point was also done. Finally, student t-tests were performed comparing pairs of patient CVR at each time-point and ROI for differences between those with active inflammation and those without.

5-4 Results

5-4-1 Behavioural task

To determine that subjects were performing the breath hold task adequately T-tests were performed on extracted time delays to compare means of each group (fig. 5-1). Both patients and controls performed all 5 BH challenges with no significant difference in delay times either between groups or before and after treatment. 4 $EtCO_2$ files (3 patients, 1 controls) were corrupted and replaced with a substitute from another scan by those subjects (where available). Of the 25 patients, only 19 completed all 3 scan sessions with the largest drop out seen between scan 2 and 3. 2 of these patients had one $EtCO_2$ file replaced with another from a different scan. 14 patients were found to have gadolinium (Gd)-enhancing lesions in their first scan with 11 patients exhibiting the lesions during their second scan. During treatment and the third scan, this number was reduced to only 3 patients' scans containing Gd-enhancing lesions (figure 5-2). There was no alteration to the EDSS scores assigned prior to any of the 3 scan sessions. In patients, the mean time intervals were 45±2 days, 85±2 days and 73±3 days for scan 1-scan 2, scan 2-scan 3 and commencement of treatment-scan 3 respectively. The mean duration between scan 2 and onset of IFN-β1a treatment was 11±2 days.

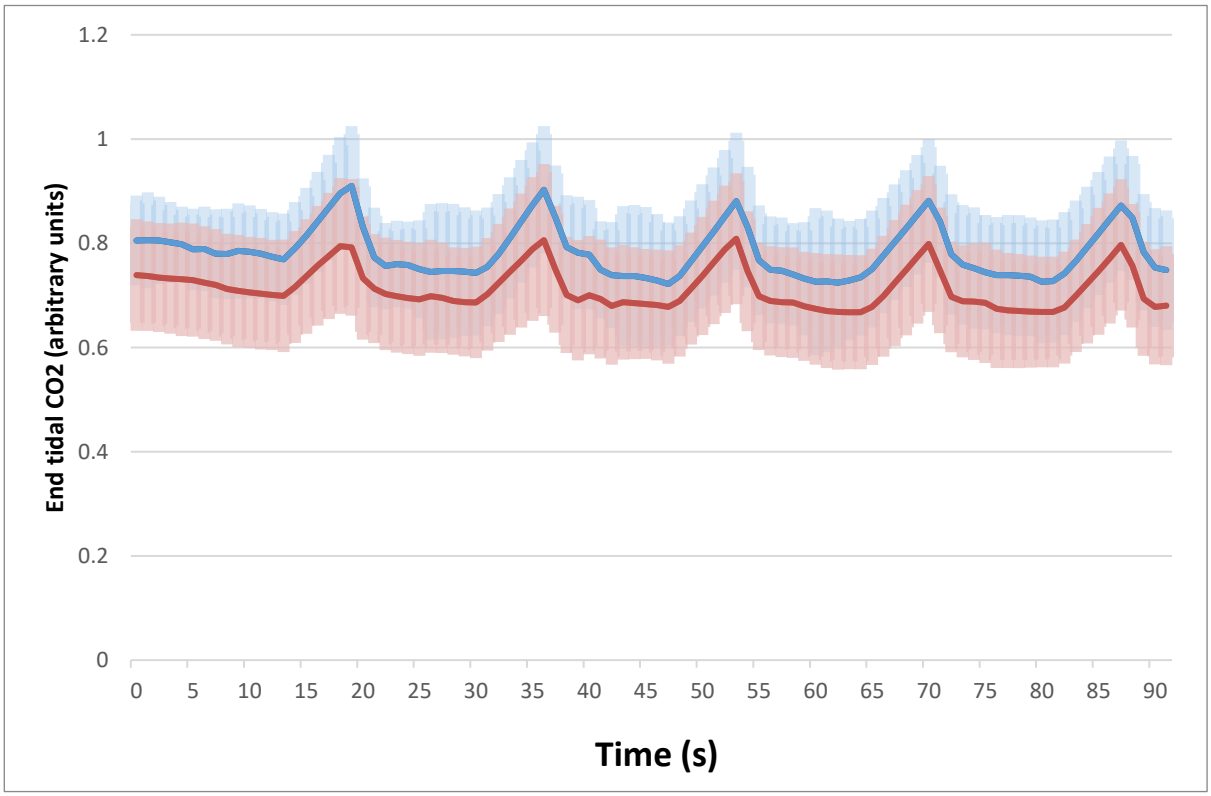

Figure 5-1 Averaged CO_2 traces of healthy volunteers (blue) and MS patients (red) from their first scan. Shaded areas represent each group's respective standard deviations. Each peak in end tidal CO_2 represents each rise in CO_2 concentration following a breath hold. Healthy volunteers had a slightly higher end tidal CO_2 than patients, but this difference was not statistically significant.

5-4-1 Grey matter, white matter and brain volume

A grey matter (GM) voxel-based morphometry (VBM) comparison revealed a decrease in GM density bilaterally in the thalamus of patients compared to controls (FWE corrected, TFCE thresholded $p<0.05$) (figure. 5-3). FSL TBSS demonstrated widespread decreases in white matter FA in patients compared to controls (figure. 5-4). Patients demonstrated a significantly lower WM FA on all three scan sessions (3.6±1% $p=0.01$, 4.3±2% $p<0.05$, 3.5±1% $p=0.01$ for scan session 1, 2 and 3 respectively) compared to controls.

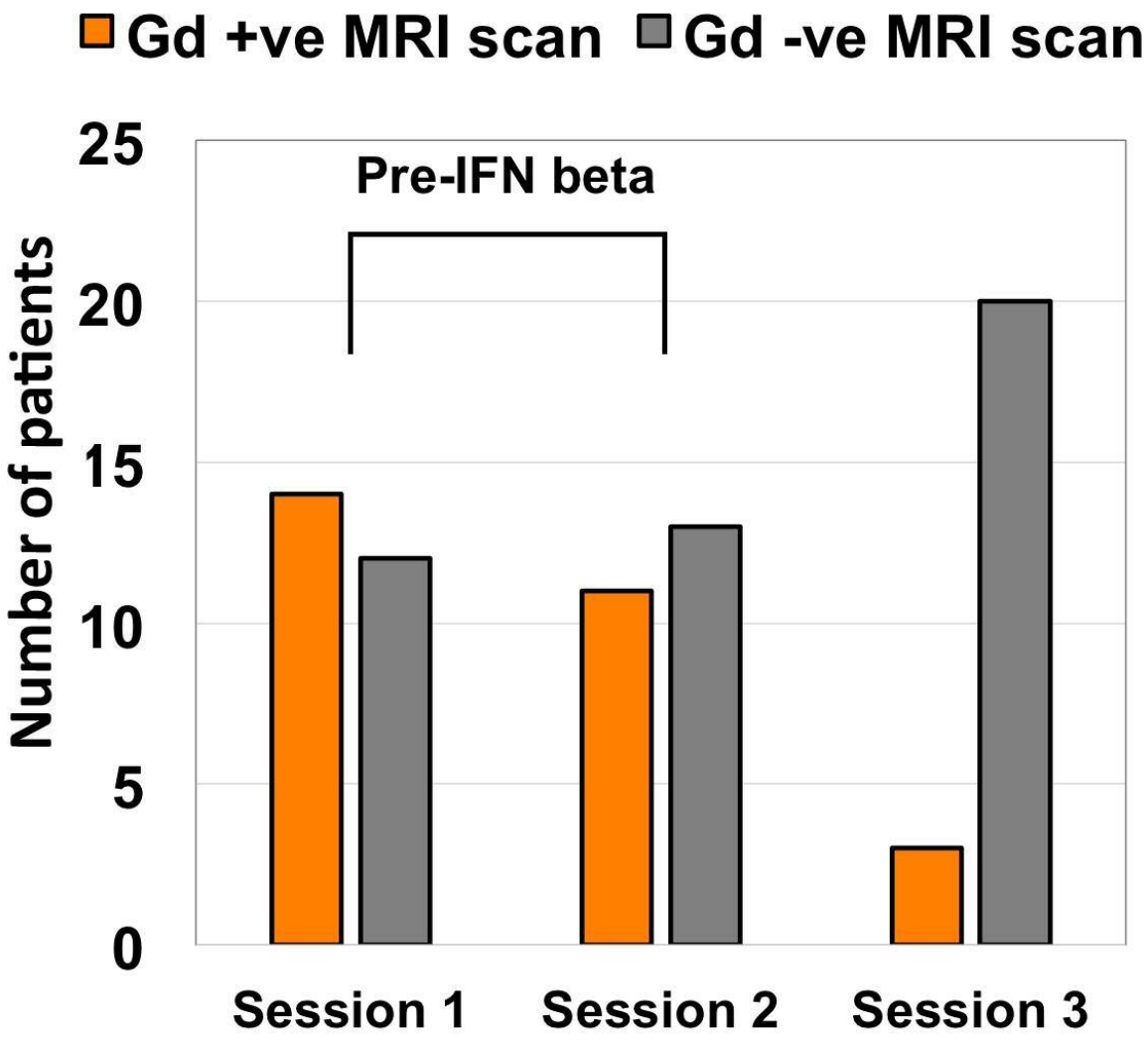

Figure 5-2 Number of patients entering final analysis showing gadolinium-enhancing lesions. 14 and 12 patients at the first and second time points showing gadolinium enhancing lesions respectively. Following treatment with interferon-β only 3 patients exhibited enhancing lesions.

	Controls (19)	Patients (25)			*p*
Age$_{mean}$ (Range)	34 (28-51)	36 (29-46)			0.4
Males/females	5/14	5/20			0.3
EDSS score, median (Range)	-	1.5 (0-3)			-
Disease duration in months, mean (Range)	-	22±6			-
Number of gadolinium enhancing scans, total (scan 1,2 and 3)	-	14	11	3	0.4
Lesion volume (mm^3), mean ± SE	-	1708.6 ±418.6	1819.7 ±428.7	1841.7 ±451.8	0.4
25 foot walk, mean ± SE (seconds)	5.3	5.8	5.8	5.5	
9-hole peg test, mean ± SE (seconds)	15.78	17.8	16.8	15.8	
PASAT 3 seconds, mean ± SE (seconds)	49.1±2.2	43.1±1.9	48.5±1.9	50.3±1.5	
PASAT 2 second, mean ± SE (seconds)	40.7±2.4	33.8±2.2	36.7±1.7	40.3±2.1	

Table 5-1 Demographic, clinical and MRI characteristics of the participants. The 9-HPT and T25-FW are expressed as the mean of two trials. T-tests were performed for between group comparisons, one-way RM ANOVA was used for between timepoint comparison.
Abbreviations: *EDSS=Expanded Disability Status Scale; 9-HPT= 9-hole peg test; PASAT= Paced Auditory Serial Addition Test; SE=standard error; T25-FW= timed 25-foot walk.*

5-4-2 Vascular reactivity

Patients exhibited a significantly lower whole brain grey matter BOLD response, my index of vascular reactivity, during breath hold compared to controls during their first scan session (19.9±9.4% lower CVR, $p<0.05$). A strong trend for a 12.5% (±6.3%) lower GM CVR was detected during the second scan

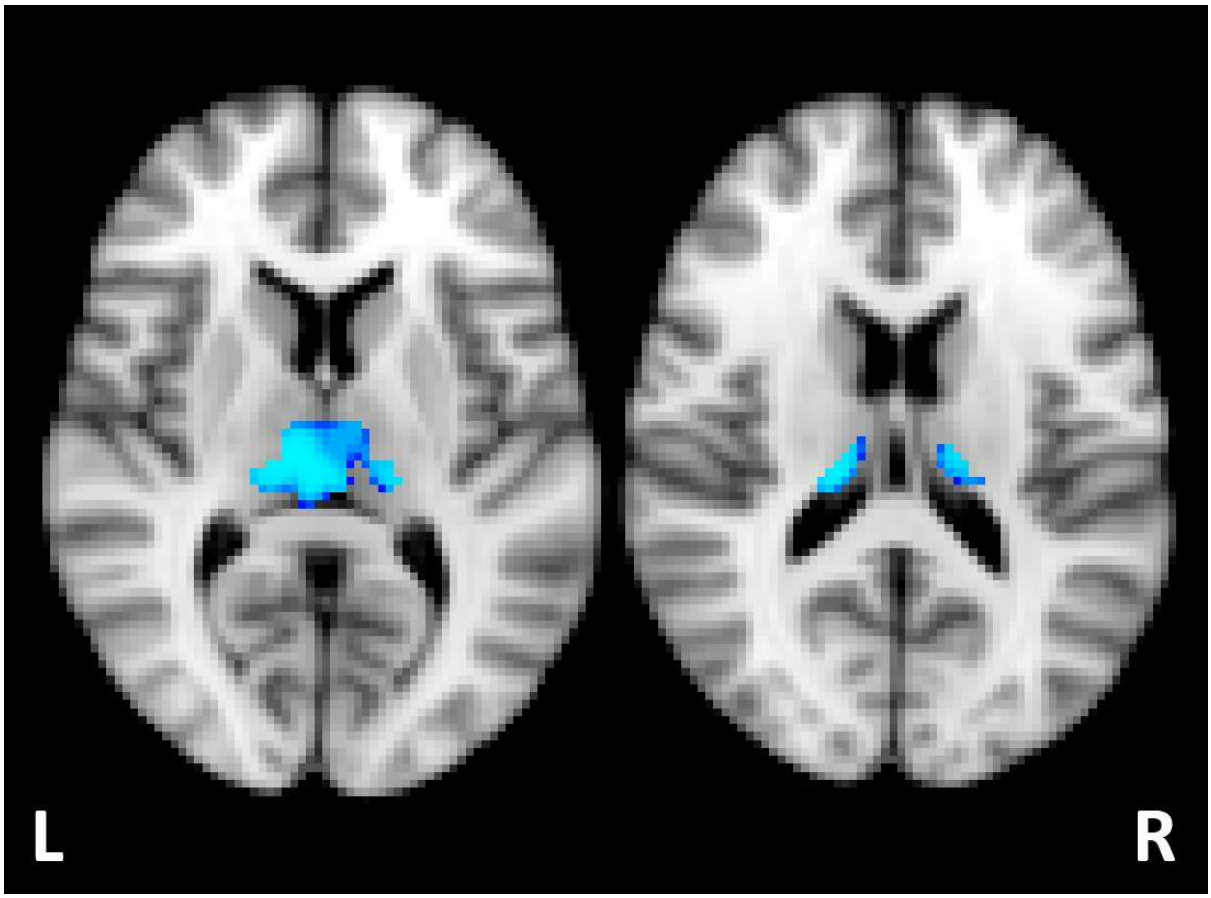

Figure 5-4 Visualistion of VBM results comparing GM densities of patients to healthy controls. A significant decrease in grey matter density was observed bilaterally in the thalamic region in patients (TFCE thresholded, FWE corrected p<0.05).

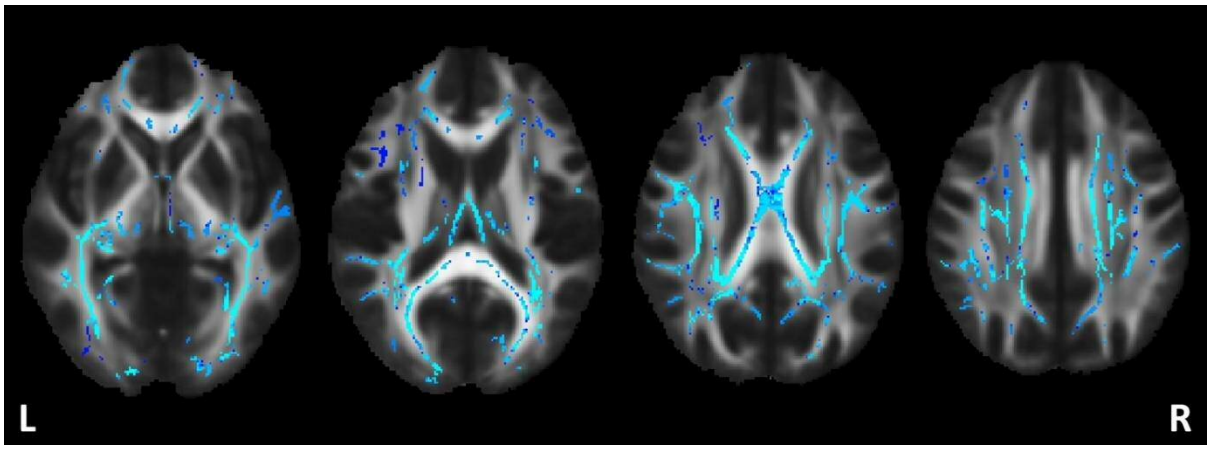

Figure 5-3 Visualisation of TBSS results comparing WM FA in patients to controls. A significant global decrease in WM FA is observed in patients (TFCE thresholded FWE corrected P<0.05).

session compared to controls (p=0.07). This was partially normalised following commencement of IFN beta treatment with only an 8.7% lower (±5.5%) GM CVR, compared to controls, exhibited in the third scan session (p=0.3). One-way within subjects (repeated measures) ANOVA confirmed no significant

difference in whole-brain GM CVR between patient groups at any time point was noted (p=0.5) (figure 5-5).

Patients with and without active inflammation were then separated and compared to controls, this revealed large differences in the CVR within time points. Overall patients exhibited a 20% lower GM CVR ($p<0.05$) during their first scan session, however those patients with active inflammatory lesions only demonstrated a 9.5%(±10.4% N.S.) lower GM CVR compared with controls. Patients without active inflammation had a significantly reduced GM CVR compared to controls of 29.4%(±15.2% p=0.01). A similar trend was observed in the second time point; those with active inflammation displayed a GM CVR similar to that of controls (100%±3.5 N.S.). Those without active inflammation exhibited a reduced GM CVR of 21%(±9.5% $p<0.05$), compared to controls. Group level voxelwise analysis can be seen in figure 5-6 where mean CVR maps of patients' first and second scans are shown, along with regions of enhanced CVR due to the presence of gadolinium enhancing lesions. Following commencement of IFN beta treatment there were no significant differences in GM CVR in either cohort of patients (those with or without active inflammation) compared to controls (15.4%±7.7 reduction and 11.8%±8 reduction for active and inactive patients respectively) (figure 5-7).

Table 5-2 summarises ROI analysis performed following whole brain GM CVR assessment. Group level analysis demonstrated a significantly lower CVR in the frontal and occipital lobes, insula cortex, precentral gyrus as well as the anterior and posterior cingulate cortices in patients compared to healthy volunteers. Extracting CVR values from each subjects' ROI to assess CVR in those patients with and without active inflammation revealed that as with global GM CVR, patients with active inflammation exhibited a higher CVR than those without active inflammation. The frontal lobe, insula, precentral gyrus and thalamus all demonstrated a significantly lower CVR in patients without active inflammation than those with, across timepoints 1 and 2 (frontal lobe; 45% lower p=0.01, 39% lower $p<0.01$. Insula; 52% lower p=0.01, 37% lower $p<0.05$. Precentral gyrus; 47% lower p=0.01, 33% lower p=0.01. Thalamus; 37% lower p=0.05, 40% lower $p<0.01$ respectively). Comparing patient subgroups

to control values revealed a significant alteration in CVR in patients' scans prior to treatment in frontal ($p<0.01$) and occipital lobes ($p<0.05$), insula cortex ($p<0.01$), precentral gyrus ($p<0.01$) as well as the posterior cingulate ($p<0.01$).

Treatment with IFN beta reversed these differences (all values are percentage CVR differences in patients without active inflammation relative to patients with active inflammation: frontal lobe; 6% higher p=0.4, insula; 7% higher p=0.4, precentral gyrus; 11% higher p=0.3, thalamus; 2% higher p=0.4). There was a trend for IFN beta to assist in the restoration of CVR in patient subgroups in the anterior

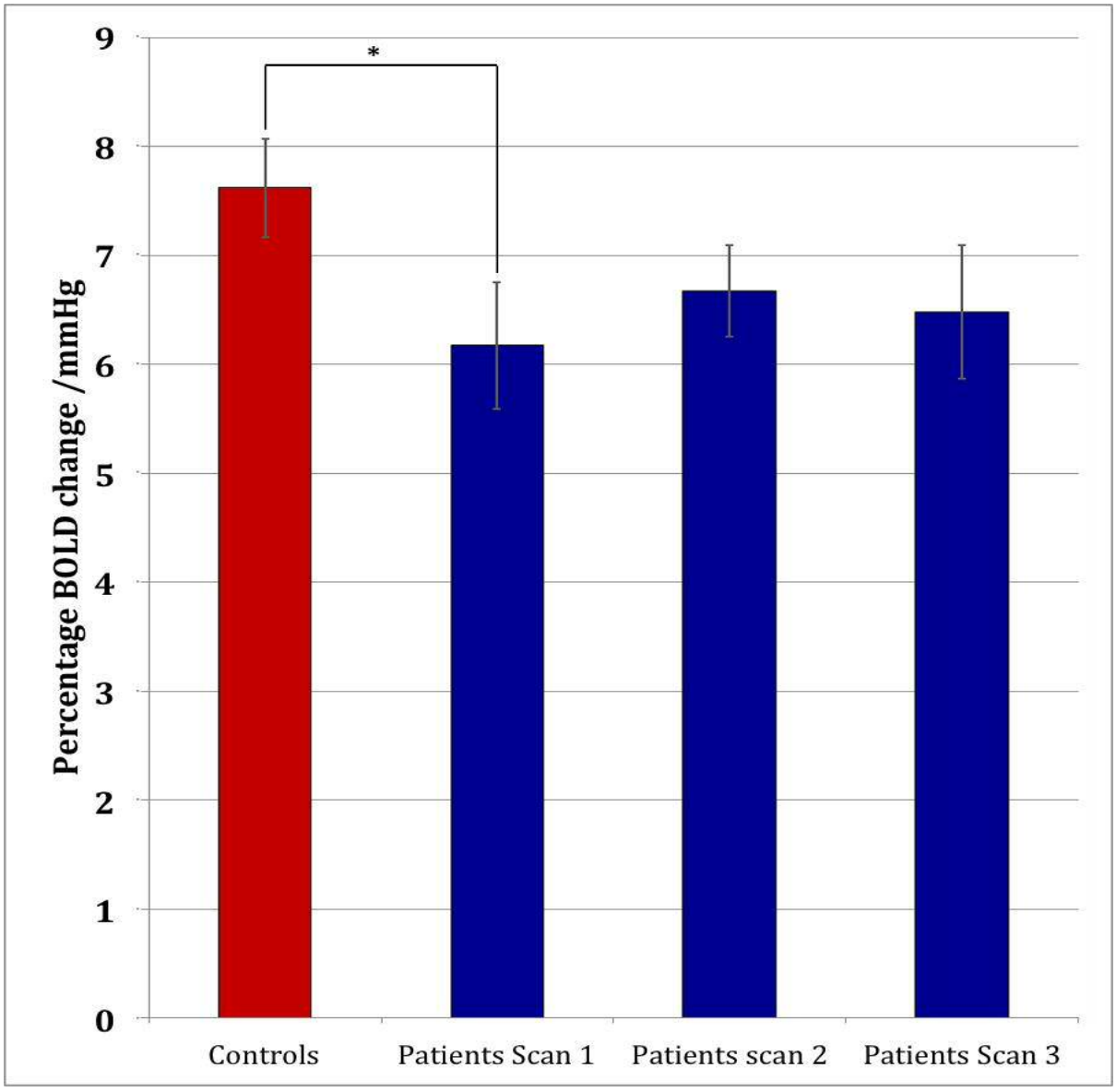

Figure 5-5 Percentage grey matter BOLD increases during breath hold comparing healthy controls to patients at each time point. There is a significant decrease in breath hold related BOLD increases in patients during their first scan compared to controls ($p<0.05$). Following treatment with interferon-beta with no significant differences between patients scan 3 and controls.

and posterior cingulate cortices and occipital lobe, but did not reach overall significance ($p=0.1$, 0.2 and 0.1 respectively compared to the frontal lobe $p<0.05$, insula $p<0.05$, precentral gyrus $p=0.05$ and thalamus $p=0.05$). Comparing these values to controls however, revealed that IFN beta treatment returned CVR values to a comparable level with controls, no significant differences in CVR at any ROI, at any time point or patient subgroup detected compared to controls (figure 5-8).

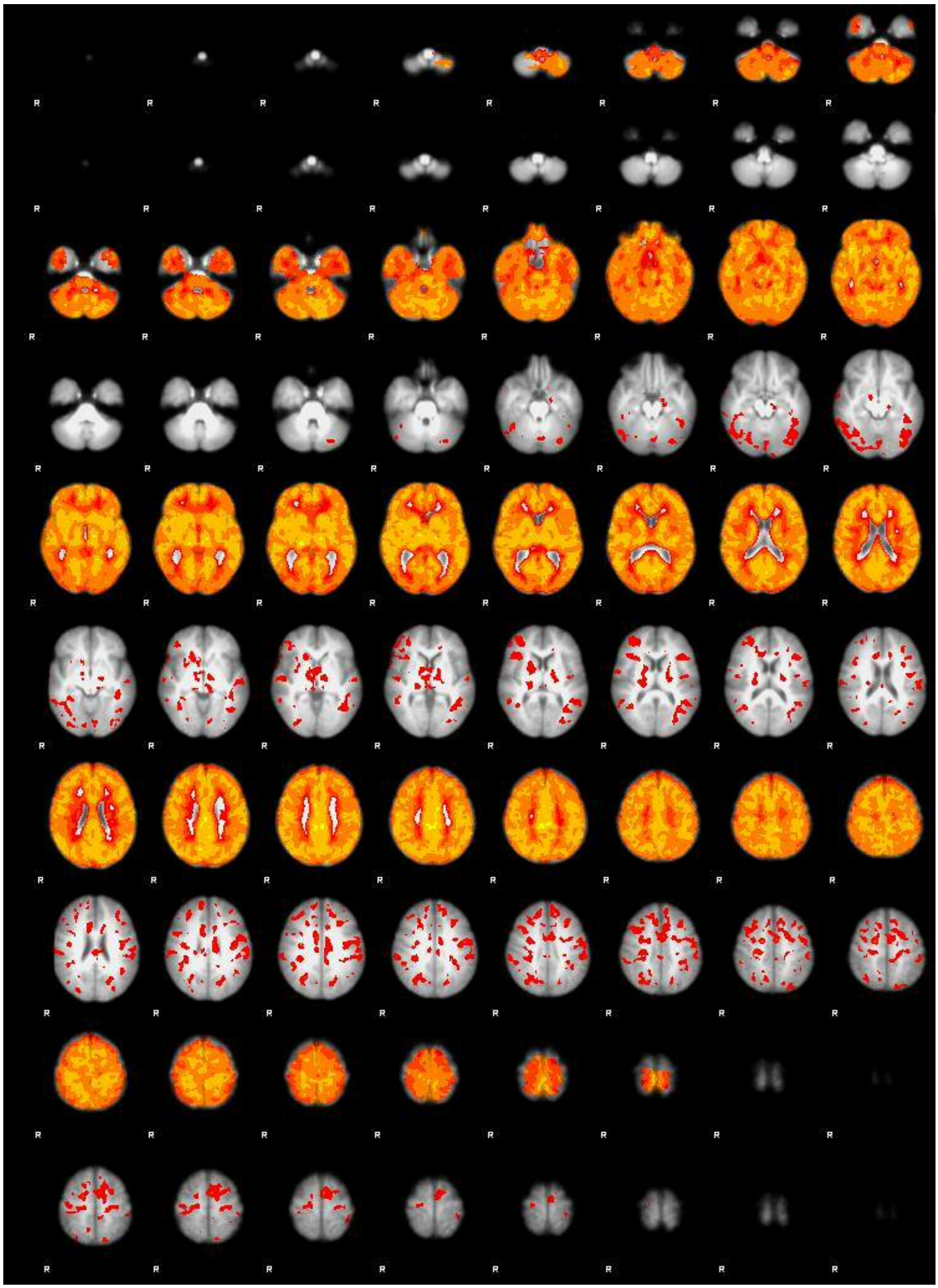

Figure 5-6 Voxelwise group analysis results of patients' scan 1 and scan 2 average z-statistic maps (top row and every other row thereafter) compared to regions of significantly increased CVR due to the presence of gadolinium enhancing lesions in those patients (second row down and every other row thereafter). Images have a threshold of z>2.3 applied, no cluster thresholding.

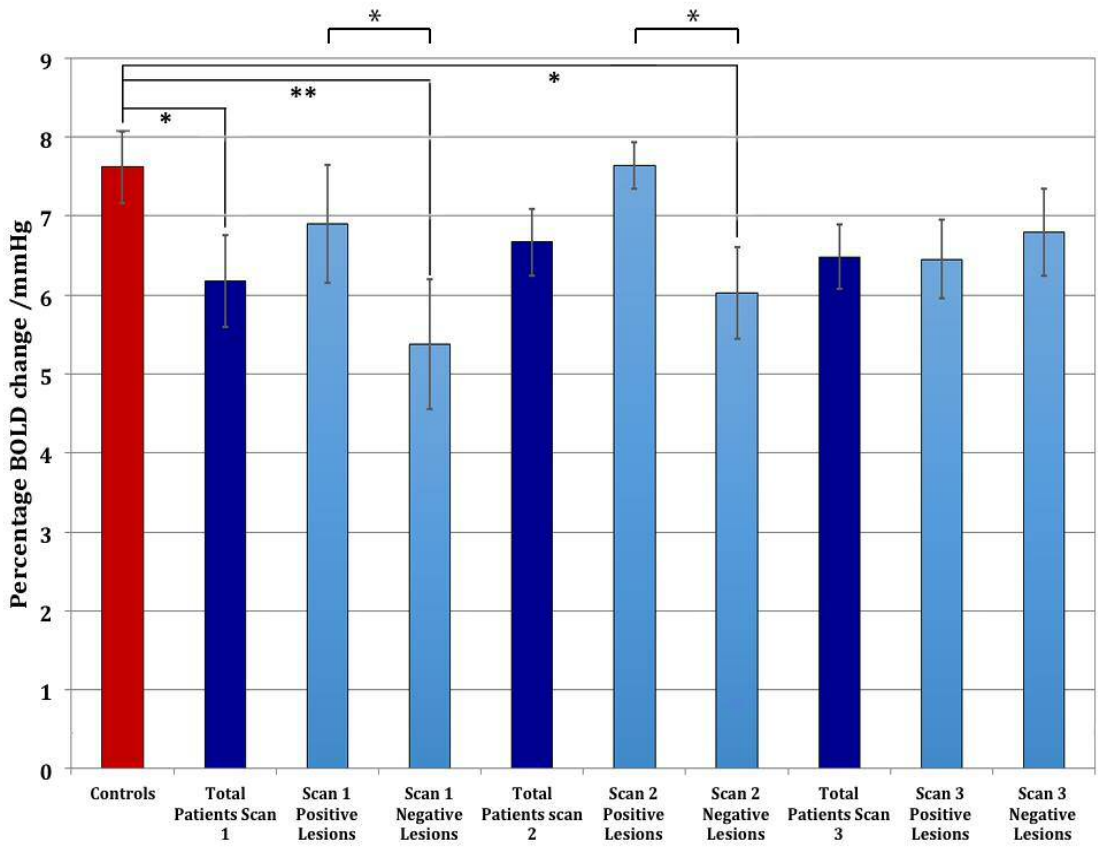

*Figure 5-7 Percentage BOLD differences /mmHg during breath hold comparing healthy controls to patients at each time point separating patients with active and inactive inflammatory lesions. One way ANOVA on ranks revealed a significant difference between CVR of patients with active inflammation and those without in the first two scans ($p<0.05$), with no significant difference detected on the third scan following IFN-β treatment. There was no significant difference in the CVR of patients with active inflammatory lesions and healthy controls ($p=0.5$). However, there was a significant decrease in CVR in patients without active inflammatory lesions in scan 1 ($p=0.01$) and in scan 2 ($p<0.05$) compared to controls. This was normalised following commencement of interferon-beta treatment ($p=0.3$). * = $p<0.05$, ** = $p<0.01$*

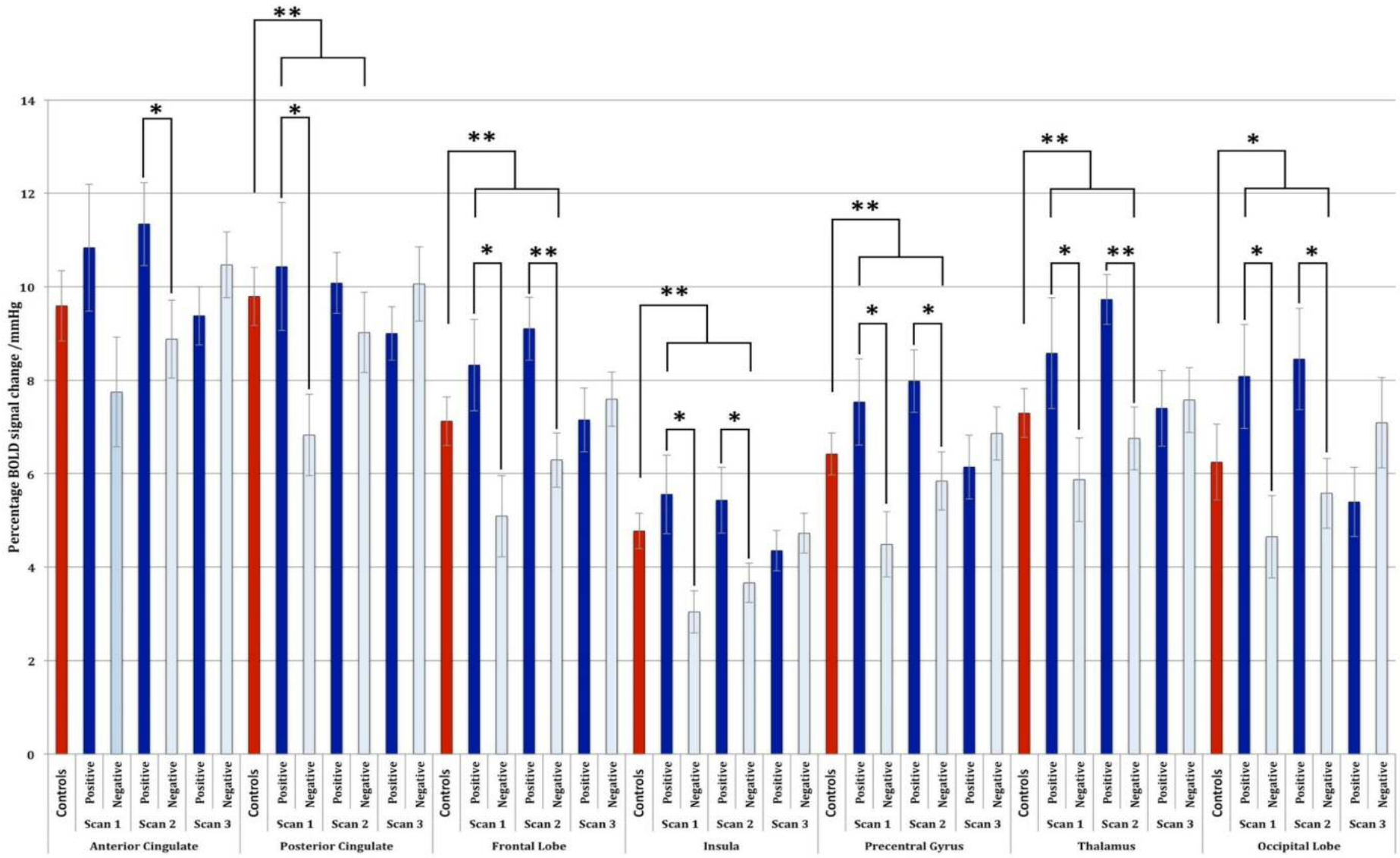
Percentage BOLD signal change /mmHg
0
2
4
6
8
10
12
14
Controls
Positive
Negative
Scan 1
Scan 2
Scan 3
Anterior Cingulate
Posterior Cingulate
Frontal Lobe
Insula
Precentral Gyrus
Thalamus
Occipital Lobe

*Figure 5-8 ROI analysis showing regions of significantly altered CVR in patients with and without gadolinium enhancing lesions compared both within group and compared to controls. In patients the poster cingulate, frontal lobe, insula, precentral gyrus, thalamus and occipital lobe all demonstrated a significantly lower CVR compared to controls. This was then normalised following commencement of IFN-β treatment. Comparing patient sub groups revealed a lower CVR in the frontal lobe, insula, precentral gyrus, thalamus and occipital lobe in patients without active inflammation compared to those with acute inflammation in scans 1 and 2. This was then normalised in both sub groups, to a level comparable with healthy controls following IFN-β treatment. There was a trend for the anterior cingulate to have a higher CVR in patients with active inflammation than those without in the first scan, but did not reach significance (p=0.06). CVR and p values are summarised in table 2. * = p<0.05, ** = p<0.01. Not corrected for multiple comparisons.*

			Group average percent BOLD signal change/mmHg								
			Controls	Patients scan 1	Active vs inactive inflammation p value	Patients scan 2	Active vs inactive inflammation p value	Patients scan 3	Active vs inactive inflammation p value	Across time point p value	Scan 1 and 2 CVR p values compared to controls
ROI analysis	Anterior Cingulate	With active inflammation	9.59	10.84	0.06	11.34	0.03	9.38	0.3	0.53	0.18
		Without active inflammation		7.75		8.88		10.47			
	Posterior Cingulate	With active inflammation	9.79	10.43	0.03	10.08	0.2	9.00	0.3	0.45	0.003
		Without active inflammation		6.82		9.02		10.06			
	Frontal Lobe	With active inflammation	7.12	8.32	0.01	9.10	0.003	7.15	0.4	0.50	0.008
		Without active inflammation		5.09		6.29		7.59			
	Insula	With active inflammation	4.77	5.56	0.01	5.43	0.02	4.35	0.4	0.67	0.004
		Without active inflammation		3.04		3.66		4.72			
	Precentral Gyrus	With active inflammation	6.42	7.53	0.01	7.98	0.01	6.14	0.3	0.49	0.003
		Without active inflammation		4.48		5.84		6.86			
	Thalamus	With active inflammation	7.30	8.58	0.05	9.73	0.002	7.40	0.4	0.66	0.006
		Without active inflammation		5.87		6.75		7.58			
	Occipital Lobe	With active inflammation	6.24	8.08	0.01	8.45	0.02	5.39	0.3	0.87	0.03

Table 5-2 Summary of ROI analysis comparing CVR in patients with and without acute inflammation defined as [22]. Total changes in CVR between timepoints was determined by one way repeated measures ANOVA comparing mean CVR of each patient sub-group at each time point. The frontal lobe, insula, precentral gyrus and thalamus all displayed significant differences in CVR over time, with t-tests showing a significant reduction of CVR following treatment with IFN beta, with a trend in the occipital lobe **Abbreviations:** *ROI = Region of interest; BOLD = Blood Oxygenation Dependent. No correction for multiple comparisons was performed.*

5-5 Discussion

The reduction in the number of patients exhibiting gadolinium enhancing lesions following treatment of IFN beta can be used as a marker to confirm the anti-inflammatory effects of IFN beta[5,13]. Inflammation has been shown to cause breakdown in the integrity of the blood brain barrier (BBB), once inflammatory mediators are removed integrity is restored[26]. This information can then be used to infer how the effects of CVR can be attributed to the anti-inflammatory effects of IFN-β.

We have demonstrated a decrease in cerebrovascular reactivity as indexed by BOLD signal changes in RRMS patients in response to hypercapnia, particularly in patients not currently exhibiting active inflammation. While whole brain GM CVR values were not able to demonstrate a significant effect of treatment with IFN beta compared to healthy controls, ROI analysis confirmed a normalisation of CVR following the commencement of IFN beta in patients not exhibiting active inflammation. This effect was particularly prominent in the frontal lobe, insula, precentral gyrus and thalamus, with a trend for treatment effects observed in the anterior and posterior cingulate cortices and occipital lobe but these did not reach significance. This was consistent with the finding that, following commencement of treatment, the number of patients exhibiting gadolinium-enhancing lesions decreased significantly. An effect well documented due to IFN-beta's immunomodulatory effects[56,59,161]. However, no corrections for multiple comparisons was made, meaning some of significance may disappear once correction has been made.

VBM results only showed a decrease in GM density bilaterally in the thalamus, typical of patients early on in their disease stage[40,162]. As EDSS score increases, there is increasing involvement in the pre- and post-central regions along with anterior and posterior cingulate gyri and insula. As large differences in CVR was detected in these regions in patients, particularly in those showing no active inflammation. It is possible that the changes in CVR could be a precursor to GM damage later in the disease course. Restoration of CVR could act to protect these regions – at least partially – from additional stress and damage. However, the effects through which IFN beta could normalise CVR are still not confirmed.

Nitric oxide (NO) is a potent vasodilator released during physiological and pathological states as a method of controlling vascular resistance and blood flow. Cytokines released during inflammation (particularly TNF-α,

IFN- and IL-6) are known to increase activation of inducible nitric oxide synthase activity (iNOS). MS patients have been found to have increased levels of both iNOS activity and [NO], occurring both during relapses of acute inflammation and remission[53,54,58,59,163,164]. Elevated production of NO would result in basal hyperperfusion thereby reducing a vessel's ability to dilate further in response to a vasoactive stimulus and reducing CVR. However, this is not corroborated by the evidence presented here; acute inflammation causes CVR to rise, something that would be less likely in basally hyperperfused subjects.

Several groups have demonstrated patients are instead cerebrally hypoperfused at baseline[47–49,165]. Many studies describing elevated levels of [NO] do not differentiate between RRMS patients in relapse or remission, or those who are primary or secondary progressive. It is therefore possible that NO levels could be affected depending on the disease course at the time of recording. In addition, there is growing evidence to suggest that endothelial dysfunction could be responsible for reductions in CO_2 chemoreception and associated vascular reactivity. Dysfunction in the endothelium has been shown to cause a reduction in CVR in both human and animal models which was then be reversed following administration of an exogenous NO donor. This activity was found to be mediated primarily through eNOS disruption [93,148,166].

Endothelin-1 (ET1), another vasoactive compound is one of the most potent endogenous vasoconstrictors known, working through two receptors – ETa and ETb. ETa receptors (ETaR) are found on vascular smooth muscle and brain endothelial cells which act to cause vasoconstriction[51]. While not typically produced under normal conditions, ET1 is released through several mechanisms including activation by TNF-α, IFN-γ and reactive oxygen species (ROS), all three of which are increased basally in MS[52,167]. Once released it causes vasoconstriction of surrounding arterioles as well as suppressing eNOS activity[47,168]. Suppression of eNOS aids in ET1's vasoconstrictive activity by preventing NO release and normal vasodilation.

This could explain the greater reduction in CVR in patients who were not currently exhibiting active inflammatory lesions, as there is evidence to suggest ET1 is upregulated in the brains of MS patients basally[47]. During inflammation, however, there is a sharp increase in the expression of IFN-γ, TNF-α, IL-6 and IL-4 along with many other pro-inflammatory cytokines. While some of these (notably IFN-γ and TNF-α) increase the expression of ET1, many more activate iNOS found in vascular endothelial cells, with TNF-α also being

implicated in nNOS activation[11,30,54,163,169]. While ET1 decreases eNOS activity it has no effect on iNOS[168]. This allows NO production to proceed and could act to overpower the vasoconstrictory effects of circulating ET1 and producing the enhanced CVR I have demonstrated here (figure.5-8).

IFN beta acts to reduce the expression of pro-inflammatory cytokines such as TNF-α, IL-6 and IFN-gamma and is demonstrated here by the reduction in patients expressing Gd-positive lesions (figure. 5-3). All of these pathways would cause a reduction in both iNOS activity as well as ET1 expression thereby allowing eNOS to function normally[59]. This would cause the normalisation of the CVR responses seen patients during their 3rd scan session.

It is possible that chronic hypoperfusion caused by ET1 expression could be the cause of neuronal energy deficiency occurring following demyelination. A positive feedback loop created as mitochondria experience further distress eventually leading to the release of ROS causing further ET1 release worsening the problem. During acute inflammatory attacks iNOS activity is increased allowing for a temporary increase in CVR. By treating with IFN-beta there can be a break in this positive feedback loop. A normalisation of both [NO] and circulating [ET1] could allow neurons to partially remyelinate, and help restore the energy balance, thereby slowing of the disease course.

There are however, several drawbacks to using BOLD contrast as a method for determining CVR. The BOLD response relies on several factors including cerebral blood flow (CBF), cerebral blood volume (CBV) and cerebral metabolic rate of oxygen consumption (CMRO2). While an increase in CBF can be measured in response to a vasoactive stimulus as I have used here, an alteration in any of the physiological factors mentioned above can cause results to vary. Therefore, this is a non-quantitative measure of CVR. Instead it would be preferable to use other techniques for measuring perfusion such as arterial-spin labelling.

5-6 Conclusions

Here I have demonstrated a decrease in CVR in MS patients who are not currently exhibiting acute inflammation, which is normalised following treatment with IFN-β. Both effects are ameliorated following commencement of IFN beta treatment. It is still unclear as to the mechanisms through which the reduction in CVR could be taking place in this subset of patients or how IFN beta could be exerting its effects. Further work to examine the molecular methods behind this reduction of CVR would require investigation into cytokines present in both subsets of patients, with and without active + inactive inflammation.

Chapter 6: Developing a measure of neurovascular coupling using a combined fMRI/MEG approach.

6-1 Abstract

The present study aims to develop an empirical measure of neurovascular coupling using two alternate stimuli: a reversing square wave checkerboard at 2Hz; and a moving square wave grating. Both stimuli were shown at 7 contrast levels (0%, 25%, 40%, 55%, 70%, 85% and 100%). The checkerboard was used to detect changes in visual evoked field amplitude. The grating allowed for gamma band oscillations to be measured. Blood flow was studied using a simultaneous BOLD/ASL fMRI sequence. 10 healthy volunteers were recruited to undergo two scan sessions: The first for MEG the second for fMRI recordings. The amplitude of the P100m component of transient VEFs (T-VEFs) was analysed in two ways – first by taking the amplitude from 0, the other by measured peak activation from the bottom of N70m troughs – and regressed against mean blood flow changes. Regression coefficients of 0.83 (±1.96, $p = 0.6$) for P100m from baseline against CBF changes, 0.27 (±0.05, $p < 0.001$) against BOLD, 1.42 (±1.64, $p = 0.3$) for P100m from N70m against CBF and 0.21 (±0.05, $p < 0.001$) against BOLD were found. Blood flow was then regressed against percentage changes in gamma power in the grating stimulus. A significant slope of -0.22 (±0.1, $p < 0.001$) and 0.08 (±0.005, $p < 0.001$) was found in percentage CBF change and percent BOLD signal change respectively. However, due to the large inter-subject variability, the power of this study is insufficient to empirically determine NVC. Nevertheless, it is a promising first step in establishing a viable protocol.

6-2 Introduction

The functional and structural integrity of the brain relies on a close balance between energy demands and substrate delivery from blood flow. The interaction between neurones, astrocytes and blood vessels endothelium to maintain sufficient cerebral blood flow is termed neurovascular coupling (NVC). NVC relies on cerebrovascular reactivity (CVR), which is the ability of vessels to dilate in response to a vasoactive stimulus. This has been shown to be impaired in several disease conditions from stroke and Alzheimer's to multiple sclerosis[34,147,170].

Evoked potentials are used to study electrophysiological characteristics of task-related events in the brain and provide an empirical measure of a large population of neural activity. The most commonly assessed is the visual evoked potential as it is both non-invasive and has been shown to have several characteristics (most notably amplitude and latency) which have been shown to alter in relation to intensity of the stimulus[171].

Visual evoked potentials (VEPs when measured using EEG, but when collected using MEG are instead referred to as visual evoked fields (VEFs)) are used clinically, particularly to assess function in CNS disorders such as multiple sclerosis and neuromyelitis optica[171–174]. VEFs are comprised of 3 main components: the first a negative deflection (N70), occurring between 65-80ms following stimulus onset; followed by a positive P100 wave at 95-120ms; and finally, a negative N140 at between 130-150ms after onset completes the VEP (fig. 6-1) [116,175].

The latency of the VEF is crucial to determining pathological states that may be occurring within the CNS. In degenerative diseases, such as multiple sclerosis (MS) the waves are differentially affected. P100 latency and amplitude is consistently affected in disease states reflecting demyelination and neuronal cell loss respectively and is therefore considered a hallmark of visual impairment. The N70 peak can also be altered and but can fail to appear at all, particularly at low stimulus intensities. It should be noted that the N70 is considered to be inconsistent in its presentation between subjects[174,176,177]. Thus, the P100 has been the main focus of evoked potential studies in both disease

states and healthy volunteers. The neural generators of VEFs are not clearly defined, generally, early phases i.e. N70 waves are thought to be generated in the primary visual cortex, with P100 waves being split between V1 and extrastriatal regions. N140 waves however, appear to be generated deeper in the parietal lobes[116,178]

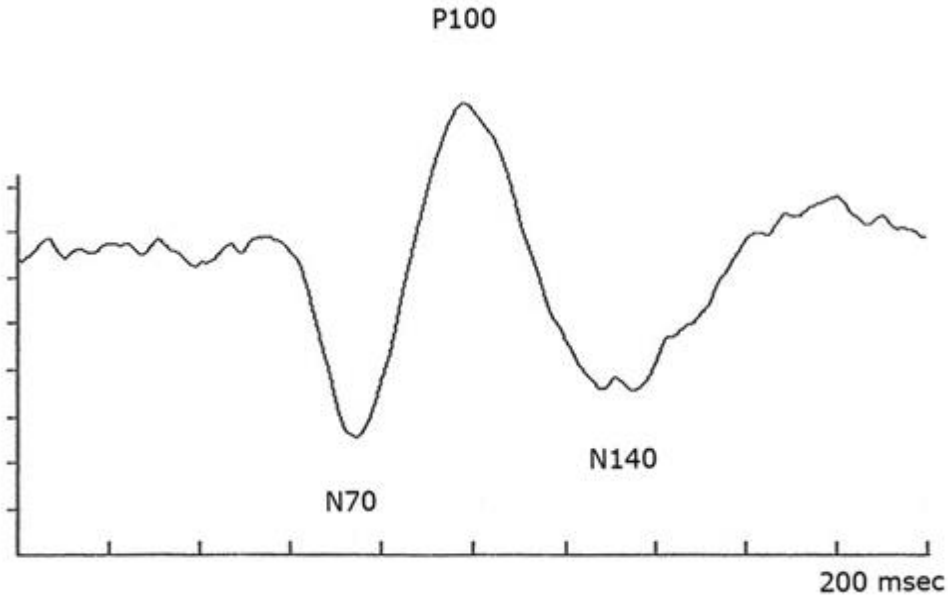

Figure 6-1 Representative trace of the three main components of the visual evoked potential. The first negative wave (N70) occurs between 65-80ms after stimulus onset. Followed by a positive deflection (P100) occurring between 95-110ms after onset. Finally, a negative deflection between 130-150ms (N140) finishes off the evoked potential.

In order to study the relationship between cerebral activity and the alterations in blood flow, there have been studies performed to look at glucose utilisation using positron emission tomography (PET)[171], blood flow changes using functional MRI (fMRI) to assess blood oxygenation level dependant (BOLD) and cerebral blood flow (CBF) measures as well as electroencephalographic (EEG) and more recently magnetoencephalographic (MEG) techniques for a more direct means of assessing neural activity[119,179,180].

Each of these techniques has its own advantages and shortcomings however, while PET allows for a direct measure of glucose and oxygen consumption. It is both expensive and involves exposure to ionising radiation which, due to ethical considerations can hinder any new study. Both EEG and MEG have very high temporal resolutions (on the order of milliseconds), but spatial resolution is poor due to this information being inferred via modelling of extra-cranial fields. In this respect, at least MEG confers a significant advantage over EEG, as magnetic fields are not hindered and distorted by the

scalp unlike electric currents. MEG also has the potential for more accurate source localisation, as modern MEG systems offer higher sensor densities compared to EEG systems, also increasing signal to noise ratios (SNR)[119,175]. Finally, fMRI has excellent spatial resolution (on the order of millimetres) but is limited by the haemodynamic response following neuronal activation meaning temporal resolution is limited to between 5 -10 seconds.

FMRI offers several markers of blood flow, the most common of which being Blood Oxygenation Level Dependent (BOLD) contrast which relies on the balance between oxy- and deoxy-haemoglobin as a contrast agent[105]. It therefore has a complicated relationship with haemodynamic and neurovascular responses and can be confounded by alterations in blood volume, neurovascular coupling and basal blood flows, which can modify task-related contrast. It is therefore difficult to use this as a quantitative measure of CBF [105,119]. Arterial Spin Labelling (ASL) involves labelling a bolus of blood coming up through the neck and assessing the magnetisation within a region of interest. While SNR is low it does enable a more accurate, quantitative approach to assessing cerebral perfusion[181,182]. By combining MEG and fMRI, it is possible to gain measures that are both high in spatial and temporal resolutions as well as quantifying blood flow and direct cerebral activities.

Previous work investigating the similarities between visual evoked potentials (VEPs) as measured by EEG and visual evoked fields (VEFs) measured via MEG has shown the two to be very comparable in terms of both observed waveforms and the latency of each peak[175,183,184]. This allows for a comparison of results seen in this study, using MEG, with previous work performed with EEG. There is, however, a difference in nomenclature as literature referring to VEFs append –m onto each wave to denote its magnetic field origins.

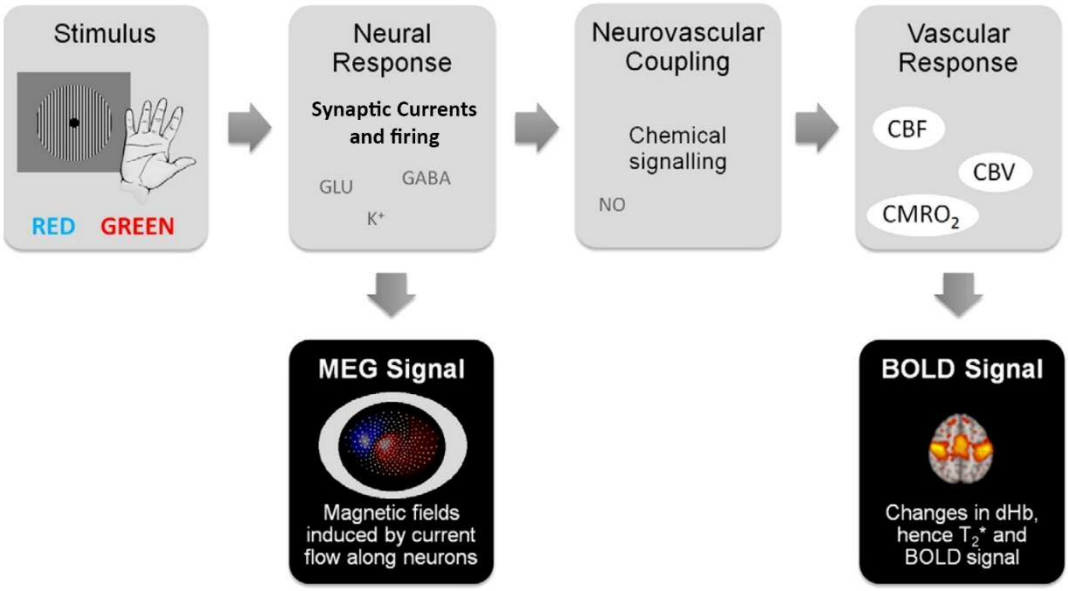

Figure 6-2 Schematic showing how MEG signals and fMRI are coupled. As a visual stimulus is presented there is a neural response causing the release of excitatory neurotransmitters (glutamate) resulting in further propagation of neural activity. This generates secondary chemical messengers (nitric oxide and K^+) acting on vascular smooth muscle and leading to increases in CBF and CBV. Image taken from [119]

Functional hyperaemia reflects vasodilation of arterioles in regions of neuronal activation and can be measured using BOLD or ASL. While it was originally assumed that coupling of neuronal activity and blood flow were due to local energy demands, work suggests that there is a direct signalling mechanism between neurons and smooth muscle within arterioles via astrocytes[86,89,170]. It is hypothesised that following synaptic firing secondary chemical messengers are released which causes a vascular response (fig. 6-2)[89,119]. Previous work using combined fMRI and EEG to model coupling between neural and haemodynamic responses, has demonstrated that a multi-modal approach to quantify neural and haemodynamic responses to a stimulus can be used gain a measure of neurovascular coupling[180].

In this present study, I aim to combine fMRI and MEG-based methods, to investigate visual evoked fields generated from a visual stimulus of increasing contrast in MEG, and regress this against blood flow alterations using a dual echo MRI sequence allowing simultaneous acquisition of ASL and BOLD weighted images. I hypothesise that as contrast increases so does the amplitude of VEFs and fMRI response within the visual cortex allowing us to develop an empirical measure of neurovascular coupling.

6-3 Methods

6-3-1 Subjects

10 healthy (M_{age} 23.9±2.16 (±SEM) years and 5 males, 5 females respectively) volunteers were recruited. Informed consent was taken for all participants under ethical approval from the Cardiff University School of Psychology Ethics Committee. All subjects apart from 4 required corrective lenses for daily use and were provided with MRI-safe spectacles throughout the experiment.

Subjects were then scanned once in MEG and once in MRI while a reversing checkerboard and moving grating were presented at 6 contrast levels.

6-3-2 Visual paradigm

There were two stimuli presented: the first was a reversing checkerboard, the second was a moving square wave grating. I was interested in two types of MEG recording from this study, the first was the presentation of VEFs and the other was changes in gamma power. These two stimuli had previously been used by other groups in CUBRIC to produce the same responses in MEG and are therefore excellent for modification and use in this pilot study[121,122,185–187]. Both were displayed at 7 contrast levels during both a MEG and MRI scan. Stimuli were generated in Matlab® at 6 (0%, 25%, 40%, 55%, 70%, 85% and 100%) Michelson contrast levels. Checks were displayed centrally at 0.5 cycles per degree (cpd) with a reversal rate of 2Hz to preserve VEFs. The grating was displayed at 3cpd with a movement of 1 cycle per second from left to right. The entire stimulating field was 16° of visual angle. Subjects sat 80cm from the screen in MEG and 60cm in MRI, and the visual angle was matched in both scanners. Contrasts were displayed pseudorandomly for each participant, but contrast order was maintained between scan sessions for each subject. These paradigms were chosen to elicit both a measurable VEP response in MEG, evoked gamma oscillations, as well as producing a stimulus-induced increase in CBF[122,186,188].

Each checkerboard contrast was displayed for a total time of 2 minutes, split into 4 blocks of 30 seconds. A rest period of a 0% contrast checkerboard was displayed for a total of 4 minutes, split into

8 30 second blocks. Each contrast block was displayed in a pseudo-random order. The grating followed the same display pattern as the checkerboard. However, each contrast block was not shown continuously, instead a 1 second on/1 second off design was employed during each 30 second block. Stimulus types were also presented pseudorandomly for each participant, but order was maintained between MEG and fMRI scans. Each stimulus lasted 16 minutes. Stimuli were displayed on a Sanyo XP41 LCD back-projection system in MEG and a Canon Xeed SX60 projector (1024x786 resolution 60Hz refresh rate) in MRI.

6-3-3 MRI

MRI data were acquired on a General Electric HDx scanner with eight channel receive only head RF coil (Medical Devices). Simultaneous ASL and BOLD imaging data was collected for each subject using a PASL proximal inversion and control for off resonance effects (PICORE). Quantitative imaging of perfusion using a single subtraction (PICORE QUIPSS II)[189] imaging sequence with a dual-echo gradient echo (GRE) readout and spiral k-space acquisition (TE1 = 3ms, TE2 = 29ms, TR = 2.2s, flip angle = 90degrees,FOV=22cm,matrix=64x64, 12 slices of 7 mm thickness with an inter-slice gap of 1 mm acquired in ascending order, voxel size 3.4mmx3.4mmx7mm, TI1 = 700ms, TI2 = 1600ms for the most proximal slice and was incremented by 54.6ms for subsequent slices, tag thickness = 20 cm, adiabatic hyperbolic secant inversion pulse, 10 mm gap between labelling slab and bottom slice, 10 cm QUIPSS II saturation band thickness). This resulted in the acquisition of 438 volumes (219 tag control pairs). A separate single shot (M_0) scan was acquired (TR=infinity) with the same parameters as the functional run to measure the equilibrium brain tissue magnetisation for purposes of quantifying CBF. A minimum contrast image was also acquired to correct for coil sensitivity with the same acquisition parameters as the ASL run except for TE =11ms, TR = 2 s, and 8 interleaves. High resolution anatomical (1mm voxel size) FSPGR T1-weighted scans were acquired for use during registration.

6-3-4 MEG

Whole head MEG recordings were acquired using a CTF-Omega 275-channel radial gradiometer system sampled at 1200Hz. An additional 29 reference channels were recorded for noise cancellation purposes and the primary sensors were analysed as synthetic third-order gradiometers[185,190]. Four of the 275 channels were switched off due to excessive sensor noise. The location of three fiduciary markers (nasion, left and right preauricular) was monitored continuously through the MEG acquisition at a frequency of 10 Hz. For each checkerboard reversal, a TTL pulse was sent to the MEG system, data was acquired continuously and epoched offline in a window that extended 40ms before and 200ms after the TTL pulse. Trials were manually excluded based on visibly identifiable artefacts. Eye movements were monitored throughout data acquisition to ensure subjects were attending to the screen and not falling asleep.

6-3-5 Analysis

6-3-5-1 MEG

Analysis of event related fields (ERFs) in sensor space was conducted using the FieldTrip toolbox for Matlab[191]. Time-locked analysis was performed on epoched raw data following baseline correction -40–200ms around each reversal.

Bandpass filtering was applied using an IIR Butterworth filter between 1-100Hz and limited from -40-200ms following reversal to allow a full range of evoked potentials to be analysed. A SAM beamformer was used to generate pseudo-T statistic maps comparing rest blocks of 0% contrast to active contrast blocks. This revealed an area of increased power in the primary visual cortex, and virtual sensors were generated using SAM beamformer coefficients, returning the time-series from peak locations.The location of the highest pseudo-T statistic within the visual cortex was used as the location for a 'virtual sensor'[121].

Following extraction evoked fields were baselined, a further IIR Butterworth filter was applied between 1-40Hz and demeaned. Filters have been applied in this way to enable source localisation to

be performed. Applying an initial filter of 1-40Hz rather than 1-100Hz resulted in a poor source solution during SAM processing. Therefore two filters have been applied in this way to mitigate this problem. Peak amplitudes were recorded for each subject at each contrast, as well as the average trace of all participants across contrasts.

There is some conflict in the literature as to how and which peak of the evoked potential should be measured. Several peaks were recorded as part of the analysis: N70m, P100m, N70m-P100m peak difference, P100m latency, N140m and P100m-N140m peak difference. All peak amplitudes were calculated using matlab peak maxima functions in time windows expected for each peak (65-80ms, 95-110ms and 130-150ms after checkerboard reversal for N70, P100 and N140 peaks respectively). This allowed for the most appropriate part to be regressed against any alterations in blood flow.

Gamma power was determined in a similar manner to calculating VEF amplitude; each dataset was epoched around each marker (-1s – 1s), the 1 second of 'off' period (-1s – 0s) was used as a baseline to compare to active periods (0 – 1s). Each epoch was then bandpass filtered using an IIR Butterworth filter to between 30-80Hz. A SAM beamformer was used to create a pseudo-T statistic map comparing baseline to active contrasts. This revealed an area of increased power in the primary visual cortex, and virtual sensors were generated using SAM beamformer coefficients, returning the time-series from peak locations. Time frequency analysis was performed using the Hilbert transform from 1-100Hz in 0.5Hz steps and represented as a percentage change in gamma power from baseline, from this peak evoked gamma power change values from baseline were obtained[122]. There was a broad overlap of increased signal in the visual cortex between VEF-optimised statistic maps, and gamma power-optimised maps. However, the peak pseudo-T statistic was not the same location for both datasets, therefore different locations for the virtual sensor were used for each subject and stimulus. Peak evoked gamma power was extracted using in house matlab® scripts.

6-3-5-2 MRI

Preprocessing of functional images was performed by first brain extracting all images using FSL-BET[155], motion correction was performed using MCFLIRT and highpass filtering of 120s was applied for BOLD and 70s for perfusion-weighted images and smoothed using a gaussian 5mm kernel. Functional images were registered first to subject's high resolution T1 structural scan, limited to 6 degrees of freedom, then to Montreal Neurological Institute (MNI) 152 space with 12 degrees of freedom. Both steps were linear warps[154]. Physiological noise correction was carried out prior to data processing, a modified RETROICOR[192], where 1st and 2nd harmonics of cardiac and respiratory cycles (and the interaction term) were calculated in addition to variance related to heart rate (HR)[193] using a general linear model framework and regressed from the data.

As two echo times were used to generate perfusion and BOLD weighted images the two datasets were processed slightly differently. For BOLD weighted images, interpolated surround averaging of the tag and control images was performed, the average of each timepoint from the mean of its two neighbours, as described previously[194] to remove the tag-control signal from the dataset.

Resulting images were then fed into FSL-FEAT[153] where a GLM was used to regress the hemodynamic responses for each contrast. Regressors were made from timings of each visual contrast convolved with a HRF. For perfusion-weighted data a sawtooth design matching the TR of the function MRI sequence was applied to model alterations in intensity between tag-control slices, an interaction between this and the visual contrast GLM was used to model ASL data (fig. 6-3).

Masks were generated by multiplying an anatomical occipital lobe mask provided by FSL, with individual thresholded z-statistic images (z=2.3) of the maximal contrast responses. These were generated from FEAT report for each subject. Functional masks were created for each subject and used as an ROI when assessing responses from each visual contrast. These masks were used to define ROIs with which to calculate percentage changes in both BOLD and CBF data

For BOLD data percentage changes were calculated using FEATQuery from the FSL toolbox. For perfusion-weighted data CBF changes were exctracted using the GLM model defined in fig. 6-3 and represented the absolute CBF of the ROI during stimulation. These values were divded by baseline CBF to obtain fractional CBF changes (percent CBF change) from baseline.

6-3-5-3 Statistical Analysis

One-way ANOVA was performed on VEF amplitudes, percentage change in gamma power, percent BOLD signal change and percent CBF change to determine the alterations in the strength of responses with stimulus intensity (contrast). Linear regression was then performed of individual blood flow responses against individual neuronal measures for each type of stimulus (checkerboard or grating). Regression was performed for each subject's responses individually, and then averaged for each stimulation type to give a mean regression coefficient. All results are mean values ± SEM unless otherwise stated.

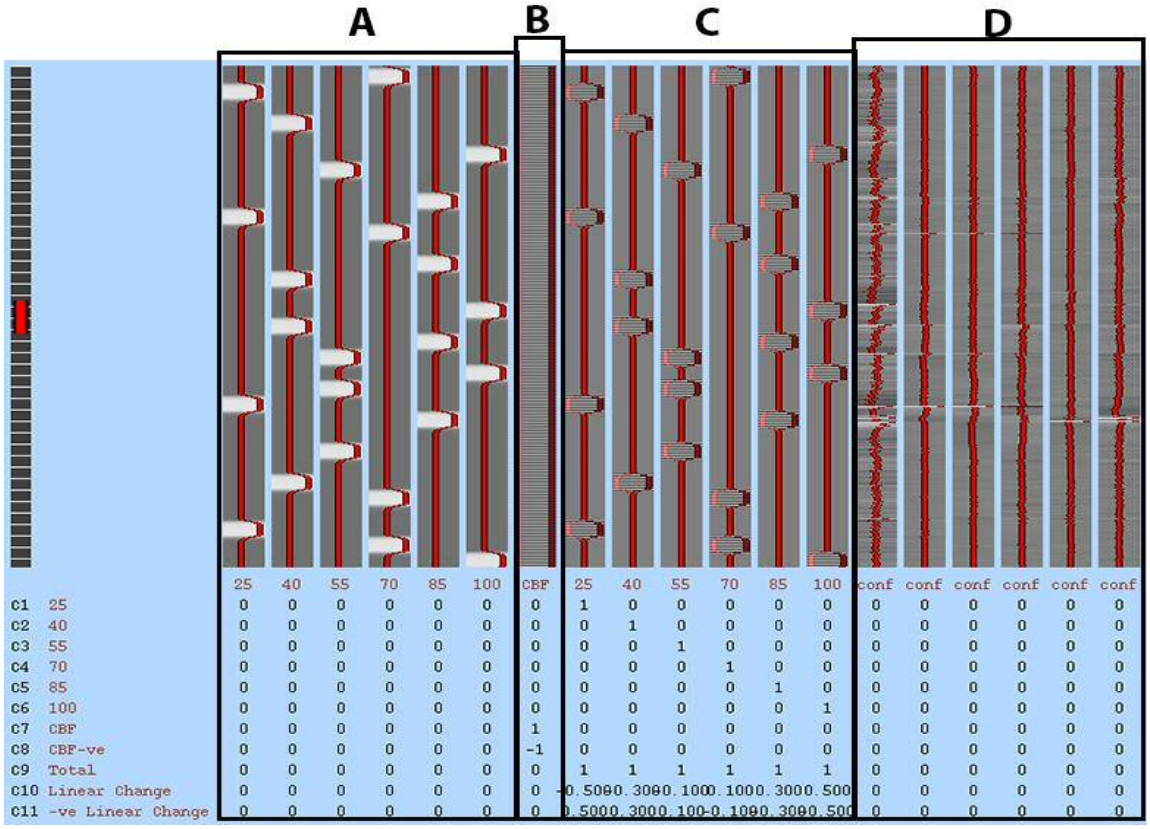

Figure 6-3 Representative design matrix for analysis of perfusion weighted images. Box A represents contrast order. Box B shows the saw tooth design used to model tag/control pairs. Box C is the interaction between contrast and tag/control labels. Finally, box D shows the motion parameters added to the model, these were obtained from FSL MCFLIRT.

6-4 Results

One-way ANOVA was used to determine alterations in the strength of response to each visual stimulus and are summarised in table 6-1.

Out of the peaks measured from the evoked potentials here I focused on the P100m as it is the one most commonly used to assess CNS damage and optical integrity[172,175]. There is some conflict in the literature as to how to peak amplitudes. In P100m's case this is whether to measure from 0 or to measure from the bottom of the N70(m) wave. For the checkerboard stimulus, P100m VEF amplitudes showed a main effect of contrast ($F = 3.3$ $p = 0.01$, $F = 2.9$ $p = 0.02$) when measured from baseline and from peak N70m respectively. BOLD signal increases and percent CBF increases showed no main effect or significant differences between contrasts ($F = 1.3$ $p = 0.2$, $F = 0.9$ $p = 0.5$ respectively).

Using the grating stimulus, no main effect was noted between each contrast response for gamma power ($F = 0.65$ $p = 0.6$). Figure 6-4 shows a single representative subject's spectograms used to calculate evoked gamma power at each contrast (25% - 100%, A-F respectively). Figure 6-5 shows averaged time/frequency responses across all subjects. In addition to this there was no significant alterations in CBF responses across contrasts ($F = 0.45$ $p = 0.8$). There was however, a significant difference in BOLD signal responses ($F = 3.3$ $p = 0.01$).

Mean Response ± SEM		Contrast						ANOVA results
		25	40	55	70	85	100	P value
Checkerboard	Percent CBF change	31.9±1.3	34.5±2	33.2±2.8	32.2±1.8	39.5±3	35.4±2.3	0.2
	Percent BOLD signal change	1.9±0.2	2.0±0.1	2.3±0.2	2.3±0.18	2.3±0.18	2.2±0.21	0.5
	VEP amplitude from 0	1.3±0.36	1.9±0.34	2.5±0.28	2.5±0.2	2.6±0.14	2.5±0.18	0.01
	VEP amplitude from N70	2.1±0.4	2.5±0.4	3.2±0.32	3.3±0.26	3.5±0.22	3.3±0.2	0.02
Grating	Percent CBF change	15.0±4.3	24.1±10	15.3±6.5	20.4±6.6	11.9±3.9	14.7±4.1	0.8
	Percent BOLD signal change	0.1±0.15	2.4±0.64	3.0±1	3.6±1.2	3.7±1.1	4.1±1.3	0.01
	Percent gamma power change	33.2±5.9	43.8±9.3	52.7±11.2	54.2±9.2	59.6±12.1	57.9±10.3	0.6

Table 6-1 Summary of mean neuronal and blood flow responses to contrast in each of the stimuli presented. For the checkerboard, no significant differences in blood flow responses were noted between contrasts ($p = 0.2$ and 0.5 for percent CBF change and percent BOLD signal change from baseline respectively). VEP amplitude was sound to be significantly different between contrasts when measured both from 0 and from the trough of N70 ($p = 0.01$ and $p < 0.05$ respectively). For the grating however, no significant difference in response was seen in percent CBF change or percent gamma power change from baseline ($p = 0.8$ and $p = 0.6$ respectively). Blood flow responses seen using BOLD did show a significant difference between contrasts ($p < 0.05$). All values are mean ± SEM.

Figure 6-6 shows the variability of VEF amplitude between contrasts, averaged VEFs (green line) along with standard error (grey shading) across subjects for each contrast. At low contrasts (figure 6-6A+B) the N70m wave is absent with P100m waves lacking sharp, defined peaks. As contrast increases there is a sharpening of the P100m peak along with N70m wave becoming more pronounced (fig. 6-6 C-F). Inter-subject variability also appears markedly higher at lower contrasts.

Figure 6-7 shows a visualisation of each response measured for each contrast shown in the checkerboard (A+B) and grating (C+D), lines shown here are mean slopes following averaging of regression coefficients for each subject. Regression of changes in blood flow against P100m amplitudes returned slopes of 0.83 (±1.96, $p=0.6$) for P100m from 0 against percent CBF change and 0.27 (±0.05, $p < 0.001$) against BOLD. A slope of 1.42 (±1.64, $p=0.3$) for P100m from N70m against CBF and 0.21 (±0.05, $p < 0.001$) against BOLD (figure 6-8A). Regression of gamma power against blood flow measures in the grating revealed a significant coupling between neuronal and blood flow measures. A significant slope of -0.22 (±0.1, $p < 0.001$) for gamma power regressed against percent CBF change. Percent change in BOLD weighted signal also returned a significant slope of 0.08 (±0.005, $p < 0.001$) (figure 6-8B).

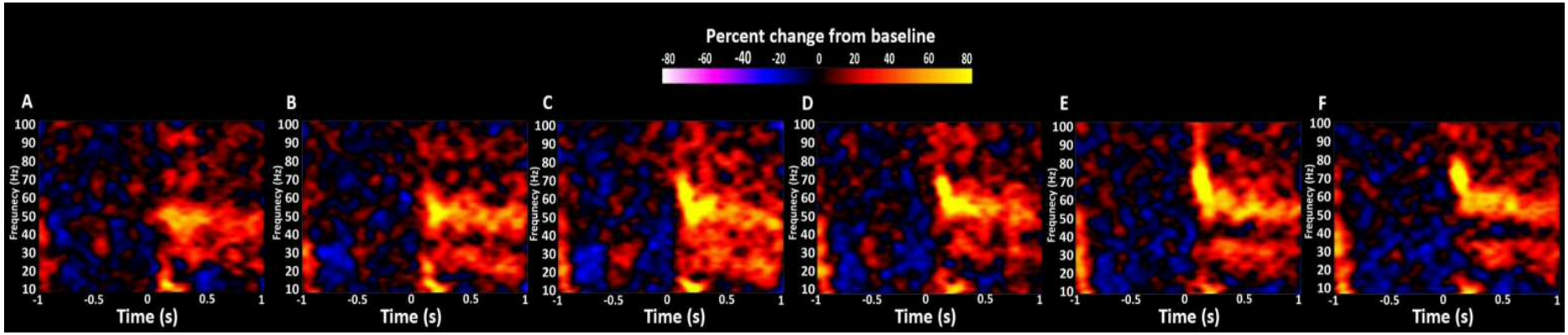

Figure 6-4 Individual time/frequency responses from the moving grating stimulus. Each contrast is represented in a separate image (A – 25%, B – 40%, C – 55%, D – 70%, E – 85%, F – 100%). As contrast increases, there is a larger increase in both broadband gamma power, and the frequency range of initial onset (30-80Hz, 0-300ms). This is then followed by a longer, sustained increase in gamma power around the 50Hz frequency mark. As contrast increases, the transient gamma power also increases.

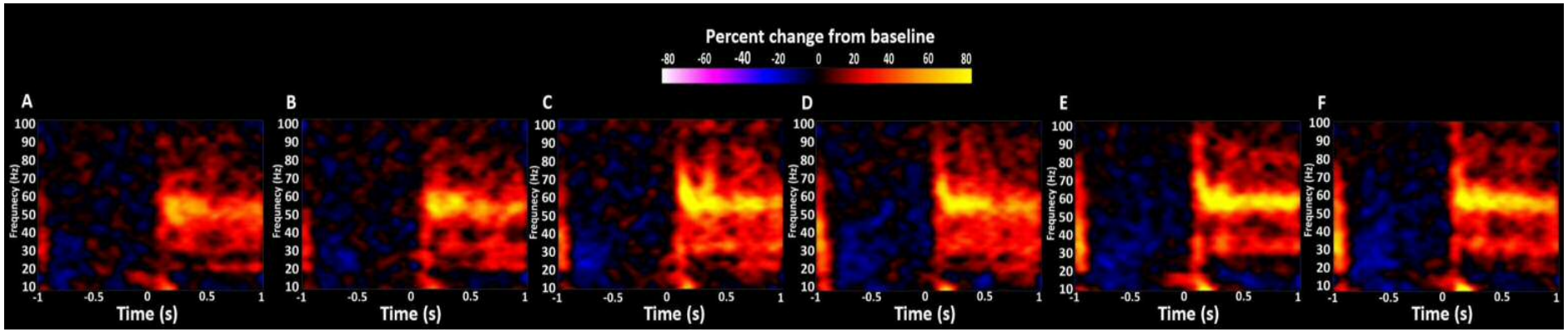

Figure 6-5 Subject averaged time/frequency responses from the moving grating stimulus. Similar to figure 3, onset of the stimulus resulted in transient increases in broadband gamma power followed by a narrower sustained gamma band response. As contrast increased so did the intensity of the response, each image represents a contrast (A – 25%, B – 40%, C – 55%, D – 70%, E – 85%, F – 100%).

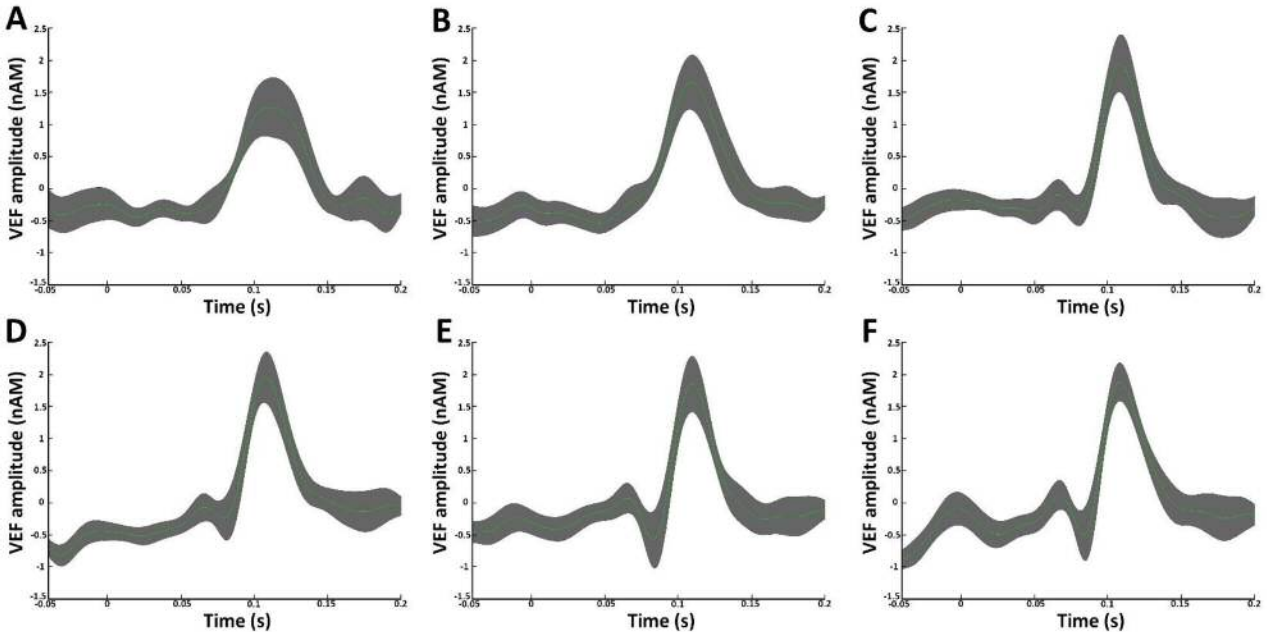

Figure 6-6 Subject averaged evoked potentials from the checkerboard stimulus (green line) with standard error shown (grey shading) for 25% (A), 40% (B), 55% (C), 70% (D), 85% (E) and 100% (F) contrasts. N70m peaks are highly variable and do not appear to show easily at lower contrasts (25% and 40%), but progressively become more prominent at higher contrasts. Similarly, P100m waves appear blunted at lower contrasts but amplitude increases with stimulus intensity, along with a reduction in standard error and a sharpening of the peak.

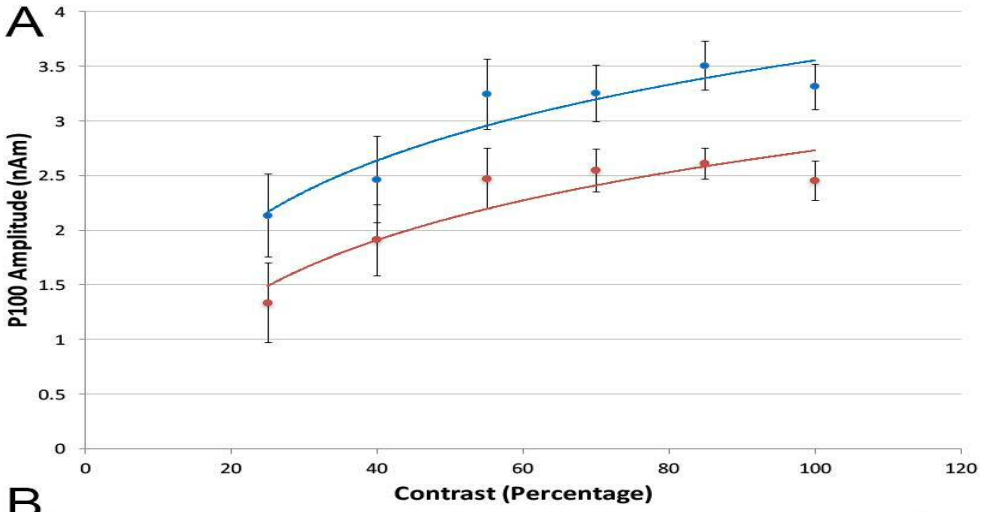
A
P100 Amplitude (nAm)
Contrast (Percentage)

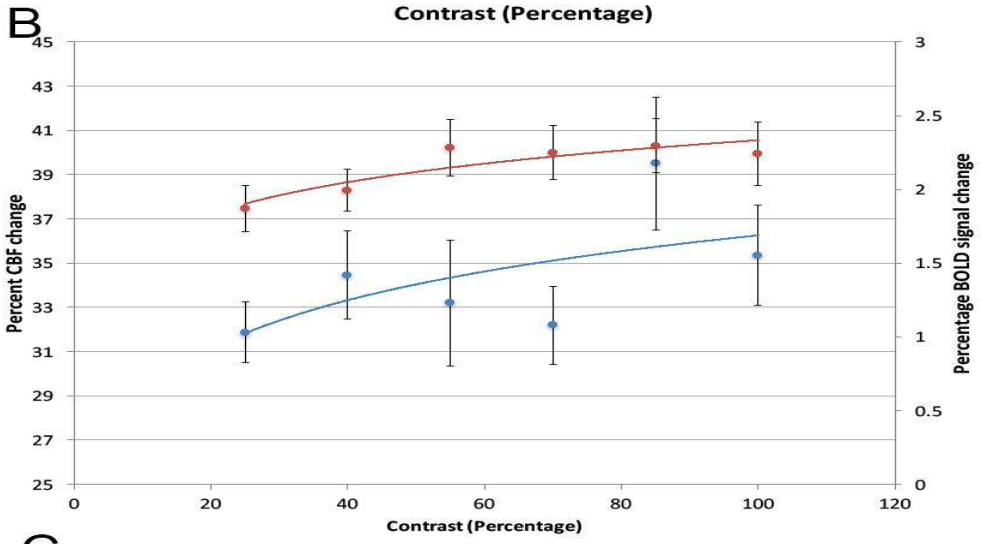
B
Percent CBF change
Percentage BOLD signal change
Contrast (Percentage)

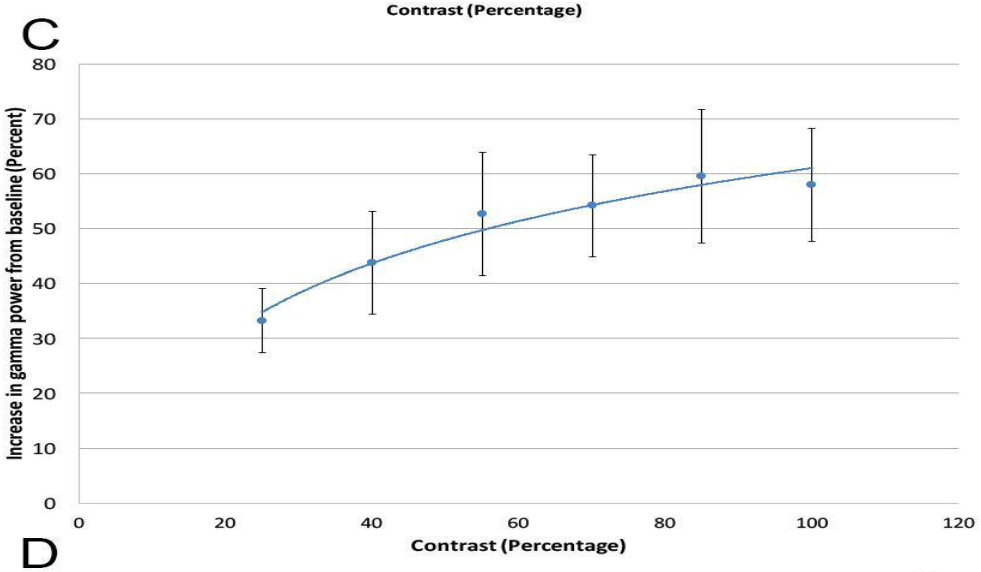
C
Increase in gamma power from baseline (Percent)
Contrast (Percentage)

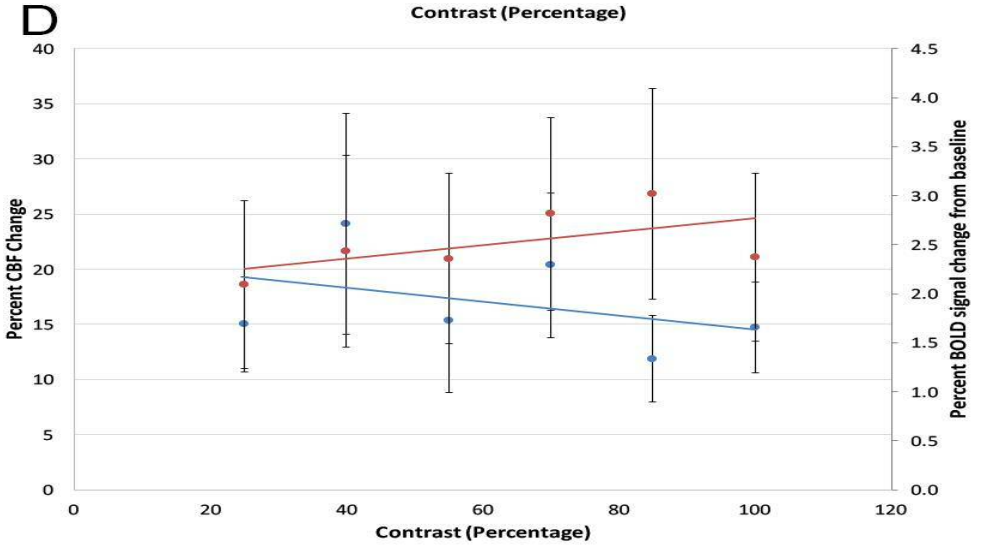
D
Percent CBF Change
Percent BOLD signal change from baseline
Contrast (Percentage)

Figure 6-7 Subject averaged responses in the checkerboard (A+B) and grating (C+D). A) Shows VEF amplitude measured from 0 (red) and from the base of N70m to peak P100m (blue). B) Displays blood flow responses BOLD (red) and percent CBF change (blue). C) Illustrates percent gamma power change as measured from the initial evoked gamma power spike. D) Shows the associated BOLD signal increases (red) and percent CBF change (blue) with each grating contrast. In A-C as contrast increases in the stimulus average reponse strength also increases in a non-linear trend. In D – the grating stimulus – very little change in blood flow reponse is noted. Lines shown are mean regression slopes following averaging of indivudal regression coefficients. Error bars show the standard error about the mean for each averaged response at each contrast.

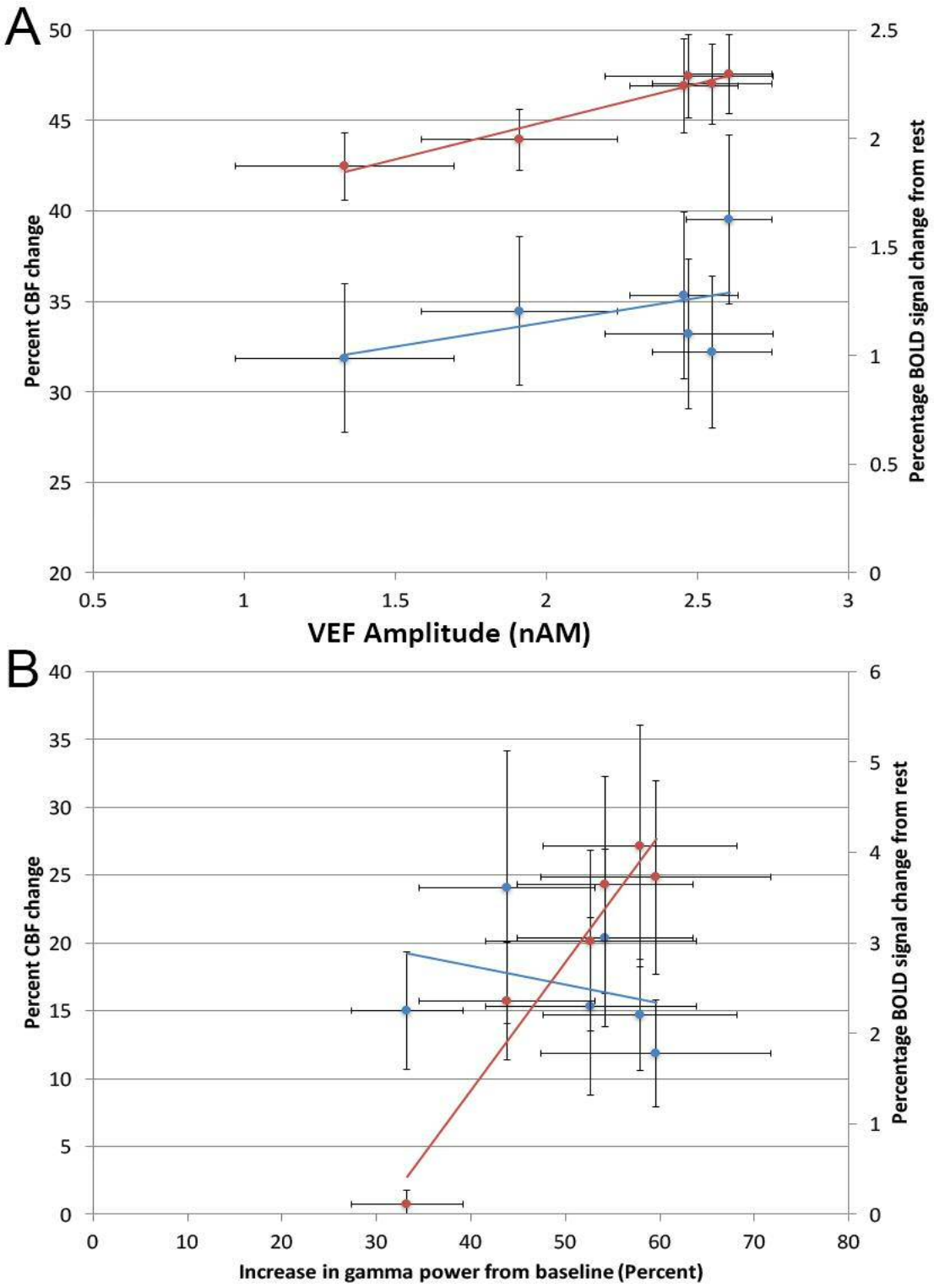

Figure 6-8 A) Regression charts of average subjects' changes in P100m amplitude from 0 against changes in BOLD (red) and percent CBF change (blue) with contrast. Regression coefficients for VEF amplitude vs CBF was 0.83 (±1.96, p = 0.6) and 0.27 (±0.05, p < 0.001) for BOLD. When P100m amplitude was measured from N70m regression coefficients were 1.42 (±1.64, p = 0.3) when compared against CBF and 0.21 (±0.05, p <0.001) against BOLD signal changes (data not shown). B) Subject averaged BOLD (red) and percent change in CBF (blue) regressed against percentage change in gamma power. A significant slope of -0.22(±0.1, p <0.001) is seen in the CBF-based NVC measure. BOLD-weighted signal-based NVC returned a significant linear regression of 0.08 (±0.005 p<0.001).

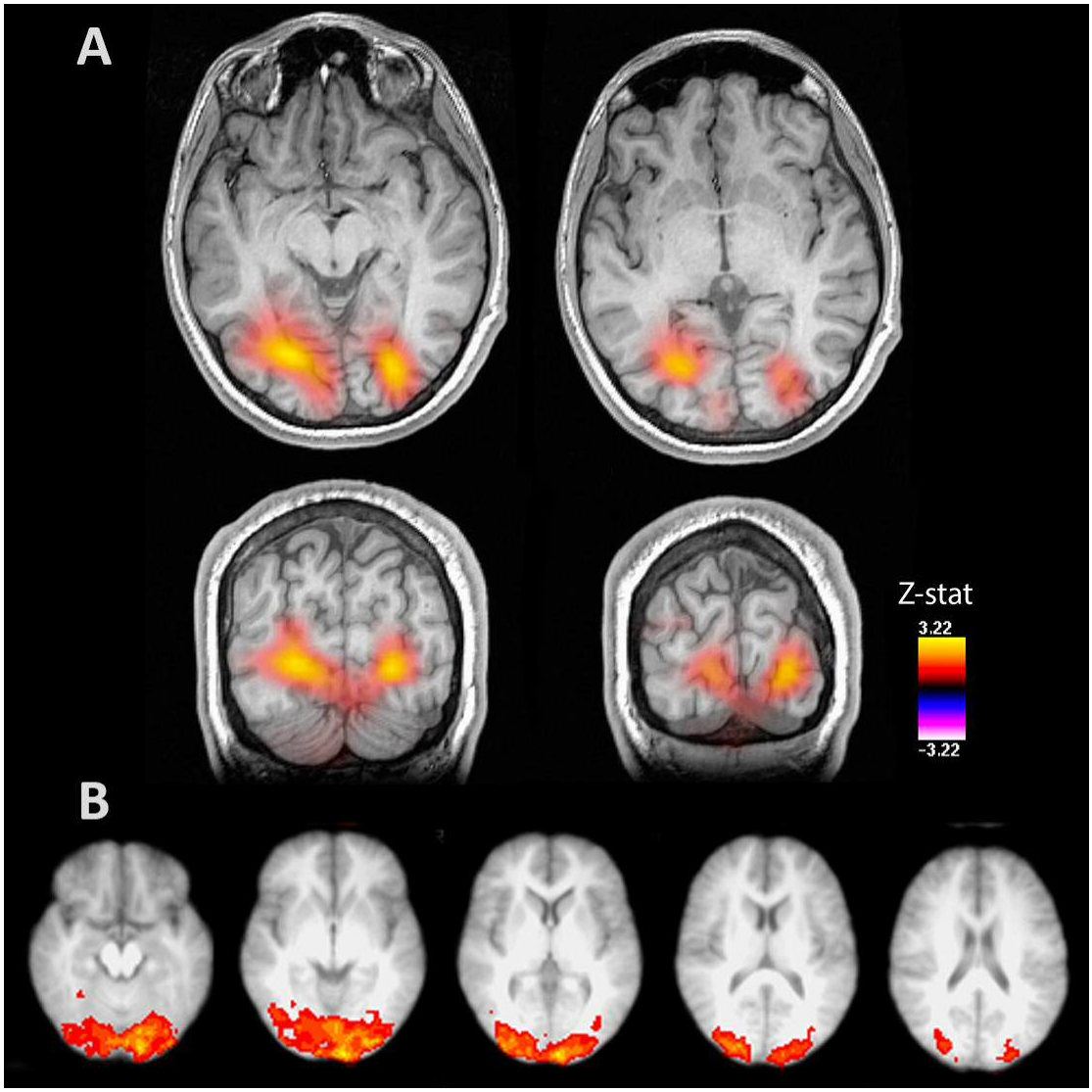

Figure 6-9 Image showing source localisation solution of visual evoked fields in MEG (A) from a single representative subject following a 100% contrast checkerboard stimulus. B) shows the same subject's BOLD response following a 100% contrast checkerboard stimulus in an fMRI setting. Spatial resolution in MEG is known for not being as accurate as fMRI, however, similar response locations can be seen indicating a strong likelihood of the neural generators of the MEG signal being responsible for the BOLD response see in fMRI.

6-5 Discussion

In this study I compared two methods of measuring NVC using different stimuli – a reversing checkerboard and a moving grating. Peak P100m VEF amplitudes were recorded in the checkerboard, whilst gamma power was measured for the grating. These were both obtained from MEG recordings, whilst BOLD/ASL-fMRI responses were collected for both stimuli. The aim was to regress neuronal measures against blood flow markers in an attempt to define empirically NVC.

Only VEF amplitude reliably increased with stimulus strength. Percent BOLD signal change measured in the grating stimulus also showed a significant increase in response to contrast levels. All other measures in each stimulus only exhibited a trending increase in response strength.

N70m waves were difficult to detect at low contrasts. At higher contrasts (50% and above), however, all three peaks (N70m, P100m and N140m) were clearly visible. I focussed on P100m as this is considered to be the most clinically relevant wave and the main focus of the EEG studies I am comparing to[172,188]. Source localisation of P100m and gamma oscillatory activity consistently revealed one peak location of activity around the calcarine sulcus in 8 out of 10 subjects in agreement with the accepted location of generators of P100m waves[116]. Locations of peak activation for P100m waves and gamma oscillations were slightly different from each other. This could possibly be due to two different neural generators of these measures, or could be due to slightly different source reconstruction in each case, possibly owing to the different parameters of the visual stimulus[188]. Group fMRI data demonstrated increased BOLD/perfusion-weighted signal in locations similar to that seen in MEG.

Regression between VEF amplitudes and fMRI responses only returned a significant dependency when regressing P100m amplitudes against BOLD signal change (fig. 6-8). Measuring NVC using percent CBF change derived from ASL data revealed no significant

relationship. This is likely due to the low SNR of this type of measurement, in addition the number of participants recruited not being high enough to give the measurement enough statistical power. Regressing blood flow measures against percent gamma power change in the grating stimulus yielded a significant coupling with both BOLD and ASL-derived measurements. Again due to the low SNR seen in ASL measures, the coupling here appeared negative, an unexpected result, but as there was no significant difference between percent CBF change at each contrast level, it is possible for this negative appearing coupling to be a false positive.

One reason for this could be the compromise being reached between MEG and fMRI measures. To gain reliable transient VEFs (T-VEFs) a reversal rate of 1-2Hz is typically employed. In fMRI it is more common to use a higher frequency of 8Hz to confer the largest possible BOLD/CBF response[115,116,171,175,183]. Using a high frequency of reversal would not allow full separation of VEFs in MEG but a low reversal frequency would not gain the necessary SNR in fMRI for us to measure a change in blood flow in a short period of time. Here I compensated and used a reversal of 2Hz which allows for measurement of T-VEFs and to gain a reasonable SNR in fMRI within a smaller timeframe. However, there is some evidence to suggest that while an increase in reversal rate up to 8Hz causes a much larger CBF response in fMRI; this is met with a reduction in $CMRO_2$[171]. In addition to this, the contrast range used in this study was limited, and focussed towards the top end of the scale, therefore the scope of the dynamic range available for the fMRI response would be limited[171,195].

The grating stimulus used here did not provide the significant alterations in blood flow that was expected. Due to the 1 second on/off design of the stimulus it is possible this reduced the rises in blood flow for each contrast. Using this stimulus however, did provide a possibility of using gamma power in creating a measure of neurovascular coupling. Gamma power has been shown to increase with stimulus intensity[128], and has been corroborated here.

Due to the lack of clear difference in blood flow responses, the low SNR of ASL could be one problem here, and as BOLD signal relies on a balance between oxygenated and deoxygenated haemoglobin it is possible to get an increase in CBF without measuring a difference in BOLD signal changes i.e. the 'ceiling effect'[105,171]. However, another problem could be the limited range of contrasts selected for the stimulus. Other studies, using a wider range of contrasts have demonstrated robust alterations in blood flow[171], implying the high contrasts used here do not fully capture subtler changes in flow. In refining this measure of NVC it would be advisable to utilise a wider range of visual contrasts, spaced further apart than what was used here.

Figure 6-7 shows a non-linear relationship of both blood flow and neuronal measures with respect to contrast. If a wider range of contrasts were to be used when refining the NVC protocol, using a power law function to characterise the relationship between responses and stimulus intensity as well as neuronal and blood flow coupling is likely to characterise the relationship better compared to using a standard linear regression model. The grating stimulus used here yielded poor results with respect to blood flow measurements. This is likely due to a combination of the higher-end contrasts used, as well as the 1s on/off design yielding low blood flow responses and high noise within the data. Indeed, as the overall aim of this thesis is to use a NVC protocol in MS patients, it would be best to have as short a scan time as possible. Two 16-minute MEG scans, followed by two 16-minute fMRI scans, as well as additional structural imaging and baseline blood flow measurements could prove too long for patients. As patients fatigue, motion artefacts can contaminate any data collected, as well as the risk of patients falling asleep during scanning. Therefore, for these reasons when refining this protocol, the grating paradigm should be withdrawn, and instead focus on the checkerboard stimulus with a wider contrast range. It is possible that evoked gamma power can be extracted from the responses gathered from the checkerboard stimulus instead. Given the high volume of trials that are collected with this stimulus, a good signal should be available

for analysis. If the PING model is indeed accurate in explaining the source of gamma oscillations, using gamma power would be a valuable tool for assessing the health of neurovascular units and the efficiency of communication between neurons and interneurons/astrocytes and the underlying vasculature. As both gamma power and VEF amplitude have previously been shown to be stable over time, an assessment of their repeatability should be undertaken to ensure an empirical measure of NVC will be similarly stable[115,185].

Chapter 7: Assessing the repeatability of neurovascular coupling: a combined MEG/fMRI approach

7-1 Abstract

This study aims to define and compare empirical measures of neurovascular coupling defined from MEG and fMRI data and assess their respective stabilities. 15 healthy volunteers were recruited to undergo 4 scan sessions consisting of two pairs of MEG and MRI. The two MEG sessions were performed M_{days} 10.6±2.6 apart, MRI sessions were M_{days} 12.5±2.7 apart. A reversing square wave checkerboard was used at 2Hz and shown at 5 contrast levels (6.25%, 12.5%, 25%, 50% and 100%) to detect changes in P100m visual evoked fields, gamma power and blood flow alterations, measured via MEG and BOLD/ASL fMRI respectively. Transient P100mVEF amplitudes were measured, along with increases in gamma power from baseline in MEG. These measures were then regressed against alterations in BOLD- and perfusion-weighted signal changes in MR, the regression coefficients defining an empirical measure of neurovascular coupling (NVC). Intra-class correlation coefficients (ICC (3,1)) was used to establish repeatability of individual neuronal and haemodynamic measures and the empirically defined NVC. P100m amplitudes were found to be unstable over time, displaying an ICC around 0. BOLD, gamma power, and perfusion weighted measures however, were more stable with significant ICC values of 0.67, 0.9 and 0.5 respectively. The regression coefficients across sessions revealed an unstable NVC measure was created using P100m amplitudes as part of a NVC measure. Instead, gamma power increases correlated more strongly with MR-based CBF measures and were found to be stable across time making CBF-gamma power a strong candidate for empirical assessment of NVC.

7-2 Introduction

The functional and structural integrity of the brain relies on a close balance between energy demands and substrate delivery from blood flow. The complex interaction between neurons, arterioles and supporting cell types helps to maintain cerebral blood flow, and is termed neurovascular coupling (NVC). NVC relies on preserved cerebrovascular reactivity (CVR), which is the ability of vessels to dilate in response to a vasoactive stimulus, and has been shown to be impaired in several disease conditions from stroke and Alzheimer's to multiple sclerosis[34,147,170]. Therefore, by defining NVC, it would be possible to establish the extent to which alterations, particularly in blood flow and substrate delivery to the brain could be contributing to the pathology of a disease state, as well as having a use as a target marker for damage when establishing new lines of treatment.

In order to study NVC a measure of both neuronal activity and associated changes in blood flow is required. Electroencephalography (EEG) and magnetoencephalography (MEG) are widely used investigate neuronal activity through evoked potentials, or oscillatory power. Similarly, functional magnetic resonance imaging (fMRI) enables researchers to study blood flow within the brain and alterations thought to correspond to changes in neuronal activation. There are several ways this can be achieved, however, these are typically variations centred around blood oxygenation level dependent (BOLD) weighted signal, or arterial spin labelling (ASL) techniques. As all of these techniques are well established throughout the research community it would desirable to assess these methods when establishing a measure of NVC.

Evoked potentials are used to study task-related events in the brain. One of the most commonly assessed is the visual evoked potential (VEP) as it is can be measured non-invasively, and has been shown to have several characteristics, (most notably amplitude and latency) which can be altered in relation to intensity of the stimulus [171].

Visual evoked potentials (VEPs) are used clinically, to assess function in CNS disorders such as multiple sclerosis and neuromyelitis optica [171–174]. VEPs are comprised of 3 main components; the first a negative deflection (N70) occurring between 65-80ms following stimulus onset, followed by a positive P100 wave at 95-120ms and finally a negative N140 at between 130-150ms after onset completes the VEP [116,175].

It should be noted that the N70 is considered to be inconsistent in its presentation between subjects [174,176,177]. Thus the P100 has been the main focus of evoked potential studies in disease states and healthy volunteers.

Oscillations in brain activity, particularly the gamma band have been demonstrated by several groups to be modulated during task-related events. [127]. However, the gamma band has been of particular interest in this study due to its ability to be modified by a range of stimulus effects – such a spatial frequency, contrast and orientation – when subjects are presented with a visual task [118]. Invasive LFP studies have also demonstrated a generation of high contrast gamma oscillations in V1 the primary visual cortex (V1), with an analogous effect being found in human MEG recordings [121,196].

Blood Oxygenation Level Dependent (BOLD) contrast is commonly used as a proxy for blood flow, and can be used to measure relative changes in CBF. However, BOLD relies on the balance between oxy- and deoxy-haemoglobin as a contrasting agent, resulting in alterations that can be susceptible to other physiological factors such as venous drainage, CMRO2, neurovascular coupling and high basal CBV [105,119,181,182]. Arterial Spin Labelling (ASL) involves labelling a bolus of blood coming up through the neck and capturing the decay of magnetisation within a region of interest. Though SNR is low, it does enable a more quantitative approach to CBF measurement [106,111].

Previous work investigating the similarities between visual evoked potentials (VEPs) as measured by EEG and visual evoked fields (VEFs) measured via MEG has shown the two to be

very comparable in waveform and peak latency [175,183,184]. Visually induced gamma band modulation occurs primarily in V1 and co-localises well with BOLD signal increases when presented with the same stimulus [122]. Co-localisation between these two measurements implies a similar source of signal for both modalities meaning either VEF amplitude or gamma band power can be used to assess V1 neuron activity along with BOLD, and by extension ASL-weighted measures used to assess related blood flow changes during a visual task.

In this study, I combine fMRI and MEG-based methods to empirically define NVC and assess its stability across multiple measurements to determine its suitability for use in patient populations. I aim to do this using blood flow alterations assessed through ASL and BOLD weighted images, generated from a visual stimulus of increasing contrast, regressed against visual evoked fields and gamma band oscillatory power in MEG as a neuronal measure. I hypothesise that as contrast increases so does VEF amplitude/gamma power and fMRI response within the visual cortex, allowing us to define NVC and assess its stability across measurements.

7-3 Methods

7-3-1 Subjects

15 healthy (mean age 23.9±2.16 (±SEM) years and 6 male 9 female respectively) volunteers were recruited. Informed consent was taken for all participants under ethical approval from the Cardiff University School of Psychology Ethics Committee. Subjects underwent 4 scans, conducted in 2 pairs; MEG-MRI, MEG-MRI. 5 subjects underwent the first pair of scans on the same day. 7 undertook the second pair on the same day. All other subjects had each scan on different days, but scans were conducted in the same pair order. The two MEG sessions were performed 10.6±2.6 days apart, MRI sessions were 12.5±2.7 days apart.

7-3-2 Visual paradigm

Contrast acuity for each eye was assessed on the first MEG session using a SLOAN letter chart at 100%, 25%, 10%, 5%, 2.5%, 1.25% and 0.6%, and all subjects apart from 4 required corrective lenses for daily use and wore them throughout the experiment. SLOAN letter charts consist of 10 specially formed letters which are also used in the more well known Snellen and logMAR charts. However SLOAN charts are readily available in a wide range of contrasts and therefore allows testing of a subject's acuity across their whole contrast detection range, rather than just at 100% contrast.

The main stimulus was a reversing checkerboard that was displayed at 6 contrast levels during both a MEG and MRI scan. Unlike in chapter 6, no grating was shown and a wider range of contrasts was utilised. The checkerboard was generated in Matlab® at 6 (0%, 6.25%, 12.5%, 25%, 50% and 100%) Michelson contrast levels in an attempt to accurately characterise the whole contrast response in both modalities and follows a similar approach used by Stevenson et al. (2011) where an attempt compare β- and γ-band responses across a range of stimulus strengths was made. This compares to Liang et. al. (2013) where only 1%, 5%, 10% and 100% contrasts were used, thereby leaving the middle, and upper contrast ranges relatively

uncharacterised by comparison. Checks were displayed at 1 cycles per degree (cpd) with a reversal rate of 2Hz. The entire stimulating field was 16° of visual angle. Subjects sat 80cm from the screen in MEG and 60cm in MRI, and the visual angle was matched in both scanners. Contrasts were displayed pseudorandomly for each participant, but contrast order was maintained between scan sessions for each subject. This paradigm was chosen in order to elicit both a measureable VEP response in MEG, evoked gamma oscillations, as well as producing a stimulus-induced increase in CBF.

As in chapter 6 each contrast was displayed for 30 seconds and repeated 4 times for a total viewing time of 2 minutes, rest periods of 0% contrast were displayed for a total of 4 minutes. The whole stimulus lasted 14 minutes and was repeated twice in each modality, once for each eye an example schematic of the contrast order can be seen in figure 7-1. The eye not being tested was covered using cotton makeup removal pads held in place with micropore tape. Eyes were switched round in each session so both eyes were tested. Eyes were tested separately in an effort to account for the effects of differences in visual acuity. If a subjects' visual acuity differs significantly between eyes, which is a concern with patients suffering from MS, then response magnitude can be affected. Responses could appear lower if both eyes are open but one eye has a significantly lower acuity than the other. However, there might not be a significant difference in measured acuity with both eyes open, due to a subject compensating for a reduced acuity in one eye with the unaffected eye. Therefore by testing eyes separately differences in acuity can at least partially be controlled for when assessing response strength. Checkerboards were displayed on a Sanyo XP41 LCD back-projection system in MEG and a Canon Xeed SX60 projector (1024x786 resolution 60Hz refresh rate) in MRI.

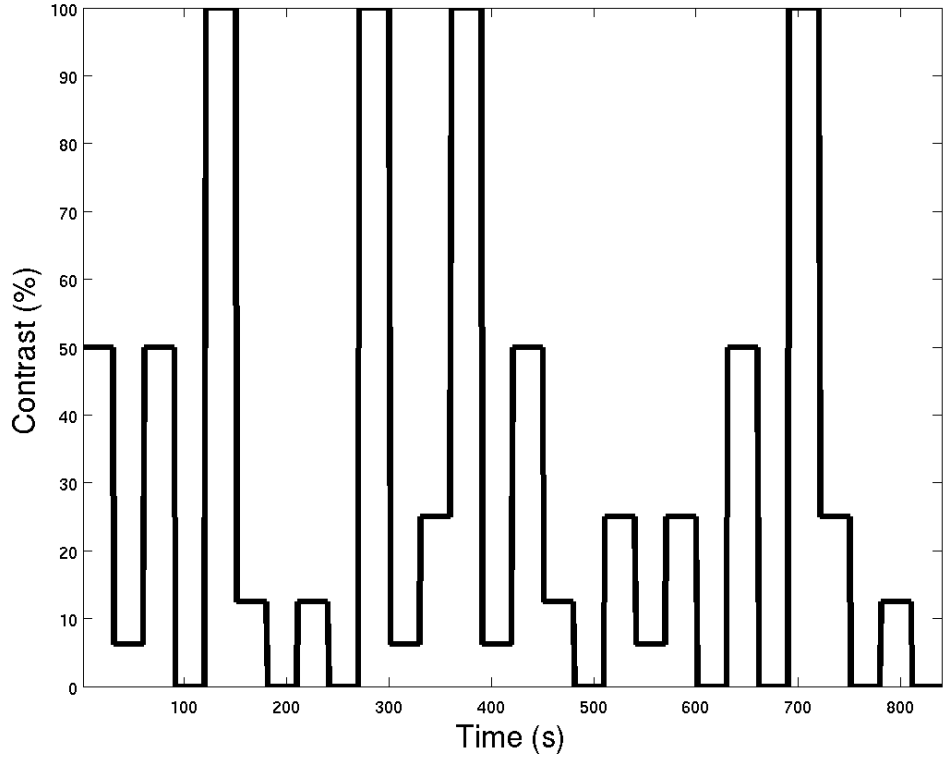

Figure 7-1 Representative schematic showing the randomised presentation of checkerboard contrast. Each bar represents 30 seconds of presentation with the height representation contrast. Sections of missing bars show the location of rest periods.

7-3-3 MRI

The main imaging protocol was kept identical to chapter 6. Images were captured on a 3 T whole body MRI scanner (GE Excite HDx, Milwaukee, WI, USA) with eight channel receive only head RF coil (Medical Devices). Simultaneous ASL and BOLD imaging data was collected for each subject during the checkerboard task using a PASL proximal inversion and control for off resonance effects (PICORE) Quantitative imaging of perfusion using a single subtraction (PICORE QUIPSS II) [189] imaging sequence with a dual-echo gradient echo (GRE) readout and spiral k-space acquisition (TE1 = 3ms, TE2 = 29ms, TR = 2.2s, flip angle = 90°, FOV=22cm, matrix=64x64, 12 slices of 7 mm thickness with an inter-slice gap of 1 mm acquired in ascending order, voxel size 3.4mmx3.4mmx7mm, TI1 = 700ms, TI2 = 1600ms for the most proximal slice and was incremented by 54.6ms for subsequent slices, tag thickness = 20 cm,

10 mm gap between labelling slab and bottom slice, 10 cm QUIPSS II saturation band thickness). This resulted in the acquisition of 382 volumes (191 tag control pairs). At the beginning of each session a calibration scan was captured for quantification of perfusion maps to calibrate longitudinal magnetisation of CSF (M_0) with the same scan parameters as the perfusion-weighted scan, but with no labelling and being captured at a fully relaxed state. Coil sensitivity was mapped using a minimum contrast image, acquired with the same acquisition parameters as before except TE = 11ms, TR = 2 s, and 8 interleaves.

A secondary, resting state scan was also performed to establish baseline CBF, allowing for absolute CBF change with contrast to be calculated.The resting state perfusion-weighted scan was performed with multiple inversion time (MTI) PASL [197] (10 inversion times (TIs)): 300ms, 400ms, 500ms, 600ms, 700ms, 800ms, 1000ms, 1100ms, 1400ms, 1700ms and 2000ms). A PICORE tagging scheme was used with a QUIPSS II cutoff at 700ms for TIs>700ms. Label thickness was 200mm, 16 control-tag pairs were acquired for each inversion time. High resolution anatomical (voxel size = 1x1x1mm^3, TE=29ms, repetition time = 7.8ms) FSPGR T1-weighted scans were acquired for use during registration.

7-3-4 MEG

MEG data capture was identical to the method laid out in chapter 6 for the checkerboard. Whole head MEG recordings were acquired using a CTF-Omega 275-channel radial gradiometer system sampled at 1200Hz. An additional 29 reference channels were recorded for noise cancellation purposes and the primary sensors were analysed as synthetic third-order gradiometers [185,190]. Three of the 275 channels were switched off due to excessive sensor noise. The location of three fiduciary markers (nasion, left and right preauricular) was monitored continuously through the MEG acquisition at a frequency of 10 Hz. For each checkerboard reversal, a TTL pulse was sent to the MEG system, data was acquired continuously and epoched offline in a window that extended 40ms before and 200ms after

the TTL pulse. Trials were manually excluded based on visibly identifiable artefacts. Eye movements were monitored throughout data acquisition to ensure subjects were attending the screen.

7-3-5 Analysis

7-3-5-1 MRI

The same analysis of functional data was performed here as described in chapter 6. Preprocessing of functional images was performed by first brain extracting all images using FSL-BET [155], motion correction was performed using MCFLIRT and highpass filtering of 120s was applied for BOLD and 70s for perfusion-weighted images and smoothed using a gaussian 5mm kernel. Functional images were registered first to subject's high resolution T1 structural scan, limited to 6 degrees of freedom, then to Montreal Neurological Institute (MNI) 152 space with 12 degrees of freedom. Both steps were linear warps [154].

Physiological noise correction was carried out prior to data processing, using a modified RETROICOR [192]. 1st and 2nd harmonics of cardiac and respiratory cycles (and the interaction term) were calculated in addition to variance related to heart rate (HR) [193] using a general linear model framework and regressed from the data.

For BOLD weighted images, interpolated surround averaging of the tag and control images was performed. The average of each slice was subtracted from the mean of its two neighbours, as described previously [194] to remove the tag-control signal from the dataset.

Resulting images were then analysed in FSL-FEAT [153] where a GLM was created for each checkerboard contrast, convolved with hemodynamic response factor, a temporal derivative was also added to represent a regressor of no interest..

For perfusion-weighted images, a sawtooth design was applied to model tag-control intensity alterations. The interaction between this and the contrast regressors were used to model ASL data (figure 7-2).

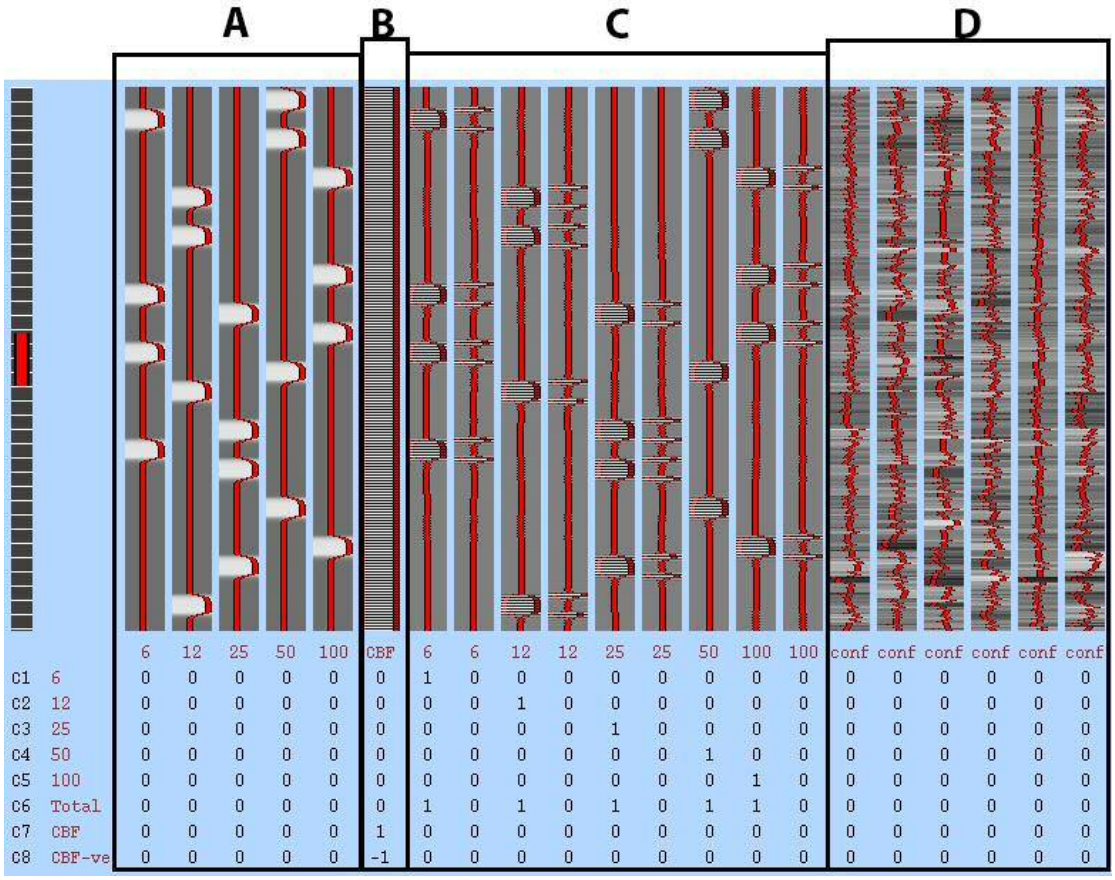

Figure 7-2 Representative design matrix of perfusion weighted images. Box A represents contrast order. Box B is the sawtooth design to model tag/controls pairs. Box C is the interaction term between contrast and tag/control labels, along with a temporal derivative EV. Finally box D shows motion parameters added to the model, these were obtained from FSL MCFLIRT.

Region of interest analysis was performed by multiplying an anatomical occipital lobe mask provided by FSL with binarised Z-statistic images (Z = 2.3) of averaged contrast activation generated from FEAT. Brain extracted functional images were registered to MNI-152 standard space via T_1-structual image. The transformation matrix was then inverted and applied to the occipital mask prior to restriction. Thus, a mask was generated for BOLD and perfusion images using the corresponding BOLD/CBF Z-statistic image. These masks were used to define ROIs with which to calculate percentage changes in both BOLD and CBF data in subject space in

response to the visual stimuli. The Harvard Oxford atlas for cortical and subcortical structures, available within FSL was used to obtain the occipital mask.

BOLD percentage changes in signal were calculated using FEATQuery from the FSL toolbox. For ASL data, mean tag-control signal difference extracted from FEAT analyses was used to define CBF during rest periods in the design. The ROI masks were then used for each subject to average voxel intensities for each visual contrast and divided by intensities for rest periods to generate a percentage signal change in CBF.

In addition to the task-related functional data baseline perfusion was calculated using a protocol as described by (Warnert *et al.,* 2014) using FSL BASIL. Briefly, CSF images were registered to perfusion series' using FSL-FLIRT [154]. This was used to create a mask of the lateral ventricles for calculation of $M_{0,CSF}$ allowing the equilibrium magnetization of blood ($M_{0,Blood}$) to be calculated [189]. A two compartment kinetic curve model as described in [113] was fitted to multi-inversion time data to calculate baseline perfusion in ml/100g/min along with mean arrival time [113,198]. A separate multi TI sequence was acquired for both scan sessions and was used with the percentage CBF increases during the task to determine increases in cerebral blood flow during each active contrast period.

7-3-5-2 MEG – VEF amplitude

Analysis of event related fields (ERFs) in sensor space was conducted using the FieldTrip toolbox for Matlab [191]. Time-locked analysis was performed on epoched raw data, following baseline correction, -40–200ms around each reversal.

Bandpass filtering was applied between 1-100Hz as described by[185] and limited from -40-200ms following reversal to allow a full range of evoked potentials to be analysed.

Source localisation using a multiple-spheres forward model[199] was derived from fitting spheres to the brain, extracted using FSL-BET [153]. Estimate maps of signal to noise were then embedded into MNI space with a smoothing of 8mm and peak activity was extracted.

A synthetic aperture magnetometry (SAM) beamformer derived from CTF software [141] was used to create differential images of evoked source power (pseudo-T statistics). This was then used calculate evoked related field activity comparing 0.04s (-0.04s-0s) prior to checkerboard reversal to 0.2s (0-2s) following checkerboard reversal.

Manual inspection of SAM images demonstrated subjects had between 2 and 3 peaks of activation within the right and left occipital lobes. To remove bias, the location of the peak with the strongest pseudo-T statistic was used as the location for placement of a 'virtual sensor' [121].

Following extraction, evoked fields were baselined, Butterworth filtered to 1-40Hz and normalised. Peak amplitudes were calculated by subtracting N70m amplitudes from P100m for each subject at each contrast, these were averaged across contrasts to give a single amplitude measure for each contrast and each participant.

7-3-5-3 MEG – Gamma power

Gamma power was determined in a similar manner to calculating VEF amplitude; each dataset was bandpass filtered using an IIR Butterworth filter to between 30-80Hz. Again, a SAM beamformer was used to create a pseudo-T statistic map comparing 0.24s (-0.04 – 0.2s) of rest averaged across a whole block to the same 0.24s of active checkerboard for each contrast. This revealed an area of increased power in the primary visual cortex, and virtual sensors were generated using SAM beamformer coefficients, returning the time-series from peak locations. Time frequency analysis was performed using the Hilbert transform from 1-100Hz in 0.5Hz steps and represented as a percentage change in gamma power from baseline, from this peak evoked gamma power change values from baseline were obtained[122].

7-3-6 Statistical analysis

Three-way ANOVA was used to assess the relationship between responses for each eye, session and stimulus contrast for each modality. Separate eye responses were then averaged and a power law was used to characterise coupling between MEG and fMRI-based measures[200]. A log-log plot was used to calculate the exponent and scaling factors of the relationship:

Repeatability was assessed using intraclass correlation coefficient (3,1) of the exponent (n) as described in [201]. All resultant values are shown as mean±SEM unless otherwise stated, though multiple comparisons have been corrected for using the Holm-Sidak method [202].

7-4 Results

Out of 15 participants, 3 were excluded due to excessive head motion. Excessive motion was characterised by movement within the MEG of greater than 20mm. Another participant was excluded for excessive artefacts in MEG that could not be corrected and resulted in SAM images without a main area of activation. 11 participants went through to final analysis.

Two way ANOVA testing visual acuity across contrasts revealed no significant difference between left and right eyes ($p=0.5$). An expected difference in acuity across contrasts was seen ($p < 0.001$). There was no interaction effect between visual acuity and eye (fig. 7-3).

No significant difference between eyes was observed ($P=0.5$) P100m amplitude showed a main effect of contrast ($F = 7.43$, $P < 0.001$) but no further effects of eye ($F = 0.377$, $P = 0.5$) or session ($F = 0.58$, $P = 0.45$) with no interaction effect seen between any factor.

Figure 7-4 shows VEF responses for each contrast in session 1 from a single representative subject.

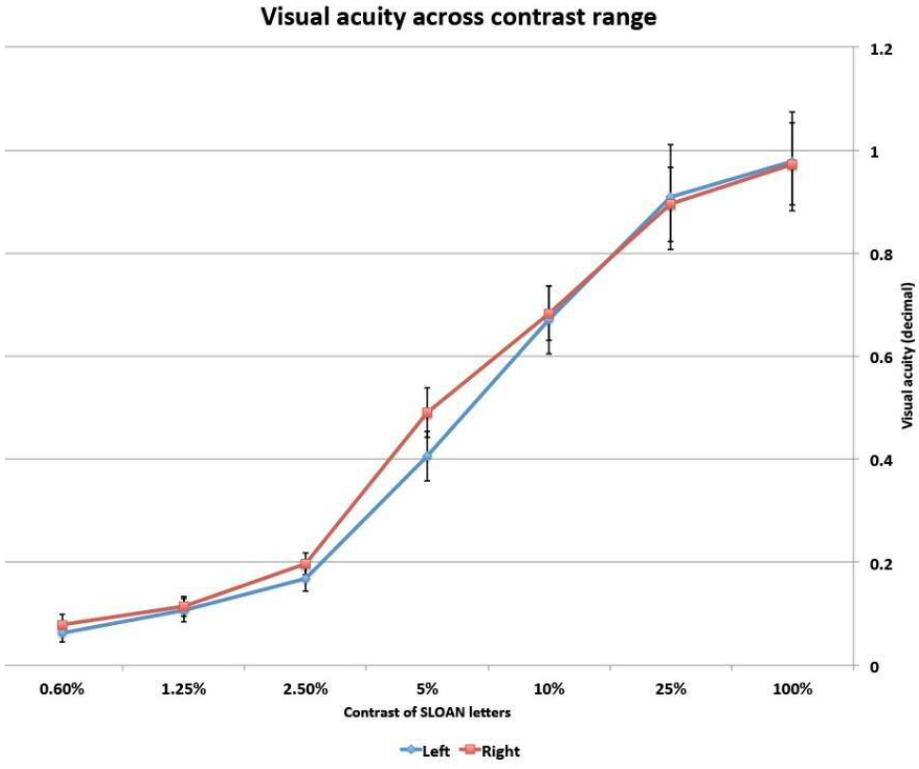

Figure 7-3 Average visual acuity for left and right eyes across contrast of a SLOAN letter chart. No significant difference between eyes was observed (P=0.5)

Gamma power similarly exhibited a main effect of contrast ($F = 68.12$, $P < 0.001$) and again no effect of eye ($F = 1.85$, $P = 0.18$) or session ($F = 0.029$, $P = 0.87$), no interaction effects were seen between any factor.

Figure 7-5 shows a single representative subject's spectograms used to calculate evoked gamma power at each contrast (6.25%-100% left to right), with the top row representing session 1, and the bottom row, session 2. Figure 7-6 shows the grand averaged spectograms of all subjects used in the analysis.

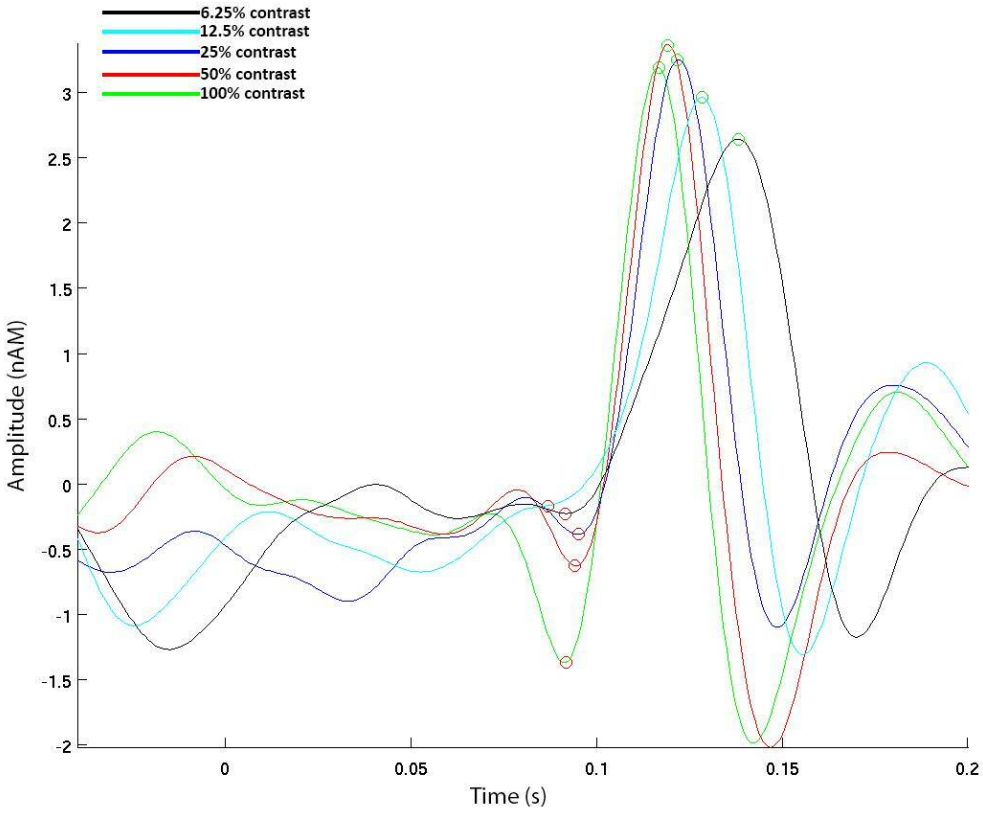

Figure 7-4 Representative trace of the three main components of the visual evoked potential from a single subject showing changes in amplitude with contrast. The first negative wave (N70) occurs between 65-80ms after stimulus onset (red circle). Followed by a positive deflection (P100) occurring between 95-110ms after onset (green circle). Finally, a negative deflection between 130-150ms (N140) finishes off the evoked potential. P100 amplitude was determined by subtracting peak N70 amplitude from P100 amplitude. Black = 6.25%, cyan = 12.5%, Blue = 25%, red = 50% and green = 100% contrast.

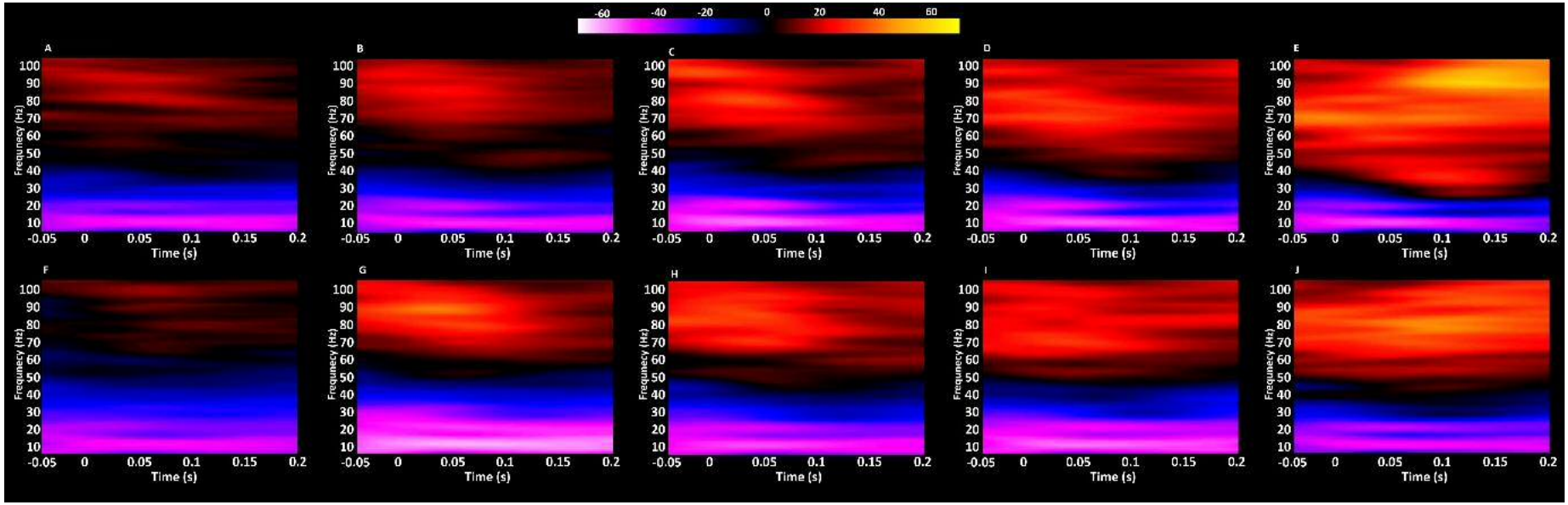

Figure 7-5 Trial averaged spectograms from a single representative subject (subject 13) showing full frequency responses of all contrasts: 6.25%, 12.5%, 25%, 50% and 100% for the left eye (A-E respectively) and right eye (F-J respectively). Images were generated from MEG virtual sensors constructed from peak locations in the visual cortex. As contrast increases there is a marked increase in broad band gamma power (40-100Hz), along with a continuous alpha/beta band suppression (9-12Hz/ 12-30Hz). All energy values are shown as percentage increases from baseline.

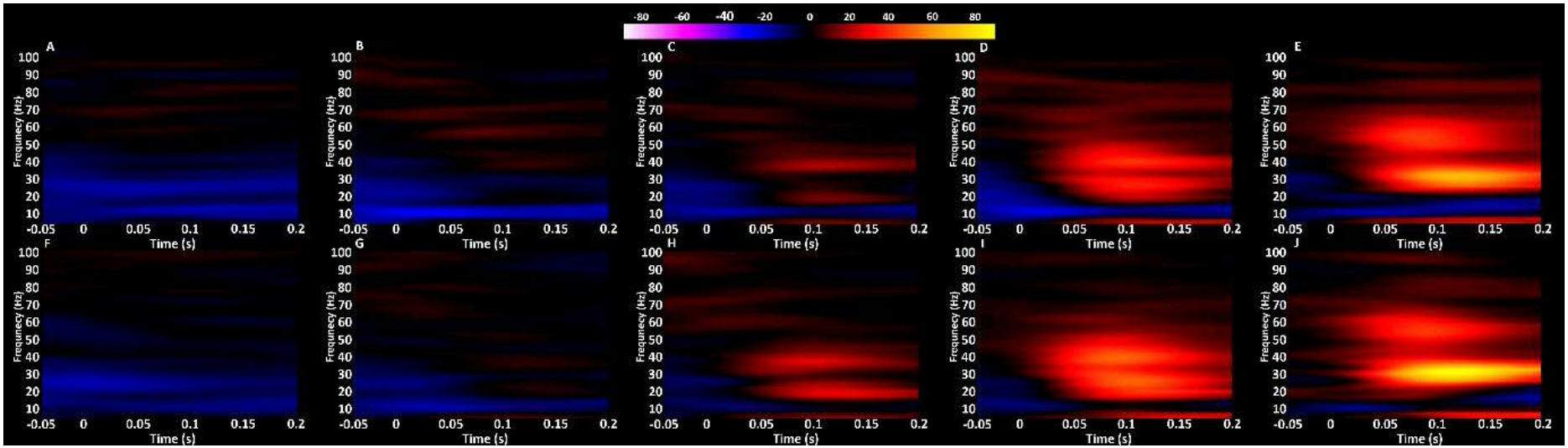

Figure 7-6 Grand averaged spectograms across contrasts from MEG virtual sensors constructed from peak locations in the visual cortex for session 1 (A-E) and session 2 (F-I). As with the individual spectograms in figure 4, as contrasts increases there is a strong increase in gamma power around two main frequency bands 30-50Hz and 50-70Hz. Suppression of the alpha band remains throughout all contrasts (9-12Hz). Energy values are represented as percentage change from baseline.

Time frequency responses were averaged across eyes for each subject, then averaged across subjects to create average spectrograms for each contrast at each time point.

There was no difference in occipital baseline CBF between session 1 and session 2 (66.4+/-4.3ml/100g/min and 69.94+/-3.6ml/100g/min $P = 0.36$ respectively. There was a significant alteration in stimulus induced CBF, with main effects of contrast ($F = 11.42$, $P < 0.001$) and session ($F = 41.85$, $P < 0.001$) but not eye ($F = 3.39$, $P = 0.07$), and no interaction effects between any factor were seen.

Finally, BOLD-weighted signal also demonstrated a significant main effect of contrast ($F = 58.44$, $P < 0.001$) but not eye ($F = 0.377$, $P = 0.5$) or session ($F = 0.62$, $P = 0.43$). No interaction effects were observed. The changes in respective signals are shown in figure 7-7; with the left column displaying data from the first session, and the right showing the second session (figure. 7-7). As there were no significant differences in responses between left and right eyes for any modality, this allowed averaging of responses across the two eyes.

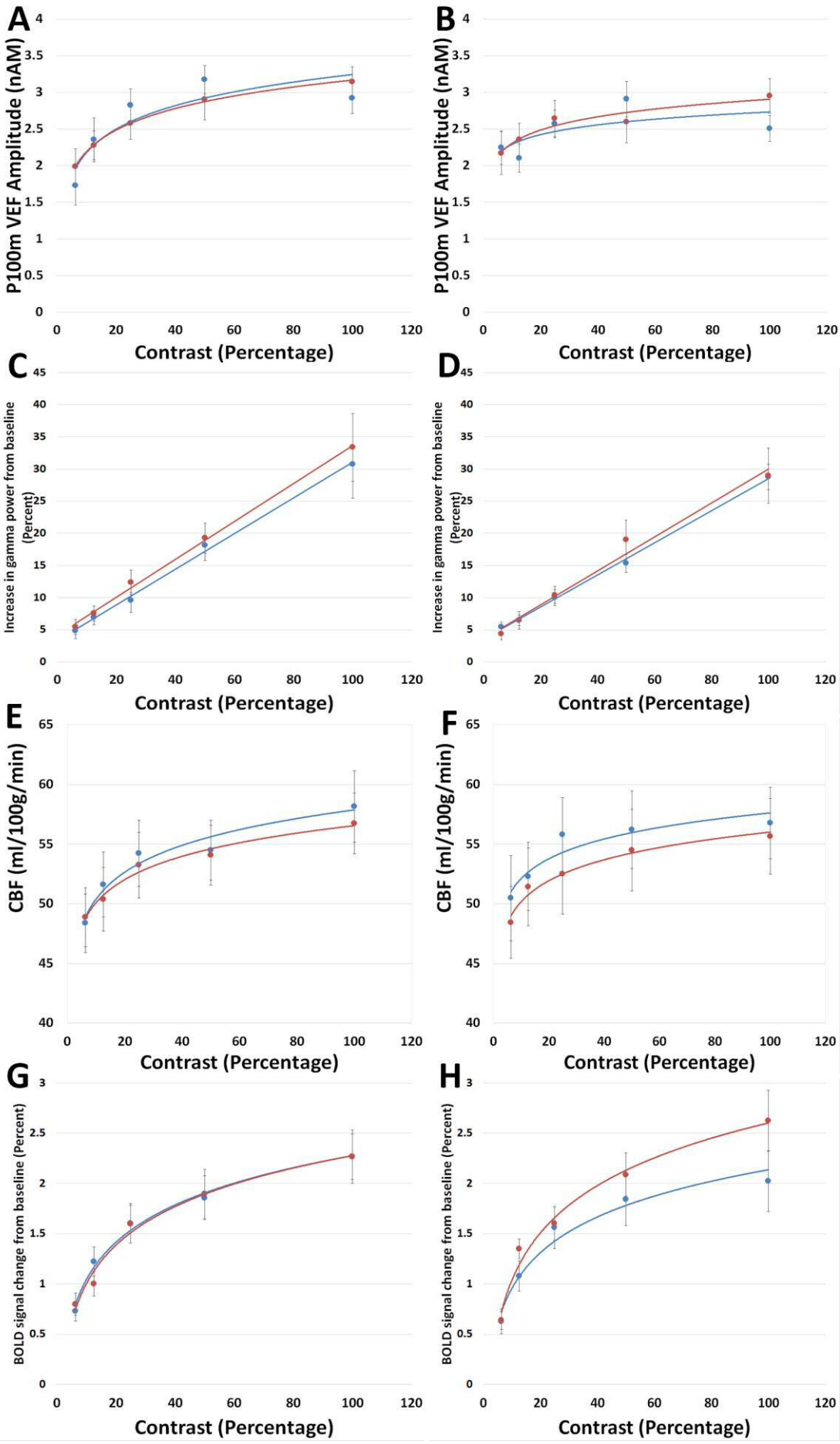
A
P100m VEF Amplitude (nAM)
Contrast (Percentage)
B
P100m VEF Amplitude (nAM)
Contrast (Percentage)
C
Increase in gamma power from baseline (Percent)
Contrast (Percentage)
D
Increase in gamma power from baseline (Percent)
Contrast (Percentage)
E
CBF (ml/100g/min)
Contrast (Percentage)
F
CBF (ml/100g/min)
Contrast (Percentage)
G
BOLD signal change from baseline (Percent)
Contrast (Percentage)
H
BOLD signal change from baseline (Percent)
Contrast (Percentage)

Figure 7-7 All graphs show responses in each modality against contrast of visual stimulus for left (blue lines) and right (red lines) eyes. A shows P100M VEF amplitudes against each contrast in the first session, B for the second session. A significant difference was observed between contrasts at both timepoints (p<0.001), with no significant difference in P100M amplitude detected between eyes or timepoint. E displays CBF changes with respect to contrasts for each eye tested at the first timepoint, F shows the second. A significant difference between CBF values for each contrast was demonstrated (p<0.001) and timepoint (p<0.001) but not between eyes. G displays BOLD-weighted signal changes between each contrast for left and right eyes at the first timepoint, H displays the second time point. A significant alteration in BOLD signal was observed between contrasts (p<0.001) but not between timepoint or eye. No interaction effects were seen between any factor for each modality. Blue = left eye, red = right eye.

To assess the repeatability of each modality, the exponent (n) values for each subject were calculated from a log-log plot of MR and MEG values against contrast at both time points. This allowed for ICC(3,1) to be performed for each modality between time points. All ICC values are summarised in table 7-1. Visualisation of response stability between sessions can be seen in figure 7-8; responses with the highest stability exhibited a similar n values for session 1 and 2 in each modality. The R2 values in table 7-1 were calculated from a trend line fitting these plots.

	Exponent *N*			
Visit 1 vs Visit 2	**ICC**	**F**	***P***	**R^2**
VEF	-0.067	0.87	0.6	0.001
Gamma	0.9	14	<0.001	0.8
CBF	0.5	3.3	0.045	0.3
BOLD	0.67	5	0.0086	0.6

Table 7-1 Summary of ICC values for the β for each modality regressed against contrast level for session 1 and session 2. All show a highly significant, positive ICC value, apart from VEF amplitude. This signifies a high level of stability of the measurements between sessions for percentage gamma change, CBF and BOLD signal change with contrast but not VEF amplitude

Finally, to assess stability of the overall measure of NVC, *n* was extracted by regressing each MR measure against each MEG measure. Both for each modality's corresponding session and again for the other time point (e.g. MEG responses on the first visit vs MR-based responses on the first visit, then MEG responses on the second visit vs MR-based responses on the first visit). ICC values in table 7-2 were calculated for each combination of session in respective modalities to determine if the effect session order had on ICC calculations. Plotting *n* values shows a high R^2 for gamma-based measures of

NVC regardless of session order (figure 7-9 A, B, E, F), but not VEF-based measures of NVC (figure 7-9 C, D, G, H).

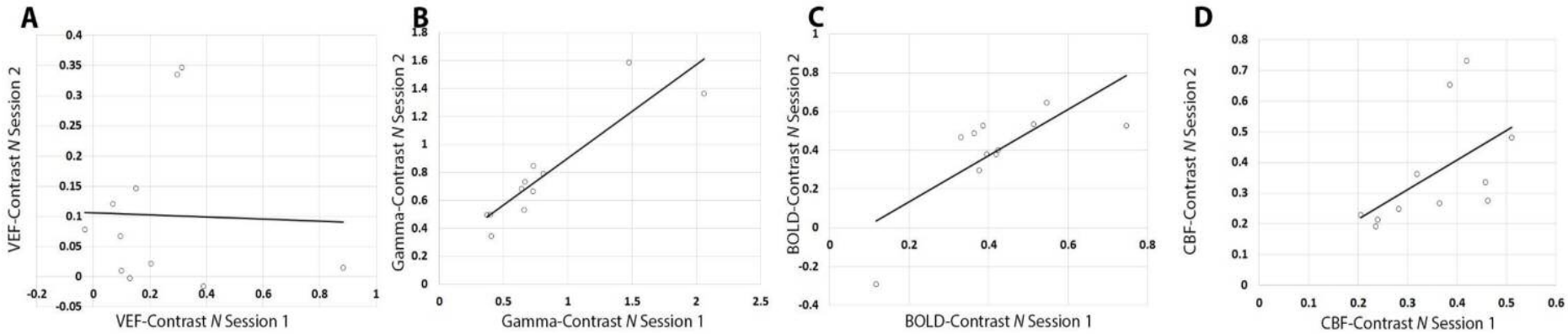

Figure 7-8 Neuronal and blood flow measures regressed against contrast and N values plotted for session 1 and session 2. VEF amplitudes demonstrated poor stability between the two sessions (A) with an ICC value of -0.67 (p=0.6). B shows gamma power regressed against contrast for session 1 vs session 2. This exhibited high stability (ICC = 0.9 p < 0.001). BOLD-based blood flow measures (C) also showed a good stability over the two sessions (ICC = 0.67 p = 0.0086). As did CBF measured through perfusion-weighted imaging (D) (ICC = 0.5 p = 0.045).

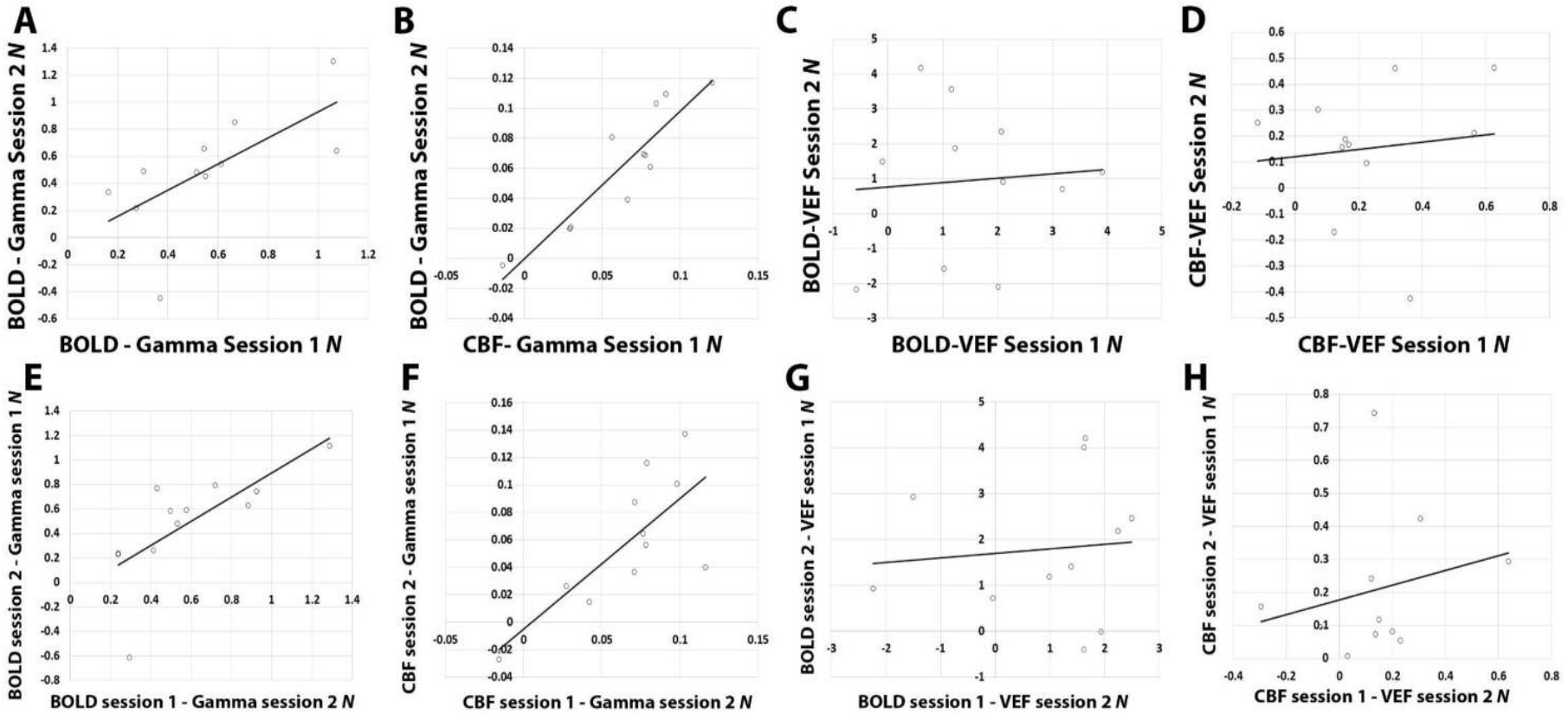

Figure 7-9 Neuronal and blood flow measures regressed against each other and N values plotted for session 1 and session 2. Gamma oscillatory-based measures of neuronal activity regressed against blood flow measures shows good stability between sessions (A and B, ICC = 0.63 p = 0.01 and ICC = 0.69 p = 0.0013 respectively). VEF-amplitude-based coupling with blood flow measures does not show the same tight coupling and stability between sessions (C and D, ICC = 0.07 p = 0.42 and ICC = 0.11 p = 0.37 respectively). Mixing session order for each modality revealed a similar tight coupling between gamma-based NVC measures (E and F, ICC = 0.69 p = 0.0068 and ICC = 0.72 p = 0.0041 respectively)), but VEF-based NVC still exhibited weak stability between sessions (G and H, ICC =0.1 p =0.37 and ICC = 0.28 p = 0.19 respectively).

					Linear Regression	
Coefficient order	**ICC**	**F**	***P***	**R^2**	**Exponent *N***	***P***
VEF 1 - CBF 1 vs VEF 2 - CBF 2	0.11	1.26	0.37	0.02	0.177	<0.01
VEF 2 - CBF 1 vs VEF 1 - CBF 2	0.28	1.79	0.19	0.06	0.178	<0.01
Gamma 1 - CBF 1 vs Gamma 2 - CBF 2	0.86	13.3	0.0013	0.8	0.063	<0.001
Gamma 2 - CBF 1 vs Gamma 1 - CBF 2	0.72	6.14	0.0041	0.6	0.064	<0.001
VEF 1 - BOLD 1 vs VEF 2 - BOLD 2	0.07	1.1	0.42	0.006	1.69	<0.05
VEF 2 - BOLD 1 vs VEF 1 - BOLD 2	0.1	1.22	0.37	0.008	1.39	<0.01
Gamma 1 - BOLD 1 vs Gamma 2 - BOLD 2	0.63	4.3	0.01	0.5	0.53	<0.001
Gamma 2 - BOLD 1 vs Gamma 1 - BOLD 2	0.69	5.3	0.0068	0.5	0.52	<0.001

Table 7-2 Summary of ICC and linear regression results for different session orders. The β of each pair of measurements at the shown sessions were used to calculate ICC. The order of session of gamma power and MRI measures does not appear to influence the ICC of these measures, gamma-CBF coupling ICC show similar results of 0.79 and 0.63 for corresponding and mixed session orders, other of which remain significant. The same is seen for gamma power-BOLD coupling, both exhibit an ICC of 0.8 and remain highly significant. The same cannot be seen in VEF-MRI coupling; with VEF-CBF coupling having a low non-significant ICC of 0.22 when comparing corresponding sessions, and a more positive but still non-significant ICC of 0.48 with mixed sessions. VEF-BOLD coupling appears to be more stable with both corresponding and mixed session analysis showing positive ICC values. However, only corresponding sessions have a significant ICC, with mixed sessions showing a trend towards significance but not quite reaching it. Finally, the significance of the regression was checked by averaging β coefficients from each combination of session/modality, with a one-way T-test being used to check for a significant difference from 0. All modalities and all combination of sessions exhibited a significant regression with each other

Regressing MRI with MEG measures, and using a one sample T-test, assessing the mean regression slope across eye and session to be greater than 0, revealed a significant relationship between VEF amplitude and CBF across contrasts ($P < 0.01$, CBF = 48.2*VEF amplitude$^{0.177}$), VEF and BOLD ($P < 0.05$, BOLD signal change = 1.34*VEF amplitude$^{1.69}$). Regression of gamma power against MRI measures also yielded a significant relationship between gamma power and CBF ($P < 0.001$, CBF = 46.4*Gamma Power$^{0.064}$) as well as with BOLD-weighted signal ($P < 0.001$, BOLD signal change = 0.5*Gamma Power$^{0.53}$) (table 7-2). This relationship is shown more clearly in figure 7-10, here, contrast responses have been averaged across eyes and session to demonstrate the coupling between the two measures of neuronal activity and CBF.

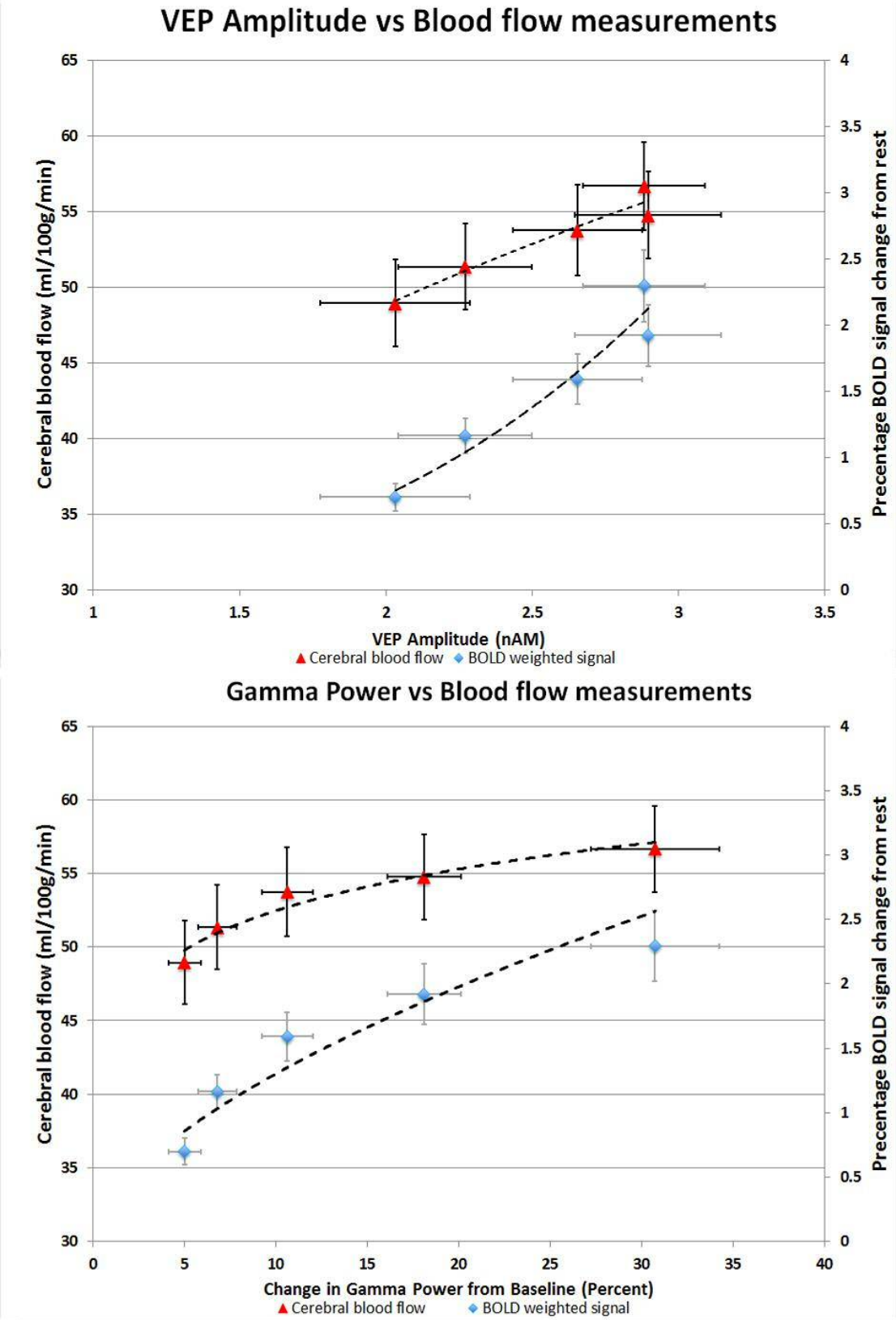

Figure 7-10 Average regression plots of VEF amplitudes against MR measures and percentage gamma power alteration against MR measures. Each point represents a contrast. There was a significant relationship between VEF amplitude and perfusion-weighted signal ($p<0.001$), however there was no significant relationship between VEF amplitude and BOLD-weighted signal changes when interrogating individual subject relationships ($p=0.1$), even though there appears to be one when data is averaged. Gamma power-CBF coupling was promising with a significant logarithmic relationship exhibited ($p<0.001$), with a similar relationship seen in gamma-BOLD coupling ($p<0.001$).

7-5 Discussion

Here I attempted to empirically define and assess the stability of neurovascular coupling in the human visual cortex across multiple measurements. The attempt to use VEF amplitude to gain a temporally stable method for measuring NVC was unsuccessful, the poor temporal stability shown here would make it a poor longitudinal measure of NVC. I have been able to define a temporally stable method for assessing NVC using gamma power as the neuronal component of NVC. Both BOLD and ASL-based methods for measuring change in blood flow were temporally stable and therefore could both be used for studying NVC.

There is little consensus over the nature of the relationship between event related potentials and vascular measures. Several groups reporting conflicting results, finding both linear and nonlinear correlations with stimulus intensity[171,203,204]. Here I noted a non-linear relationship with stimulus intensity with vascular responses, saturating at higher contrasts (figure 7-7 E-H).

VEF amplitude also exhibited a non-linear relationship with contrast, but a non-linear relationship was noted between gamma oscillatory power and contrast (figure 7-7 A-D) in agreement with previous studies[128]. It has been previously noted that P100 amplitude is the most stable and reliable of the three VEF components [205]. As the N75 peak is highly variable, particularly at low contrast, it is likely a large proportion of the between session variability seen for VEF measurements is due to my method for determining P100 amplitude.

Due to the slow time course of the haemodynamic activity, it has often considered as a summation of fast acting neuronal responses over time, and has therefore assumed to be a linear coupling between the two[121,206]. Studies combining neuronal measures with flow-based techniques have instead noted a saturation effect of blood flow at high neuronal activation levels in the visual cortex. While evoked potential amplitude increases linearly with stimulus intensity (contrast or flicker rate), saturation of blood flow is observed, in agreement with this study[206,207].

Over long stimulation periods both BOLD and VEF amplitudes have been shown to exhibit habituation, resulting in a lower response over time for a given stimulus intensity [117,203]. As there are many factors affecting BOLD signal change other than cerebral blood flow, it is not a quantitative measure of CBF, but could have potential use as an indicator of relative CBF changes in NVC. Furthermore, ASL-based measures of CBF have been shown to have a higher stability over time compared to BOLD [112].

The low ICC exhibited by VEF amplitude would indicate a lower temporal stability and would therefore be less suitable for NVC measurement, contradicting other groups' findings of high test-retest stability of VEP amplitudes [105,115].

This does not apply when coupling vascular measures to gamma oscillatory power. Both induced and evoked gamma band responses have been shown to increase linearly with respect to contrast, a similar relationship seen here (figure 7-7 C+D)[125]. This is a trend also observed in intracranial recordings in monkey, suggesting my data is a good representation of the underlying neurophysiology[118,127,187,208]. As evoked gamma is a broadband activity with some subjects showing augmentation across the whole gamma range (figure 7-5) it does not suffer from the same dissociation from neuronal firing rates seen in narrowband-induced gamma[127]. High ICC values for evoked gamma amplitude are also in agreement with[185], demonstrating high test-retest stability of measurements over time, and shows promise in defining NVC.

The high stability of coupling using gamma power is summarised in table 7-2, where ICC values remain similar and with a high significance for gamma-based NVC measures regardless of session order during analysis. As a similar trend cannot be seen in VEF-based NVC calculations it would seem to be a poor representation of underlying neurophysiology with one group finding significant correlations between VEP amplitude and CBF[180]. Instead, what I observe here is a brief spike in broadband gamma oscillatory power in response to checkerboard reversal. Blood flow increases saturate at high contrast levels however, presumably due to the limit of arterioles' ability to dilate further.

In conclusion, the methods presented here represent an attempt to empirically define neurovascular coupling, and assess the stability of this measure across time. I have been able to demonstrate a relationship between two neuronal measures and two blood flow measures in response to a contrast-based visual task. VEF amplitude showed poor stability over time, making it a poor candidate for further investigation of NVC, with evoked gamma band oscillatory power instead being a better choice. Both BOLD and ASL-weighted measures of CBF showed strong coupling with gamma band power. This remains true even when the order of sessions is mixed during analysis adding weight to this measure being the most useful in further investigating NVC.

Chapter 8: Neurovascular coupling in multiple sclerosis

8-1 Abstract

Following on from chapter 7 where I assessed the most reliable method for measuring neurovascular coupling, I aimed to determine the extent to which this is affected in a pathological state such as multiple sclerosis given the reduced CVR seen in this patient group. 14 patients with relapsing-remitting multiple sclerosis (RRMS) and 12 age and sex matched healthy volunteers underwent an MEG and fMRI scan that were performed on the same day. A reversing square wave checkerboard was used at 2Hz and shown at 6 contrast levels (0%, 6.25%, 12.5%, 25%, 50% and 100%) to detect changes in gamma power and blood flow alterations, measured via MEG and BOLD/ASL fMRI respectively. The neuronal measure (gamma power) was then regressed against alterations in BOLD- and perfusion-weighted signal changes in MR, the exponent (*n*) values of a power law defining an empirical measure of neurovascular coupling (NVC). Patients exhibited a significantly lower gamma power increase in response to the reversing checkerboard contrast compared to healthy controls ($p < 0.05$). However, none of the blood flow measures (absolute CBF, percent/absolute CBF change and percent BOLD signal change) showed any significant difference. When determining neurovascular coupling (defined as the exponent of a power law function regressing blood flow measures against gamma power change), there was a strong trend towards a lower NVC in patients when using absolute CBF as a blood flow measure in NVC ($p = 0.1$). There is promise for this technique to be used to assess the link between neural activity and CBF, particularly disease states

8-2 Introduction

Cerebrovascular reactivity is crucial to maintaining proper NVC. As we have seen in chapter 5, CVR is impaired in Multiple Sclerosis patients, and is normalised following interferon-β treatment. Using the new methods for testing NVC outlined in chapter 7, I aim to test to what extent NVC is altered in MS patients given their impaired CVR to CO_2. If there is an alteration in NVC in MS patients, this could have wide implications for both the mechanism through which axonal loss could be occurring as well as possible avenues of MS treatment to halt further damage. As several histopathological studies have shown hypoxia-like tissue injury in MS brains, this lends support to the notion of impaired NVC as well as CVR in MS[34,145,209]. In addition to this, increased nitric oxide (NO) and endothelin-1 (ET-1) expression have a range of implications for the state of perfusion in MS sufferers. There is conflict in the literature about whether MS sufferers are chronically hyper- or hypo-perfused at rest due to the expression of these two vasoactive compounds respectively[48,51,52,57,166,209,210]. However, in either case this could have a severe impact on NVC and the response of the vasculature to a neuronal stimulus.

One of the common initial presentations of multiple sclerosis (MS) is optic neuritis (ON). ON is an acute unilateral visual impairment characterised by a reduction in visual acuity and reduced structural connectivity values in affected optic radiations, optic nerves and associated visual pathways[5,205]. Even in the absence of visual impairment patients with MS exhibit optic nerve atrophy, demyelination and axonal loss in the retinal nerve fibre layer[211]. Clinically, pattern reversal visual evoked potentials (VEPs) are used, along with high contrast visual acuity tests to assess damage to the visual pathway, and make up part of Kurtzke's extended disability score (EDSS). Here the P100 portion of the evoked potential is used as it is the least variable of the three portions of the VEP (the other two being N75 and N145 mentioned previously)[205]. During both ON and MS P100 latency increases and amplitude decreases compared to healthy controls which is thought to represent demyelination and axonal loss along the optic pathway respectively[174,211,212]. It is therefore important to still use VEPs to assist in determining the damage along the visual pathway of any patient group. It is important to note however, while high contrast Snellen charts are typically used to assess visual acuity in MS, results

from these tests do not correlate well with disease activity, EDSS score, or optic nerve demyelination measures. Instead researchers are moving towards using SLOAN low contrast charts to determine visual acuity, as it appears to be more sensitive to damage and therefore is more appropriate to use in pathological states involving the visual pathway[211–213].

I have been able to demonstrate altered vascular reactivity in MS patients, which is restored following treatment with interferon beta in chapter 5. This alteration gives considerable indication to the disruption of normal vessel function caused by both inflammation and other vasoactive compounds such as NO and ET-1. As only CO_2 was used in chapter 5 to assess vascular reactivity a more appropriate, neurological stimulus would be useful to determining how far this dysfunction can occur. Cerebral hypoperfusion has been established in the literature and has been indicated to be caused – in part – by the action of ET-1 acting through ET-1_a receptors in smoother muscle cells[47,48,51,209]. However, as the actions of ET-1 do not appear to have any effect on inducible isoforms of NOS (iNOS) coupling between neurons and blood flow might still be preserved[214].

In chapter 7 we concluded that P100m amplitude is less appropriate a neural measure compared to gamma power to use in NVC due to its high temporal variability contradicting previous work[187,208]. Here I intend to focus on using gamma power as a neuronal activation marker and, along with blood flow measures using ASL/BOLD imaging attempt to distinguish any alteration in NVC given the reduced vascular reactivity to CO_2 seen in chapter 5. As in chapter 5 I was able to demonstrate a decrease in vascular reactivity in MS patients compared to healthy volunteers, I am expecting to see a decrease in the haemodynamic response in MS patients from neuronal stimulation. As there is evidence of GM damage in patients, even in the early stages of MS, representing neuronal cell loss, I am also expecting to see a decrease in the gamma power of patients in response the visual checkerboard task. As inflammation is known to interfere with multiple forms of cell-cell signalling, I also hypothesise a decoupling of neurovascular coupling in MS patients compared to healthy volunteers.

8-3 Methods

8-3-1 Participants

14 patients with a diagnosis of MS according to the revised diagnostic criteria (Polman C et al, 2005), were eligible to start IFN beta, but were not currently on any disease modifying treatments, and had not experienced a relapse in the last 3 months were recruited at University Hospital Wales, Cardiff. Patients were assessed with behavioural measures before MEG and MRI scans were undertaken. 12 age-matched healthy volunteers were assessed with the same behavioural measures. Participants were not asked to alter their lifestyle habits prior to scanning. Participants' written consent was obtained according to the protocol approved by REC Wales, and NHS R&D Wales.

8-3-2 Visual paradigm

Contrast acuity was assessed prior to the MEG scan session using the same protocol as described in chapter 7-3-2. A SLOAN letter chart was shown at 100%, 25%, 10%, 5%, 2.5%, 1.25% and 0.6% to establish acuity across the contrast range, and all subjects apart from 5 required corrective lenses for daily use and wore them throughout the experiment.

The main stimulus was the same one used in chapter 7, with no modifications. The reversing checkerboard displayed at 6 contrast levels displayed during both a MEG and MRI scan. The checkerboard was generated in Matlab® at 6 (0%, 6.25%, 12.5%, 25%, 50% and 100%) Michelson contrast levels, the same contrasts that were used in chapter 7. Checks were displayed at 1 cycle per degree (cpd) with a reversal rate of 2Hz. The entire stimulating field was 16° of visual angle. Subjects sat 80cm from the screen in MEG and 60cm in MRI, and the visual angle was matched in both scanners. Contrasts were displayed pseudorandomly in the same order for both MEG and MRI for each participant and session. This paradigm was chosen to elicit both a measureable VEP response in MEG, and evoked gamma oscillations, as well as producing a stimulus-induced increase in CBF.

Timings for each contrast were kept the same as in chapter 7. In the previous chapter, there were no differences in responses between eyes, but as there were no significant differences in visual acuity

between subjects' eyes, this is to be expected. However, due to optic neuritis being a common complaint in MS patients, eyes are tested separately here, as the likelihood of a significant difference in visual acuity between eyes being much higher than in healthy volunteers. Checkerboards were displayed on a Sanyo XP41 LCD back-projection system in MEG and a Canon Xeed SX60 projector (1024x786 resolution 60Hz refresh rate) in MRI.

8-3-3 MRI

The whole imaging protocol was kept identical to chapter 7-3-3. Images were captured on a 3-T whole body MRI scanner (GE Excite HDx, Milwaukee, WI, USA) with eight channel receive only head RF coil (Medical Devices). Simultaneous ASL and BOLD imaging data was collected for each subject during the checkerboard task using a PASL proximal inversion and control for off resonance effects (PICORE) Quantitative imaging of perfusion using a single subtraction (PICORE QUIPSS II)[189] imaging sequence with a dual-echo gradient echo (GRE) readout and spiral k-space acquisition (TE1 = 3ms, TE2 = 29ms, TR = 2.2s, flip angle = 90°, FOV=22cm, matrix=64x64, 12 slices of 7 mm thickness with an inter-slice gap of 1 mm acquired in ascending order, voxel size 3.4mmx3.4mmx7mm, TI1 = 700ms, TI2 = 1600ms for the most proximal slice and was incremented by 54.6ms for subsequent slices, tag thickness = 20 cm, adiabatic hyperbolic secant inversion pulse, 10 mm gap between labelling slab and bottom slice, 10 cm QUIPSS II saturation band thickness). This resulted in the acquisition of 382 volumes (191 tag control pairs). At the beginning of each session a calibration scan was captured for quantification of perfusion maps to calibrate longitudinal magnetisation of CSF (M_0) with the same scan parameters as the perfusion-weighted scan, but with no labelling and being captured at a fully relaxed state. Coil sensitivity was mapped using a minimum contrast image, acquired with the same acquisition parameters as before except TE = 11ms, TR = 2 s, and 8 interleaves. To establish baseline CBF allowing for absolute CBF change with contrast to be calculated, an additional resting perfusion-weighted scan was performed with MTI PASL[197] (10 inversion times (TIs)): 300ms, 400ms, 500ms, 600ms, 700ms, 800ms, 1000ms, 1100ms, 1400ms, 1700ms and 2000ms). A PICORE tagging scheme was used with a QUIPSS II cut-off at 700ms for TIs>700ms. Label thickness was 200mm, 16 control-tag pairs were

acquired for each inversion time. High resolution anatomical (voxel size = 1x1x1mm^3, TE=29ms, repetition time = 7.8ms) FSPGR T1-weighted scans were acquired for use during registration.

8-3-4 MEG

The MEG data acquisition was identical to what was described in chapter 7-3-4. Whole head MEG recordings were acquired using a CTF-Omega 275-channel radial gradiometer system sampled at 1200Hz. An additional 29 reference channels were recorded for noise cancellation purposes and the primary sensors were analysed as synthetic third-order gradiometers[185,190]. Three of the 275 channels were switched off due to excessive sensor noise. The location of three fiduciary markers (nasion, left and right preauricular) was monitored continuously through the MEG acquisition at a frequency of 10 Hz. For each checkerboard reversal, a TTL pulse was sent to the MEG system, data was acquired continuously and epoched offline in a window that extended 40ms before and 200ms after the TTL pulse. Trials were manually excluded based on visibly identifiable artefacts.

8-3-5 Analysis

8-3-5-1 MEG

Gamma power was determined in the same manner as described in section 7-3-5-3; each dataset was bandpass filtered using an IIR Butterworth filter to between 30-80Hz. A SAM beamformer was used to create a pseudo-T statistic map comparing 0.24s (-0.04 – 0.2s) of rest block to 0.24s of active checkerboard for each contrast. This revealed an area of increased power in the primary visual cortex, and virtual sensors were generated using SAM beamformer coefficients, returning the time-series from peak locations. Time frequency analysis was performed using the Hilbert transform with time/frequency spectrograms displayed as a percentage change in gamma power from rest [122].

8-3-5-2 MRI

All MRI analysis was performed in the same way described in 7-3-5-1. Pre-processing was performed by first brain extracting all images using FSL-BET[155], motion correction was performed using MCFLIRT and high pass filtering of 120s was applied for BOLD and 70s for perfusion-weighted

images and smoothed using a Gaussian 5mm kernel. Functional datasets were registered first to subject's high resolution T1 structural scan, limited to 6 degrees of freedom, then to Montreal Neurological Institute (MNI) 152 space with 12 degrees of freedom. Both steps were linear warps performed using FSL-FLIRT[154].

Physiological noise correction was carried out prior to data processing, using a modified RETROICOR[192]. 1st and 2nd harmonics of cardiac and respiratory cycles (and the interaction term) were calculated in addition to variance related to heart rate (HR)[193] using a general linear model framework and regressed from the data.

For BOLD weighted images, interpolated surround averaging of the tag and control images was performed. The average of each slice was subtracted from the mean of its two neighbours, as described previously[194] to remove the tag-control signal from the dataset.

Resulting images were then used in FSL-FEAT[153] where a GLM was created for each contrast, with a gamma hemodynamic response factor added as well as a temporal derivative (figure 7-2).

For perfusion-weighted images, a sawtooth design was applied to model tag-control intensity alterations. The interaction between this and the contrast regressors were used to model ASL data (see figure 7-2 for an example).

Region of interest analysis was performed by multiplying an anatomical occipital lobe mask provided by FSL with binerised Z-statistic images (threshold z = 2.3) of averaged contrast activation generated from FEAT. Thus, a mask was generated for BOLD and perfusion images using the corresponding BOLD/CBF Z-statistic image for each subject. These masks were used to define ROIs with which to calculate percentage changes in both BOLD and CBF data in subject space. The Harvard Oxford atlas for cortical and subcortical structures, available within FSL was used to obtain the occipital mask. Brain extracted functional images were registered to MNI-152 standard space via T_1-structual image. The

transformation matrix was then inverted and applied to the occipital mask prior to restriction using the appropriate Z-statistic image.

BOLD data percentage changes in signal were calculated using FEATQuery from the FSL toolbox. For ASL data, mean tag-control signal difference extracted from FEAT analyses were used to define CBF during rest periods in the design. The ROI masks were then used for each subject to average voxel intensities for each contrast and divided by intensities for rest periods to generate a percentage signal change in CBF.

Baseline perfusion was calculated using a protocol as described by Warnert *et al.,* 2014 using FSL BASIL. Briefly, CSF images were registered to perfusion series' using FSL-FLIRT[154]. This was used to create a mask of the lateral ventricles for calculation of $M_{0,CSF}$ allowing the equilibrium magnetization of blood ($M_{0,Blood}$) to be calculated[189]. A two compartment kinetic curve model as described in[113] was fitted to multi-inversion time data to calculate baseline perfusion in ml/100g/min along with mean arrival time [113,198]. A separate multi TI sequence was acquired and used with the percentage CBF increases during the task to determine increases in cerebral blood flow during each active contrast period.

8-3-6 Statistical Analysis and modelling of neurovascular coupling

Separate eye responses were averaged together following two-way ANOVA to assess the relationship between eye and contrast. A power law function was then used to characterise the relationship between each modality and contrast:

Coupling was then assessed using a similar power law fitting changes in gamma power and blood flow response. The exponent of which (n) was used as the measure of NVC:

Multiple regression was used to assess how age, visual acuity, cohort, checkerboard contrast and baseline CBF could affect NVC in these subjects. All resultant values are shown as mean±SEM unless otherwise stated, though multiple comparisons have been corrected for using the Holm-Sidak method[202].

8-4 Results

Of the 27 subjects recruited to take part, all but 5 needed corrective lenses for the visual acuity tests and during scans. Of the patients 1 was excluded for excessive movement in MEG defined as movement >20mm and 1 felt claustrophobic in the MRI meaning that part of the study was not completed. Of the controls one due to be scanned was excluded due to not meeting the screening criteria and another was excluded due to excessive motion in MEG. In total 13 patients and 10 controls went through to analysis. A summary of volunteer characteristics can be found in table 8-1.

One-way ANOVA testing visual acuity between left and right eyes revealed no significant difference in acuity between eyes in either cohort ($F = 1.42$, $P = 0.2$ and $F = 0.73$, $P = 0.4$ in controls and patients respectively). Following this, visual acuity scores were averaged across eyes. Multiple regression was performed for visual acuity data, changes in visual acuity could be determined by a combination of SLOAN letter contrast and age ($p < 0.001$ and $p < 0.05$ respectively) with group (healthy control or patient) having no significant contribution ($p = 0.98$) (fig. 8-1).

Two-way ANOVA was used to assess modality responses in each eye for patients and controls to further determine any difference between eyes.

In controls: Percent CBF change showed no significant effect of eye ($F = 3.4$, $P = 0.7$) or contrast ($F = 3.2$, $P = 0.07$), absolute CBF exhibited no significant effect of eye ($F = 0.01$, $P = 0.9$) or contrast ($F = 0.06$, $P = 0.9$). Absolute CBF change however, exhibited no significant effect of eye ($F = 1.1$, $P = 0.3$) but a main effect of contrast was seen ($F = 9.8$, $P < 0.001$), percent BOLD signal change demonstrated no significant effect of eye ($F = 0.007$, $P = 0.9$) with a main effect of contrast ($F = 34.7$, $P < 0.001$), finally percent gamma power change revealed no significant effect of eye ($F = 0.7$, $P = 0.4$) but a main effect of contrast ($F = 33.2$, $P < 0.001$).

In patients: Percentage CBF change showed no significant difference between eyes ($F = 0.9$, $P = 0.4$) but a main effect of contrast ($F = 3.1$, $P < 0.05$), absolute CBF exhibited no significant difference between eyes ($F = 0.03$, $P = 0.9$), and no significant difference between contrasts ($F = 1.9$, $P = 0.1$).

Absolute CBF change displayed no significant difference between eyes ($F = 1.1$, $P = 0.3$) but a main effect of contrast ($F = 8.8$, $P < 0.001$), similarly percent BOLD signal change had no significant difference between eyes ($F = 1.2$, $P < 0.001$). Finally, percent gamma power change demonstrated no significant difference between eyes ($F = 4.5$, $P = 0.06$) but a significant main effect of contrast ($F = 14.3$, $P < 0.001$).

As there was no significant difference in responses between eyes, all responses were averaged across eyes for all subjects for further analysis.

Figure 8-2 shows full time/frequency responses to the checkerboard in a single representative subject in MEG; healthy volunteer on the top row (A-E) and patient on the bottom row (F-J). Contrasts are shown from left to right (6.25% - 100%). Subject averaged responses are shown in figure 8-3; healthy volunteers on the top row (A-E); patients on the bottom row (F-J).

As in chapter 7 a power law (equation 1) was used to describe the relationship between each modality and checkerboard contrast. This was done using a log-log plot of each modality response against contrast. To determine the contributing factors for each set of responses, multiple regression was performed for each modality, results are summarised in table 8-2. Following this the exponent (m) value were then used to compare responses of each cohort and is summarised in table 8-3. Visualisation of response plots is shown in figure 8-4.

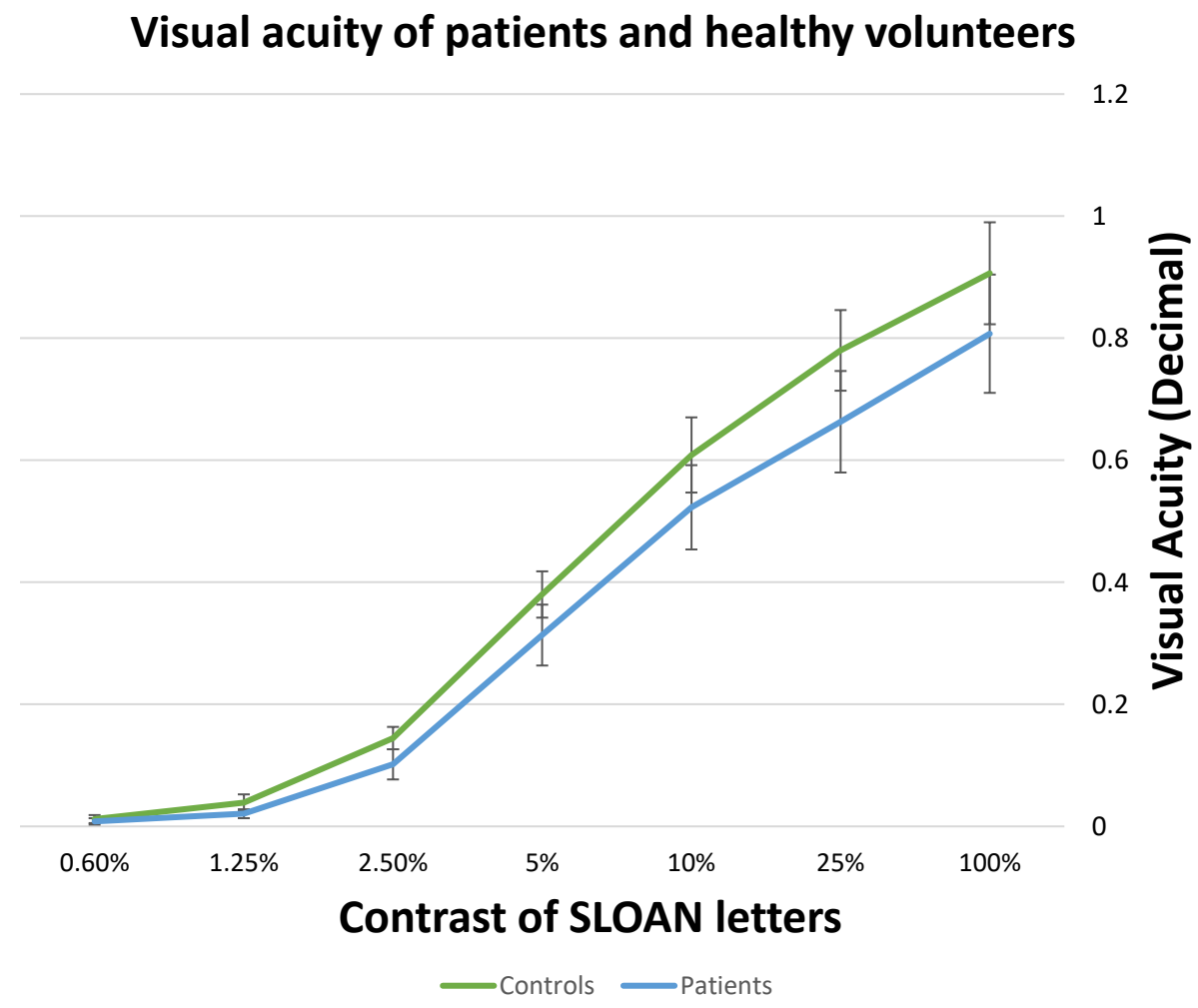

Figure 8-1 Average visual acuity for healthy volunteers (green) and patients (blue). No significant difference between volunteer group was seen (P = 0.98), main effects of age and SLOAN letter contrast significantly contributed to any difference in visual acuity (p <0.05 and p <0.001 respectively).

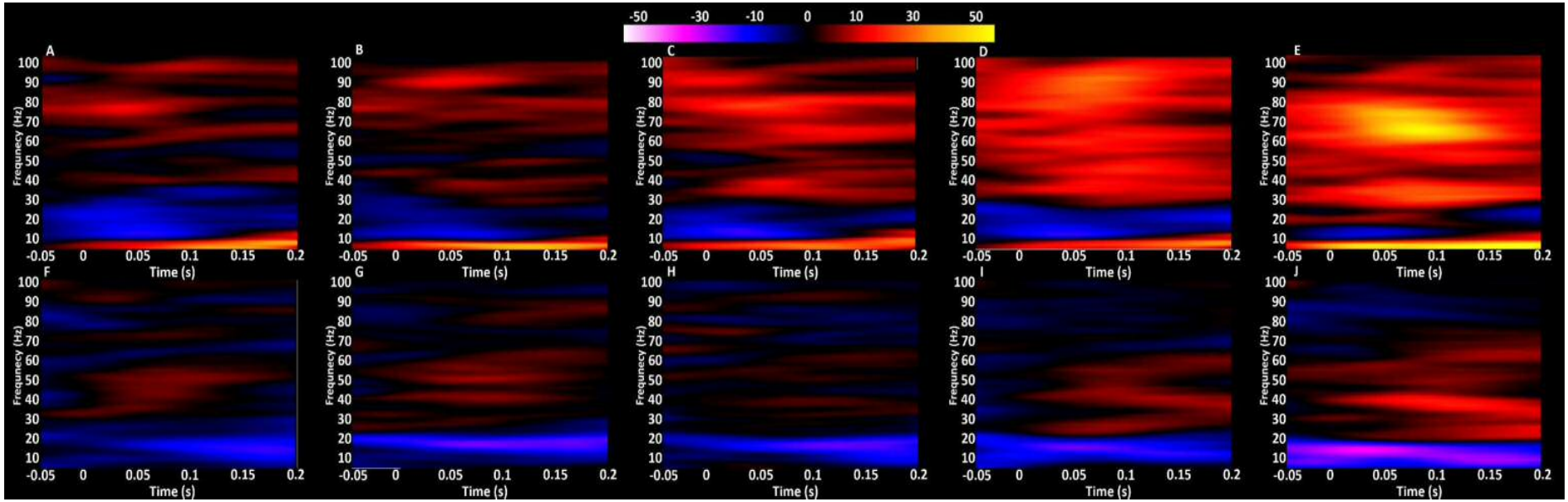

Figure 8-2 Trial- and eye-averaged spectrograms of a representative healthy volunteer (subject 2 A-E top row) and patient (subject 1 F-J bottom row), showing full frequency responses at all checkerboard contrasts: 6.25%, 12.5%, 25%, 50% and 100% (left to right respectively). Images were generated from MEG virtual sensors constructed from peak locations in the visual cortex. As contrast increases there is a marked increase in broad gamma band activity (30-80Hz), along with a desynchronisation in the alpha/beta bands (9-12Hz/12-30Hz). Gamma band activity was markedly higher in the healthy volunteer compared to the patient, all energy values are shown as a percentage change compare to baseline.

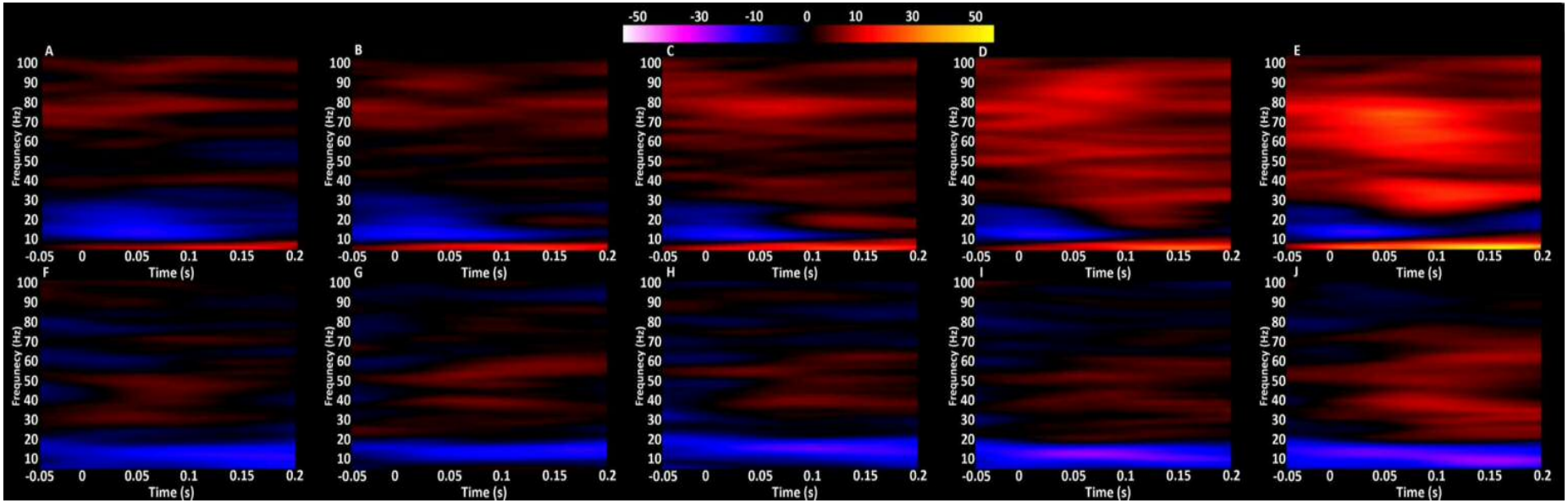

Figure 8-3 Grand averaged spectrograms across contrasts and subjects, healthy volunteers (A-E) and patients (F-J). Contrasts shown increase from left to right (6.25%, 12.5%, 25%, 50% and 100%). As with the spectrograms in figure 2, broadband gamma band power (30-80Hz) increases with contrast with desynchronization in the alpha and beta bands (9-12Hz/12-30Hz). Overall a weaker gamma band response is seen in patients compared to healthy volunteers. All energy values are shown as a percentage change compare to baseline.

	Behavioural characteristics		
	Mean		
	Controls	Patients	P
M/F	2/8	5/8	0.3
Age	40.3±3.3	43.3±2.9	0.5
9HPT	22.4±0.8	25.1±0.9	0.05
PASAT 3	49.1±3	47.5±2.4	0.7
PASAT 2	36.1±2.5	31±1.9	0.1
25FW	9.6±0.2	12.6±1.4	<0.05
Baseline V1 CBF	50.4±3.7	48±2.6	0.3
EDSS		3 (0-4.5)	
P100 Latency (ms)	108±0.003	119±0.003	<0.05
Whole Brain Volume (mm^3)	1,523,327	1,493,231	0.2
Gamma Power at rest	0.95	1.09	0.053

Table 8-1 Behavioural characteristics of each cohort. The only significant difference in behavioural measures between patients and controls was in the 9-hole peg test (9HPT) and 25 ft walk (25FW). Patients were slower to complete the 9HPT than controls 25.1±0.9s and 22.4±0.8s p = 0.05 respectively patients were also slower to complete the 25 ft walk compared to controls 12.6±1.4s and 9.6±0.2s p <0.05 respectively. In addition to this P100 latency of the VEF was longer in patients than controls 19±0.003ms compared to 108±0.003ms p < 0.05 respectively. There was also a trend for resting gamma power to be higher in patients than controls (1.09 and 0.95 respectively) but this did not reach significance p = 0.053. Resting gamma was measured using the same virtual sensor position used when measuring active task responses.

Multiple regression P values					
	Contrast	**Age**	**Baseline CBF**	**Visual Acuity**	**Subject Group**
Percent CBF	<0.001	0.3	<0.001	0.9	0.055
Absolute CBF	<0.001	0.2	<0.001	0.9	<0.001
Absolute CBF change	<0.001	1	<0.05	0.7	0.6
BOLD	<0.001	0.07	0.2	<0.05	0.07
Gamma	<0.001	0.3	<0.05	<0.01	<0.01

Table 8-2 Summary of multiple regression significance for each modality. Percentage CBF change showed a significant dependence on a combination of checkerboard contrast and baseline CBF ($p < 0.001$ or both), with a strong trend for a difference between subject groups ($p = 0.055$). Absolute CBF also exhibited the same dependence on checkerboard contrast and baseline CBF ($p < 0.001$), a significant difference between subject groups was also noted ($p < 0.001$). Absolute CBF change was shown to be influenced heavily by checkerboard contrast ($p < 0.001$) and baseline CBF, but to a lesser extent ($p < 0.05$). Percent BOLD signal change also demonstrated a strong dependence on checkerboard contrast ($p < 0.001$) as well as subject visual acuity ($p < 0.05$). Finally, percent gamma power change was composed of a combination of checkerboard contrast, baseline CBF, visual acuity and subject group ($p < 0.001$, $p < 0.05$ and $p < 0.01$ respectively). Age did not appear to have any significant effect on responses in any modality, but a slight trend was seen in percent BOLD signal change, but did not reach significance

Modality responses vs contrast						
	Mean *M* ± SEM			Mean *K* ± SEM		
Modality	**Controls**	**Patients**	***P***	**Controls**	**Patients**	***P***
Percent Gamma power change	0.917±0.08	0.621±0.12	<0.05	0.84±0.23	0.51±0.13	0.1
Percent CBF change	0.514±0.15	0.34±0.073	0.1	6.2±1.7	8.5±2.2	0.2
Absolute CBF	0.0647±0.007	0.0467±0.009	0.08	51±3.5	48.7±2.4	0.3
Absolute CBF Change	0.605±0.15	0.416±0.08	0.1	3±0.8	3.9±0.96	0.3
Percent BOLD signal change	0.0496±0.036	0.511±0.091	0.4	0.28±0.032	0.24±0.054	0.3

Table 8-3 Summary of exponent (m) values of responses in each modality vs contrast in patients and healthy volunteers along with statistical significance. Only percent change in gamma power n showed any statistical difference between patients and controls (0.34±0.073compared with 0.514±0.15 p <0.05 respectively). There was a distinct trend for absolute CBF to be altered between patients and controls (0.0467±0.009 and 0.0647±0.007 p=0.08 respectively), but did not reach statistical significance. The exponent from the power law model for both absolute and percentage change in CBF showed an interesting trend towards an alteration between patients and controls (absolute CBF change: 0.416±0.08 and 0.605±0.15 respectively, percent CBF change: 0.34±0.073 and 0.514±0.15 respectively. P = 0.1 in both). But no significant difference in the n of percent BOLD signal change with respect to contrast between patients and controls was observed (0.511±0.091 and 0.0496±0.036 p = 0.4).

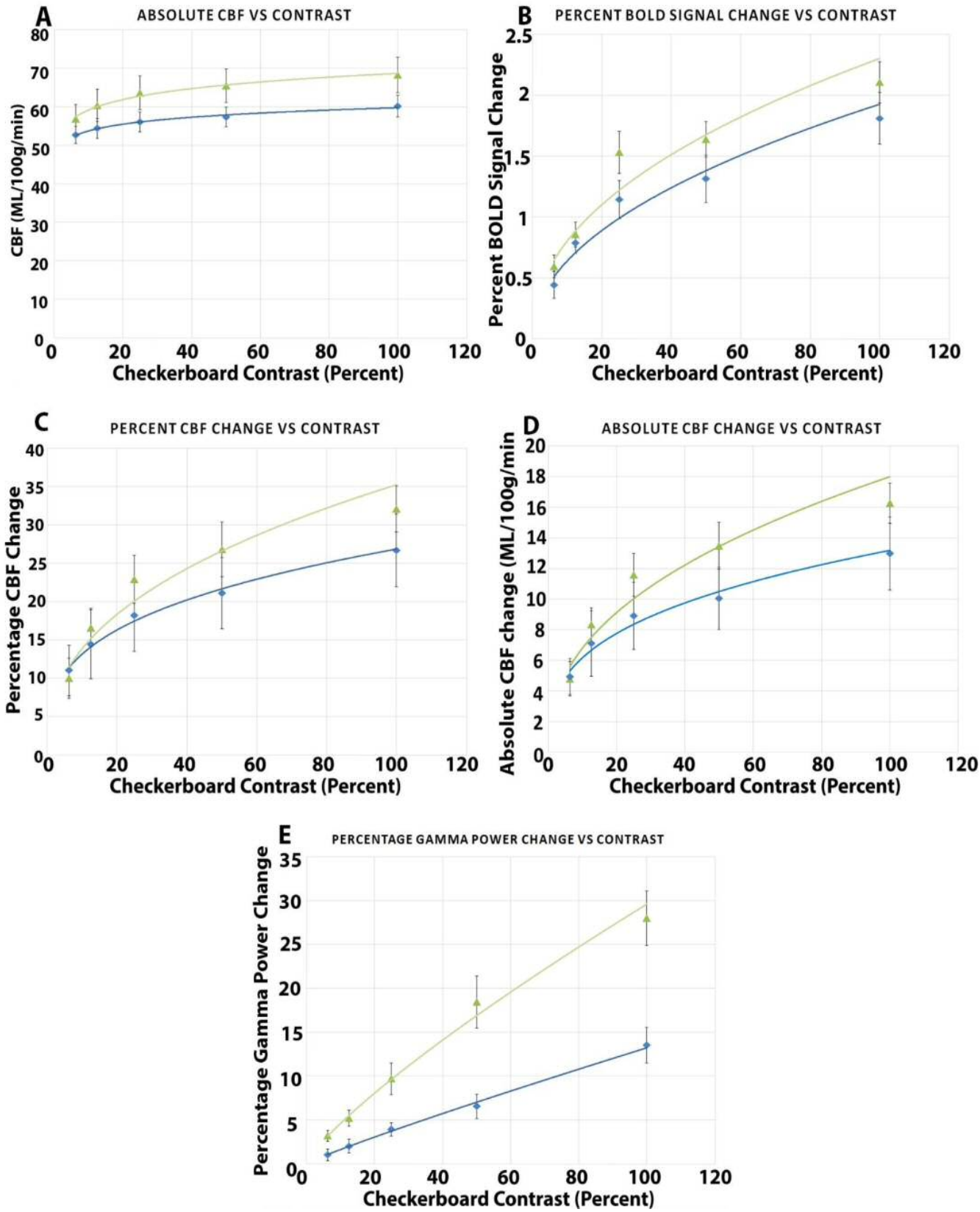

Figure 8-4 Visualisation of responses to a reversing checkerboard at different contrast levels. Controls are shown in green, patients in blue. A power law function was used to describe the relationship between the magnitude of response and contrast level. A) Shows the absolute at each checkerboard contrast used. The exponent (n) of the power law was used as my measure of NVC, there was a non-significant difference between patients and controls. B) Shows the percent BOLD signal change at each checkerboard contrast, there was a non-significant difference between patients and controls. C) Shows the percent CBF change at each checkerboard contrast, there was a non-significant difference between patients and controls. D) Shows the absolute CBF change at each checkerboard contrast, there was a non-significant difference between patients and controls. E) Shows the percent gamma power change at each checkerboard contrast, there was a significantly reduced gamma power increase at each contrast in patients compared to controls ($p < 0.05$).

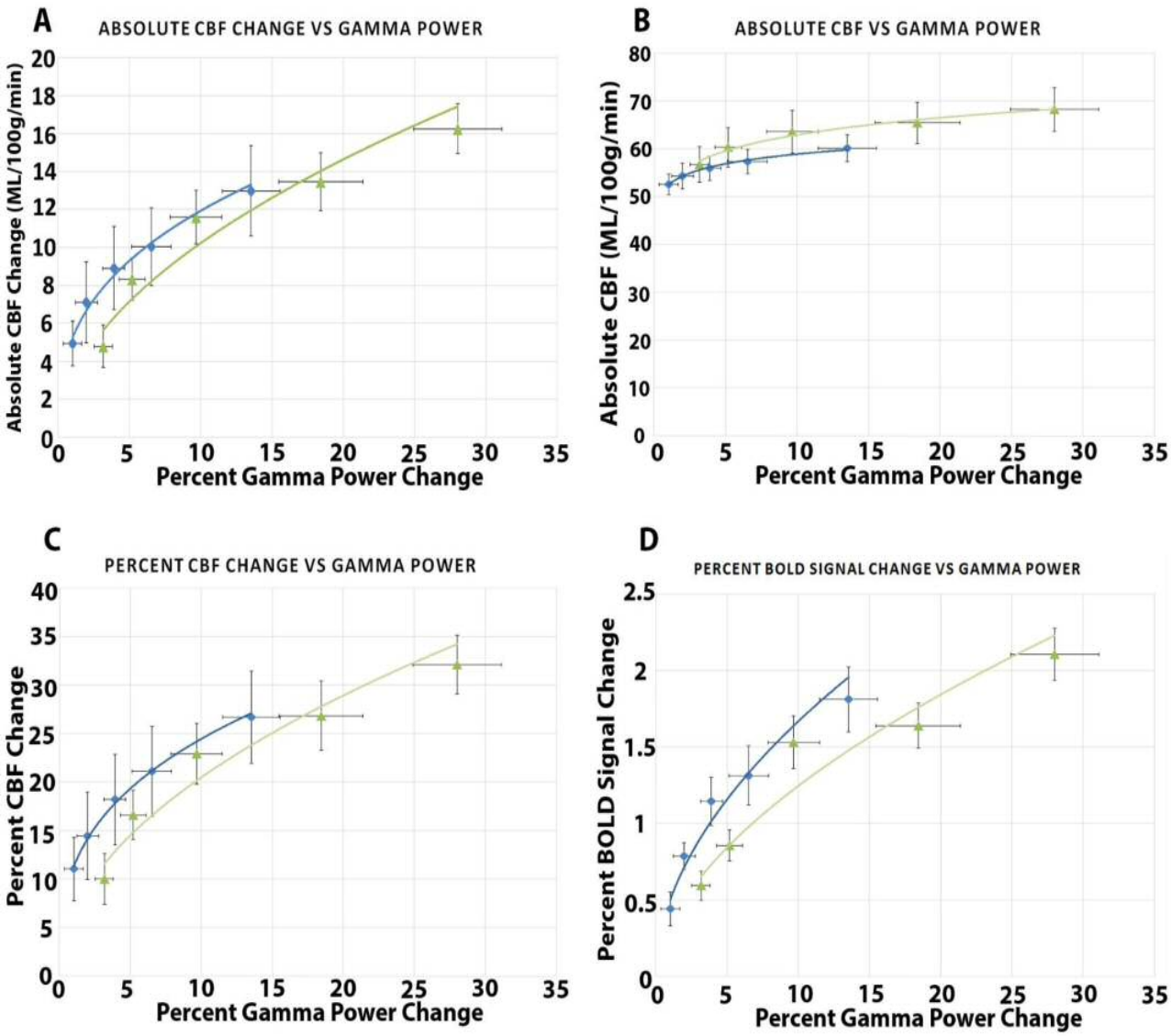

Figure 8-5 Visualisation of NVC in healthy volunteers (green) and patients (blue). All points represent one contrast of the reversing checkerboard. A) Shows power law plots of NVC as measured using percent gamma power change regressed against absolute CBF change in ml/100g/min. There was a strong trend for NVC to be altered in patients compared to controls, but did not quite reach significance (p = 0.1). B) Uses absolute CBF as a blood flow measure for NVC, there was on significant difference between patients and controls (p = 0.2). C) Percent CBF change was used as a blood flow measure in NVC, there was a trend towards a significant difference in NVC between patients and controls (p = 0.1). D) Percent BOLD signal change as a blood flow measure showed the smallest difference in NVC between patients and controls (table 4) and as such was clearly not significant (p = 0.3).

Each blood flow measure was then regressed against Percent gamma power change using the power law function described in equation 2. Visualisation of the resulting NVC measures are shown in figure 8-5, with the exponent (*n*) summarised in table 8-4. T-tests were performed to establish the extent to which any difference between patients and controls could be seen. Both percent CBF change and absolute CBF change showed notable, non-significant trends for an alteration in NVC in patients. Healthy volunteers exhibited an NVC relationship that could be described as:

Compared to patients' coupling:

Absolute CBF showed a slight trend towards a significant alteration in NVC in patients when comparing the two mean exponent values for healthy volunteers and patients respectively:

Finally, BOLD signal-based NVC did not show an obviously significant trend when comparing the exponents of healthy volunteers and patients respectively:

Blood Flow vs Gamma Power						
	Mean *N*			Mean *K*		
Modality	**Controls**	**Patients**	***P***	**Controls**	**Patients**	***P***
Percent CBF	0.61±0.2	0.44±0.1	0.1	8.2±2.4	12.4±2.5	0.1
Absolute CBF	0.081±0.01	0.051±0.01	0.2	53±3.9	51.2±2.5	0.3
Absolute CBF Change	0.8±0.2	0.46±0.1	0.1	3.95±1.1	4.7±1.1	0.2
BOLD	0.55±0.07	0.48±0.1	0.3	0.41±0.06	0.55±0.1	0.07

Table 8-4 Summary of exponent n values used as a measure of NVC in patients and controls. Overall there was no significant difference in NVC measures between the two cohorts, however a strong trend for patients to have a lower NVC than controls when either absolute or percent CBF change as a blood flow measure (p = 0.1). Percent BOLD signal change showed the smallest difference in NVC measures between the two groups when gamma power was regressed against it.

8-5 Discussion

Building on the previous chapter assessing the stability of measures of neurovascular coupling I have attempted to investigate neurovascular coupling can be affected in disease states. There is a trend for neurovascular coupling to be altered in multiple sclerosis but did not reach statistical significance here. It is worth noting that a significant alteration in the gamma band responses to the reversing checkerboard between patients and controls was seen and was the largest response alteration seen in any modality. Absolute CBF change showed a clear trend of being altered in patients compared to controls, but like all other blood flow measures did not quite reach significance. Overall however, responses were generally seen to be lower in patients with MS compared to controls, irrespective of whether they were significantly different from healthy volunteers or not.

One of the leading models for the source of gamma oscillatory power comes from the Pyramidal Interneuron Gamma (PING) network[127,128,187,215]. Here, gamma is modelled by the interaction between inhibitory and excitatory drives, spiking from excitatory neurones is quickly stopped by inhibitory neurones which briefly shut down the network. The re-establishment of this network drives what is seen as gamma oscillations. Stronger excitatory drives – derived from a stronger stimulus for example – cause a faster recovery from these inhibitions resulting in higher oscillatory frequencies and an increase in amplitude[128,187]. In LFP studies spiking activity has been shown to saturate or even decrease at high contrast levels whereas human MEG has had conflicting reports between linear and non-linear increases in gamma power with contrast[127,128,187,208]. This can (at least partially) be explained by the difference in recording methods used, as LFP studies have very small recording sites, any changes in spatial coherence of these signals could results in the apparent saturation or reduction in recording measures. In MEG however, an increase in spatial coherence of gamma oscillations would manifest as an increase in amplitude and is in agreement with the findings here as well as other studies[121,122,185,187]. The decreased gamma responses in patients compared to healthy volunteers for each checkerboard contrast are evidence – along with the increase P100m latency – that even though these patients are still in the early stages of the disease with a low EDSS and only an increased 25 foot-walk (FW) time

there are significant neuronal alterations in these patients. Indeed, P100 latency has long been shown to be lengthened in CIS and very early RRMS patients, even before some lesions can be detected[5,173,174].

The increase in P100m latency in patients compared to controls implies there is damage along the visual pathway in these early stage MS patients, even though this did not result in a significantly altered visual acuity. As increases in gamma power, interpreted under the PING model, rely on an increasing strength of the input (in this case contrast of the visual stimulus). Damage to the visual pathway seen in MS presents as a reduction in visual acuity, and therefore would impact the perceived contrast of the checkerboard. The implication of this is that depending on the severity of damage to the visual pathway, the measure of neurovascular coupling we see here could be restricted as we would not be able to elicit a maximal response from neurons in V1 and therefore would not be able to fully measure the associated haemodynamic response. I attempted to control for differences in visual acuity by using corrective lenses during scan sessions, however, while patients remarked these lenses helped increase their acuity, corrective lenses would not compensate for differences in acuity due to damage along the visual pathway. As no T_2 scans were collected it is not possible to determine the WM damage in these patients, and therefore it isn't possible to determine if the decrease in gamma power seen here is due to a genuine decrease in neuronal activation, or if it is a result of decreased input to V1, but NVC is preserved.

Peak gamma frequency has also been previously used as a measure of neural activity which, along with high temporal stability also alters with stimulus contrast of a visual checkerboard[185,186]. However, any alteration appears to plateau at 40% contrast of a visual grating meaning it would have been unsuitable for use in this study where I am trying to capture as wide a range of neurovascular coupling as possible[187,196]. Indeed, as I have already assessed the stability and usefulness of using gamma power in measuring neurovascular coupling in chapter 7, as this study yielded some good properties in measuring neurovascular coupling, the same protocol was used here in patients.

Gamma oscillatory power and BOLD responses have been previously shown to be decoupled under certain stimulatory circumstances [122,135]. Here it seems that a similar decoupling between gamma power and BOLD signal changes can be seen in patients with MS. Due to the complicated nature of the BOLD signal this is not entirely unexpected as many other factors could be confounding the coupling between BOLD signal change and gamma power (such as $CMRO_2$ and CBV alterations), particularly in a pathological state such as MS. However, there was a non-significant trend towards a lower absolute change in CBF for each stimulus contrast in patients compared to healthy volunteers. The extent of this was not quite as large as the change in gamma power and, also implies some degree of decoupling between the two measurements.

We have previously mentioned the interference of nitric oxide synthase (NOS) activity in chapter 5 in inflammatory active patients. Higher levels of circulating endothelin-1 (ET-1) would be acting to supress endothelial NOS (eNOS) activity[93,148]. Due to the close relationship between neurons, astrocytes and vascular smooth muscle cells it would be reasonable to infer that neural activity plays a key role in helping to regulate resting vascular tone. This could provide an explanation for the higher resting gamma power seen in patients compared to healthy volunteers. Increased oscillatory activity of the PING network could be indicative of extra neuronal signalling. It is possible this extra neuronal activity is due to damage along the visual pathway, with extra processing being required by the visual cortex to compensate for alterations in visual acuity. The higher resting gamma power, signalling for dilation of vascular smooth muscle cells, may be why no cerebral hypoperfusion was seen in these patients, contradictory to many other studies[48,150,209]. Indeed, as these patients were still early on in their disease course, any decreases in gamma power could be indicative of early damage, as gamma power has been shown to negatively correlate with cortical thickness and therefore cell count[125].

As with many neuroimaging studies the current study here also indicates a similar problem. While the exponent of many of the blood flow-based measurements and NVC in patients were almost half the value of what was seen in healthy controls along with low standard error significance was still not

reached. When comparing two populations a larger sample size would have been desirable. However, due to the time constraints placed on this study, along with the selective enrolment criteria this was not possible. Given that these patients were still in the early stages of their disease, later stage patients could have produced much large difference in NVC than the ones seen in the present study. However, with more advanced patients comes the additional confound. Different therapies and drugs to manage both the disease and symptoms, many of which being psychoactive would cause further complications to assessing if, and how NVC could be affected in this pathological state. Patients who are prescribed DMTs tend to be further along in their disease course, and therefore would have suffered further damage to their visual system, resulting in a greater impairment to their electrophysiological responses.

In conclusion, I attempted to use the methods laid out in chapter 7 to establish whether there was an alteration in neurovascular coupling in patients with multiple sclerosis, given their altered CVR. While a significant decrease in gamma power in response to the reversing checkerboard was seen in patients compared to healthy volunteers, no significant alterations in blood flow were noted. Due to the haemodynamic response being relatively unaltered in MS patients despite the decrease in gamma power implies there was a stronger blood flow response in patients for a given increase in gamma power. However, as there is also no way to separate out whether the decreases in gamma power are due to damage along the visual pathway, decreased neuronal activation, or a combination of the two, it is difficult to definitively assess whether neurovascular coupling is altered or preserved in these early stage MS patients.

Chapter 9: General Discussion

9-1 Summary of findings

Data collected from the Sapienza institute in Rome and analysed in this thesis, investigating the effects multiple sclerosis has on cerebrovascular reactivity and the role treatment plays in its restoration, was used as a prelude to inform the direction future research should take into the possibility of establishing a non-invasive method for measuring neurovascular coupling. This was developed using a multi-modal MEG/fMRI approach to gain an understanding for the role high frequency oscillatory activity (interpreted under the PING model) plays in altering blood flow, and how multiple sclerosis can alter this essential dynamic.

The first experiment found in chapter 5 using data gathered from the Sapienza institute in Rome, found a wide difference in the vascular reactivity of early RRMS patients in response to CO_2 depending on whether the patients were undergoing acute inflammation. Patients who did not exhibit any indications of being acutely inflamed demonstrated a significantly decreased cerebrovascular reactivity compared to healthy volunteers and patients who were acutely inflamed. This effect was reversed following commencement of treatment with the disease modifying drug interferon-β1a (IFN-β1a).

Based on these results, a pilot study was performed using a neuronal stimulus to elicit a blood flow response. I am interested in blood flow changes in response to a neuronal stimulus as CO_2 only tests the ability of vessels to dilate, rather than full NVC. Using MEG and fMRI to measure neuronal responses and blood flow changes respectively, a graded visual paradigm was designed to modulate the strength of the response measured. Two visual tasks were shown, designed to obtain two different neuronal responses; a checkerboard was used to gather visual evoked field (VEF) responses, a classical measure used clinically to assess neuronal damage along the visual pathway, and a moving grating to elicit sustained gamma band oscillatory activity. In chapter 6 I noted the checkerboard appeared to produce the most consistent results when measuring VEF amplitude and percent BOLD signal/CBF change. The grating paradigm resulted in a high degree of variability between participants and was

deemed unsuitable to be used to measure neurovascular coupling (NVC). The likely reason for this is the design of the stimulus; compared to the reversing checkerboard which allowed for a continuous 30s block at each contrast, the grating was shown in a 1s on/off design. This means that for each 30s block, the grating was only shown for 15s, and making the stimulus too weak to elicit a strong, stable response.

This protocol was refined further in chapter 7, where the repeatability of each neuronal and blood flow measure was assessed. As I established in chapter 6, that a checkerboard task appeared to be the most appropriate stimulus for gaining stable neuronal and blood flow response. This task was repeated, but was altered to utilise a wider range of stimulus strengths to characterise the full spread of the NVC relationship. Using a power law function to characterise the relationship between stimulus strength (in this case percentage contrast of the checkerboard) and response strength, gamma oscillatory power was found to be highly stable over time, as was absolute CBF change and percent BOLD signal change in relation to stimulus strength. VEF amplitude however, was found to be less stable, with a high variability between time points.

With the protocol established I aimed to finally build on the results from chapter 5, and further investigate the NVC relationship in multiple sclerosis. Gamma power was found to be significantly depressed at each contrast of the visual stimulus compared to healthy volunteers, but no corresponding decrease in CBF was noted. Using the same power law function utilised in chapter 7 I demonstrated a strong trend for a decoupling between gamma power and absolute CBF change in multiple sclerosis patients compared to healthy volunteers, but this did not reach significance.

9-2 Interpretation and future research

9-2-1 Decreased cerebrovascular reactivity (CVR) in multiple sclerosis

Previous studies have demonstrated chronic hypoperfusion in both normal appearing white matter (NAWM) and grey matter (GM) in MS patients[34,46–48]. Disruptions in normal blood flow at rest could result in long term low level hypoxia to neurons, which would be extremely damaging as it puts

considerable strain on mitochondria to produce enough ATP to maintain proper resting membrane potentials. The production of endothelin-1 (ET-1) has been implicated in overcoming the normal regulation of luminal diameter[51,214], causing the vasoconstriction and associated reduction in blood flow in MS patients. Loss of normal vascular reactivity in response to a vasoactive stimulus, broadly in line with previous work using 5% hypercapnia[145,216], implies there is a greater level of interference from the constant presence of pro-inflammatory cytokines or vasoconstrictive mediators. It is interesting to note that patients exhibiting signs of acute inflammation also had a higher vascular reactivity than those who were not acutely inflamed. This would be possible due to the higher levels cytokines such as TNF-α,IFN-γ and IL-6, all of which cause increases in inducible nitric oxide synthase (iNOS) activity and would therefore allow for an increase in vascular reactivity, as iNOS would not be activated in non-inflamed patients. The administration of IFN-β, while reducing pro-inflammatory cytokine activity, also greatly reduces the level of ET-1 production and helps to explain the normalisation of CVR following the commencement of treatment.

These interpretations are somewhat speculative, however, as no biological samples were taken from patients during this study. It is, therefore, impossible to confirm the presence of these biomarkers. Instead I have had to rely on the literature for possible explanations to the differences in in CVR in these subsets of patients, and why both groups appear to have their vascular reactivity restored following administration of a DMT such as IFN-β.

9-2-2 Increased inter-subject variability using a moving grating stimulus.

When first attempting to establish a measure for NVC using the protocol outlined in chapter 6, it was noted there was a high level of variability between subject responses using a moving grating compared to the reversing checkerboard. Originally this was thought to be an issue with the gamma power measure being unreliable. However, the results persisted in the blood flow measurements, which also showed a higher level of variability compared the same contrasts in the checkerboard, along with a lower average response.

As this was an attempt to replicate the work of Muthukumaraswamy (2009). In this study Muthukumaraswamy et al. used a square wave grating to elicit gamma band oscillations. The visual task was presented at two contrast levels (30% and 100%) and presented in a similar on/off pattern, 5s on 10s off in both contrasts. However, as I was testing a larger range of contrasts (40%, 55%, 70%, 85% and 100%) the protocol was altered to a 1s on/off pattern but presenting each contrast in 30s blocks.

The lower blood flow response could be due to the relatively transient nature of the design protocol. As each grating was only presented for 1s before moving to a 0% contrast block for 1s does not give the haemodynamic response (HR) sufficient time to increase to the same level as the checkerboard would, as each contrast was presented continuously for 30s. Instead as the HR requires around 5s to reach its peak this would explain the relatively flat regression slope show in fig. 6-6D, as well as the high inter-subject variability.

Muthukumaraswamy (2010) et al. noted that induced gamma power had a high level of inter-subject variability compared to evoked responses. This would help to explain the high variability seen between subjects and the large SEM in fig. 6-6C compared to VEF amplitudes. Indeed, Muthukumaraswamy went on to show evoked gamma oscillatory power to be highly stable over time and between subjects, and lead to the refinements to the protocol seen in chapter 7.

9-2-3 Repeatability of NVC and compromises in the protocol

We were able to demonstrate, in line with other studies, that evoked responses exhibited the smallest amount of inter-subject variability. This was used to refine the protocol when looking to establish the repeatability of each neuronal response. To that end the checkerboard was used as the only visual stimulus in chapter 7. However, it was possible that differences in visual acuity might affect both neuronal and blood flow responses as a lower visual acuity would have the effect of reducing the perceived contrast of any stimulus. To account for this possible confound the visual acuity of each eye was assessed prior to the commencement of each scan session. During both MRI and MEG scans the

responses from each eye were measured separately. Averaging of responses between eyes was only done when it was established there was no significant difference in acuity between eyes. In addition to this, the contrast range was also increased to cover a wider range of stimulus responses. Previous studies had shown that VEF amplitudes and percent BOLD signal changes plateau at high contrasts meaning the only way to get a full representation of NVC was to use a range of contrasts from 0%-100%.

Evoked gamma oscillatory power has also been shown to have a low inter-subject variability[185], so here I aimed to alter the protocol that would allow the measurement of VEF amplitudes, gamma oscillatory power, percent BOLD signal change and absolute CBF change in the respective scan sessions. For this reason, a checkerboard of 2Hz and 1 cycle per degree of visual angle (cpd) was selected. In an fMRI setting a reversal rate of 8Hz and a high cpd has been shown to be the most effective at eliciting a maximal CBF response[217]. This is in contrast to MEG studies, which have shown that for checkerboard stimuli, a low reversal rate of 0.5-1Hz and low cpd prove to be the most effective (and most commonly seen in the literature) of evoking a maximal response[128,218,219]. Indeed, as the aim in this study was to measure evoked field amplitude and evoked gamma oscillatory spikes, the former of which has been shown to require 200ms to complete – or longer in the case of MS patients – a maximal reversal rate of 2Hz was set. A similar compromise had to be reached regarding the spatial frequency of the checkerboard. Fortunately, it has previously been shown that the BOLD response is less sensitive to the spatial frequency of a visual stimulus than either VEF amplitudes or gamma power is[122]. Spatial frequency was therefore maintained at 1cpd, to gain the largest neuronal response – particularly as these measurements have a lower signal to noise ratios (SNR) compared to blood flow measurements in MRI.

A different compromise could have been reached in regards to this protocol. Steady state VEFs amplitudes and phase (the latter being comparable to latency in transient VEFs) could have been utilised instead[184,220,221]. This would have allowed for a higher reversal rate of the checkerboard

allowing for maximal blood flow responses and still gathering a measure of neuronal activity. The higher reversal rate would prevent the measurement of evoked gamma oscillatory power, and instead the responses would be more akin to induced gamma responses, something that had already been shown to have a high inter-subject variability. I have already shown a proof of concept with the NVC measure in chapter 6 using a low spatial frequency/low reversal rate stimulus. Having two neuronal measures would also offer more options in case a low repeatability score was found in any of the individual measures. As time was critical I concluded that for these reasons it would be best to stay with the measures I had already identified and tested.

Intraclass correlation coefficient 3,1 (ICC 3,1) was used to assess the repeatability of each response, as well as the repeatability of each NVC measure – defined as the exponent value of a power law function between neuronal and blood flow responses. Contradicting previous reports, I found transient VEF (T-VEF) amplitudes to have an ICC value close to 0: indicating low repeatability between measurements[115]. Evoked gamma oscillatory power, however, proved to be highly stable with an ICC value of 0.9.

The low repeatability seen here is likely to be due to the design of the checkerboard protocol. As each reversal succeeded another, there was no opportunity to establish a resting baseline period with which to compare individual evoked responses prior to averaging. This meant that the baseline of each T-VEF was a small 400ms window between the end of one T-VEF and the start of the next. During this time, neuronal responses would still be resetting, therefore could provide an unstable baseline with which to measure the new T-VEF amplitude. This is would be particularly noticeable if a subject had a higher T-VEF latency which could result in part of the N145m wave being captured in the baselining window. It would have been ideal to have a boxcar design whereby each checkerboard reversal was preceded by a blank 0% contrast screen. Due to the time constraints imposed using such a wide range of contrasts, 30s of active checkerboard being needed to be repeated 4 times to allow for a high enough SNR in an fMRI setting and subject tolerances of the stimulus I was forced to

compromise and calculate VEF amplitude in this way. As gamma oscillatory power was baselined according to the 30s rest blocks interspersed throughout the protocol, a more stable baselining would have been likely to occur. Due to these factors it is a likely explanation for the differences in results shown here compared to the literature.

As both BOLD signal changes and absolute CBF were found to have a significant, positive ICC value, both measures were brought forward to the final protocol to be used in patients. As a dual echo MRI sequence was being used to capture these two responses simultaneously, there was little time penalty associated with collecting both contrasts with this method. However, it is known that the ASL techniques have an inherently lower SNR compared to BOLD signal and could be at least partially responsible for the lower ICC value seen in chapter 7. my results here are similar to what has been concluded by other studies.

Regressing blood flow responses against neuronal measures using the power law function mentioned previously yielded a stable NVC measure when using evoked gamma oscillatory power. This stability was found to occur even when the order of the scans was swapped (session 2 neuronal responses against session 1 blood flow changes and vice versa). This held true with both BOLD and absolute CBF. As T-VEF amplitude were found to be too variable over time, a NVC measure based on this neuronal response was found exhibit the same low ICC value as VEF amplitude on its own when regressed against visual stimulus contrast.

9-2-4 Neurovascular coupling in MS

The final study, to investigate how NVC is affected in patients with early MS prior to DMT commencement demonstrated a significantly reduced gamma band response compared to healthy volunteers. While there was a strong trend for absolute CBF change to be reduced compared to healthy volunteers it did not quite reach significance ($p = 0.08$). Similarly, coupling between gamma power and absolute CBF change showed a strong trend for NVC in patients almost half of that of age and sex matched healthy volunteers, with no significant alteration in baseline perfusion.

However, what does appear to be clear is that even MS patients at such as early stage (mean EDSS 3) in their disease course are already showing profound alterations in NVC compared to healthy controls. This is generally in line with similar research into visual responses in MS patients[172,174,222,223]. Patients tend to exhibit lower blood flow response for each contrast compared to healthy volunteers, as well as a longer latency and lower VEF/VEP amplitudes[222,224].

9-2-5 Our approach to measuring neurovascular coupling

Our aim was to develop a protocol for defining and measuring neurovascular coupling in humans via non-invasive means. I chose to focus on the visual system as it has the advantages of being one of the most extensively studied regions of both human and non-human brains, with responses that are easily measured, and have a wide supporting literature base with which to easily design the type of protocol that would allow for the measurement of a graded neuronal and haemodynamic response. As the aim of this thesis was to further extend the method for testing neurovascular coupling in an inflamed brain, using the visual system had the added advantage that similar visual tasks are used clinically to assess disease progression and damage, thereby allowing for a comparison of experimental results shown here and clinically accepted patient responses.

Using a non-invasive method was also crucial. Unlike some notable severe epilepsy studies where patients undergo placement of electrocorticography nets (ECOG) during pre-planned surgery to pinpoint the locations of seizure activity, multiple sclerosis patients, or many neurodegenerative patients do not have such dangerous, highly invasive, expensive surgeries occurring during their treatment. Indeed, proposing such surgeries to allow for direct measurement of neural activity would be irresponsible, and the proposed benefits (of which none would be immediately available or clear) would be negligible. Similarly, catheterisation of an artery close to the region of interest to get an absolute, continuous measure of blood flow would represent a highly risky proposition for any subject thinking about participating in a study, especially it is not required for treatment. Finally, the use of non-invasive methods for measuring neurovascular coupling means that there are far fewer ethical

implications when proposing new studies, along with any subject group (patient or healthy volunteer) being easier to recruit than if highly invasive methods were used.

However, the use of non-invasive recordings does have its drawbacks, particularly when attempting to measure neural activity. Namely I do not have the certainty that the gamma power changes measured do in fact relate to the LFP and individual firing patterns found in invasive animal studies[127,225]. Several mathematical models have been proposed that attempt to explain the physiology behind the gamma oscillatory signal, but without invasive recordings I cannot be certain that any signals measured here can be compared directly to animal studies[127,128,138,142,226].

With additional time, it would have been preferable to obtain a larger cohort of MS patients to determine if the trend for altered NVC in patients would reach statistical significance. However, the exclusion criteria were extremely restrictive as it is critical for patients to begin disease modifying treatments as soon as they become eligible, meaning only a small window of opportunity was present to allow for recruitment of participants. As in the first study into CVR in MS patients, having the opportunity to investigate the effects of IFN-β treatment on this alteration in NVC would be extremely informative as to finding if, like CVR, the likely alteration in NVC is reversible with treatment. If so, the measure of NVC used here would be a potential marker for assessing the effects of new treatments, as well as exploring NVC in other diseases of the CNS.

Appendix A

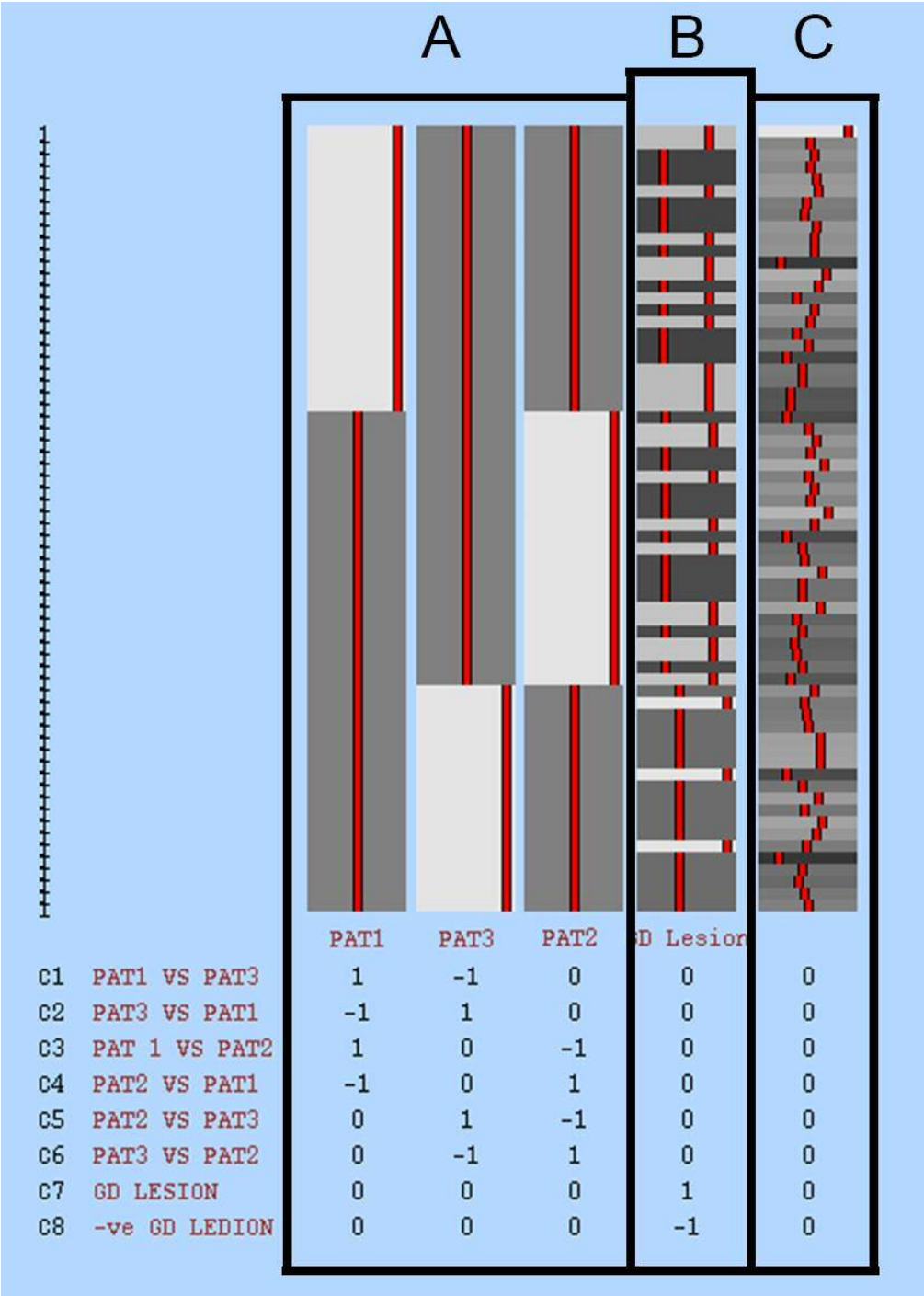

Design matrix of group level patient GLM. Box A contains the averaging model for patients at time point 1, 3, and 2 (left to right). Box B contains a model for whether a patient exhibited acute inflammation, determined by the presence of gadolinium enhancing lesions. Box C contains the model for whole brain grey matter densities as determined from FAST segmentation as part of FSL VBM.

References

1. Compston, A. & Coles, A. Multiple sclerosis. *Lancet* **372,** 1502–1517 (2008).
2. Dutta, R. & Trapp, B. D. Relapsing and progressive forms of multiple sclerosis – insights from pathology. *Curr. Opin. Neurol.* **27,** 271–278 (2014).
3. Reipert, B. Multiple sclerosis: a short review of the disease and its differences between men and women. *J. Men's Heal. Gend.* **1,** 334–340 (2004).
4. Geurts, J. J. G. & Barkhof, F. Grey matter pathology in multiple sclerosis. *Lancet Neurol.* **7,** 841–51 (2008).
5. Filippi, M. & Agosta, F. Imaging Biomarkers in Multiple Sclerosis. **788,** 770–788 (2010).
6. Redford, E. J., Kapoor, R. & Smith, K. J. Nitric oxide donors reversibly block axonal conduction : demyelinated axons are especially susceptible. *Brain* **1,** 2149–2157 (1997).
7. Patejdl, R., Penner, I. K., Noack, T. K. & Zettl, U. K. Multiple sclerosis and fatigue: A review on the contribution of inflammation and immune-mediated neurodegeneration. *Autoimmun. Rev.* **15,** 210–220 (2016).
8. Centonze, D. *et al.* The link between inflammation, synaptic transmission and neurodegeneration in multiple sclerosis. *Cell Death Differ.* **17,** 1083–91 (2010).
9. Stadelmann, C., Wegner, C. & Brück, W. Inflammation, demyelination, and degeneration - recent insights from MS pathology. *Biochim. Biophys. Acta* **1812,** 275–82 (2011).
10. Wuerfel, J., Paul, F. & Zipp, F. Cerebral blood perfusion changes in multiple sclerosis. *J. Neurol. Sci.* **259,** 16–20 (2007).
11. Farkas, E. *et al.* Tumor necrosis factor-alpha increases cerebral blood flow and ultrastructural capillary damage through the release of nitric oxide in the rat brain. *Microvasc. Res.* **72,** 113–119 (2006).
12. Minagar, A. & Alexander, J. S. Blood-brain barrier disruption in multiple sclerosis. *Mult. Scler.* **9,** 540–549 (2003).
13. Katsavos, S. & Anagnostouli, M. Biomarkers in Multiple Sclerosis: An Up-to-Date Overview. *Mult. Scler. Int.* **2013,** 340508 (2013).
14. Koriem, K. M. M. Multiple sclerosis: New insights and trends. *Asian Pac. J. Trop. Biomed.* **6,** 429–440 (2016).
15. Polman, C. H. *et al.* Diagnostic criteria for multiple sclerosis: 2010 Revisions to the McDonald criteria. *Ann. Neurol.* **69,** 292–302 (2011).
16. Alroughani, R., Al Hashel, J., Lamdhade, S. & Ahmed, S. F. Predictors of Conversion to Multiple Sclerosis in Patients with Clinical Isolated Syndrome Using the 2010 Revised McDonald Criteria. *ISRN Neurol.* **2012,** 1–6 (2012).
17. Marcus, J. F. & Waubant, E. L. Updates on Clinically Isolated Syndrome and Diagnostic Criteria for Multiple Sclerosis. *The Neurohospitalist* **3,** 65–80 (2012).
18. Lublin, F. D. *et al.* Defining the clinical course of multiple sclerosis The 2013 revisions. (2014).
19. Jenkins, T. M. *et al.* Neuroplasticity predicts outcome of optic neuritis independent of tissue damage. *Ann. Neurol.* **67,** 99–113 (2010).
20. Penner, I., Kappos, L., Rausch, M., Opwis, K. & Radu, E. W. Therapy-induced plasticity of

cognitive functions in MS patients : Insights from fMRI. **99,** 455–462 (2006).

21. Bates, D. Treatment effects of immunomodulatory therapies at different stages of multiple sclerosis in short-term trials. *Neurol.* **76,** S14–S25 (2011).

22. Polman, C. H. *et al.* Diagnostic criteria for multiple sclerosis: 2005 Revisions to the 'McDonald Criteria'. *Annals of Neurology* **58,** 840–846 (2005).

23. Ebers, G. C. *et al.* A population-based study of multiple sclerosis in twins. *N. Engl. J. Med.* **315,** 1638–42 (1986).

24. Winquist, R. J., Kwong, A., Ramachandran, R. & Jain, J. The complex etiology of multiple sclerosis. *Biochem. Pharmacol.* **74,** 1321–9 (2007).

25. van Walderveen, M. A. A. *et al.* Histopathologic correlate of hypointense lesions on T1-weighted spin-echo MRI in multiple sclerosis. *Neurol.* **50,** 1282–1288 (1998).

26. Jacobs, L. D. *et al.* Intramuscular Interferon Beta-1A Therapy Initiated during a First Demyelinating Event in Multiple Sclerosis. *N. Engl. J. Med.* **343,** 898–904 (2000).

27. Liu, J. S., Zhao, M. L., Brosnan, C. F. & Lee, S. C. Expression of inducible nitric oxide synthase and nitrotyrosine in multiple sclerosis lesions. *Am. J. Pathol.* **158,** 2057–66 (2001).

28. Szatmári, S. *et al.* Impaired cerebrovascular reactivity in sepsis-associated encephalopathy studied by acetazolamide test. *Crit. Care* **14,** R50 (2010).

29. Kemp, K. *et al.* Oxidative injury in multiple sclerosis cerebellar grey matter. *Brain Res.* **1642,** 452–460 (2016).

30. Pacher, P., Beckman, J. S. & Liaudet, L. Nitric oxide and peroxynitrite in health and disease. *Physiol. Rev.* **87,** 315–424 (2007).

31. Peng, L., Zhang, X. & Hertz, L. High extracellular potassium concentrations stimulate oxidative metabolism in a glutamatergic neuronal culture and glycolysis in cultured astrocytes but have no stimulatory effect in a GABAergic neuronal culture. *Brain Res.* **663,** 168–172 (1994).

32. Bear, M. F., Connors, B. W. & Paradiso, M. A. in *Neruoscience: Discovering the Brain* 75–100 (Lippincott Williams & Wilkins, 2006).

33. Craner, M. J. *et al.* Molecular changes in neurons in multiple sclerosis: altered axonal expression of Nav1.2 and Nav1.6 sodium channels and Na+/Ca2+ exchanger. *Proc. Natl. Acad. Sci. U. S. A.* **101,** 8168–73 (2004).

34. Trapp, B. D. & Stys, P. K. Virtual hypoxia and chronic necrosis of demyelinated axons in multiple sclerosis. *Lancet Neurol.* **8,** 280–91 (2009).

35. Black, J. a, Newcombe, J., Trapp, B. D. & Waxman, S. G. Sodium channel expression within chronic multiple sclerosis plaques. *J. Neuropathol. Exp. Neurol.* **66,** 828–37 (2007).

36. Cambron, M. *et al.* White-matter astrocytes, axonal energy metabolism, and axonal degeneration in multiple sclerosis. *J. Cereb. Blood Flow Metab.* **32,** 413–24 (2012).

37. Su, K. G., Banker, G., Bourdette, D. & Forte, M. Axonal degeneration in multiple sclerosis: The mitochondrial hypothesis. *Curr Neurol Neurosci* **9,** 411–417 (2009).

38. Witte, M. E., Mahad, D. J., Lassmann, H. & van Horssen, J. Mitochondrial dysfunction contributes to neurodegeneration in multiple sclerosis. *Trends Mol. Med.* **20,** 179–87 (2014).

39. Lansley, J., Mataix-Cols, D., Grau, M., Radua, J. & Sastre-Garriga, J. Localized grey matter

atrophy in multiple sclerosis: A meta-analysis of voxel-based morphometry studies and associations with functional disability. *Neurosci. Biobehav. Rev.* **37,** 819–30 (2013).

40. Chard, D. & Miller, D. Grey matter pathology in clinically early multiple sclerosis: evidence from magnetic resonance imaging. *J. Neurol. Sci.* **282,** 5–11 (2009).

41. Haider, L. *et al.* The topograpy of demyelination and neurodegeneration in the multiple sclerosis brain. *Brain* **139,** 807–815 (2016).

42. Davies, A. L. *et al.* Neurological deficits caused by tissue hypoxia in neuroinflammatory disease. *Ann. Neurol.* **74,** 815–825 (2013).

43. Holland, C. M. *et al.* The Relationship between Normal Cerebral Perfusion Patterns and White Matter Lesion Distribution in 1,249 Patients with Multiple Sclerosis. *J. Neuroimaging* **22,** 129–136 (2012).

44. Aboul-Enein, F. *et al.* Preferential loss of myelin-associated glycoprotein reflects hypoxia-like white matter damage in stroke and inflammatory brain diseases. *J. Neuropathol. Exp. Neurol.* **62,** 25–33 (2003).

45. Fischer, M. T. *et al.* Disease-specific molecular events in cortical multiple sclerosis lesions. *Brain* **136,** 1799–1815 (2013).

46. Juurlink, B. H. J. The evidence for hypoperfusion as a factor in multiple sclerosis lesion development. *Mult. Scler. Int.* **2013,** 598093 (2013).

47. D'Haeseleer, M. *et al.* Cerebral hypoperfusion in multiple sclerosis is reversible and mediated by endothelin-1. *PNAS* **110,** 5654–5658 (2013).

48. De Keyser, J., Steen, C., Mostert, J. P. & Koch, M. W. Hypoperfusion of the cerebral white matter in multiple sclerosis: possible mechanisms and pathophysiological significance. *J. Cereb. Blood Flow Metab.* **28,** 1645–51 (2008).

49. Rashid, W. *et al.* Abnormalities of cerebral perfusion in multiple sclerosis. *J. Neurol. Neurosurg. Psychiatry* **75,** 1288–93 (2004).

50. Donato, O. Di *et al.* Multiple Sclerosis : Cerebral Circulation Time. *Radiology* **262,** 947–955 (2012).

51. Farco, G. *et al.* Circulating endothelin-1 alters critical mechanisms regulating the cerebral microcirculation. *Hypertension* **62,** 1–18 (2014).

52. Andresen, J., Shafi, N. I. & Bryan, R. M. Endothelial influences on cerebrovascular tone. *J. Appl. Physiol.* **100,** 318–327 (2006).

53. Smith, K. J. & Lassmann, H. The role of nitric oxide in multiple sclerosis. *Lancet Neurol.* **1,** 232–41 (2002).

54. Calabrese, V. *et al.* Nitric oxide synthase is present in the cerebrospinal fluid of patients with active multiple sclerosis and is associated with increases in cerebrospinal fluid protein nitrotyrosine and S-nitrosothiols and with changes in glutathione levels. *J. Neurosci. Res.* **70,** 580–7 (2002).

55. Morikawa, A. *et al.* Augmentation of Nitric Oxide Production by Gamma Interferon in a Mouse Vascular Endothelial Cell Line and Its Modulation by Tumor Necrosis Factor Alpha and Lipopolysaccharide. *Infect. Immun.* **68,** 6209–6214 (2000).

56. Muñoz-Fernández, M. a & Fresno, M. The role of tumour necrosis factor, interleukin 6,

interferon-gamma and inducible nitric oxide synthase in the development and pathology of the nervous system. *Prog. Neurobiol.* **56,** 307–40 (1998).

57. Peruzzo, D. *et al.* Heterogeneity of cortical lesions in multiple sclerosis: an MRI perfusion study. *J. Cereb. Blood Flow Metab.* **33,** 457–63 (2013).

58. Acar, G. *et al.* Nitric oxide as an activity marker in multiple sclerosis. *J. Neurol.* **250,** 588–92 (2003).

59. Stewart, V. C. *et al.* Pretreatment of Astrocytes with Interferon-α/β Impairs Interferon-γ Induction of Nitric Oxide Synthase. *J. Neurochem.* **68,** 2547–2551 (2002).

60. Cross, a H. *et al.* A catalyst of peroxynitrite decomposition inhibits murine experimental autoimmune encephalomyelitis. *J. Neuroimmunol.* **107,** 21–8 (2000).

61. Wuerfel, J. *et al.* Changes in cerebral perfusion precede plaque formation in multiple sclerosis: a longitudinal perfusion MRI study. *Brain* **127,** 111–9 (2004).

62. Chen, Z. & Ma, L. Hyperperfusion of Multiple Sclerosis Plaques Characterized by 3D FSE Arterial Spin Labelling. *Chinese Med. Sci. J.* **29,** 194–196 (2014).

63. Guthikonda, P., Baker, J. & Mattson, D. H. Interferon-beta-1-b (IFN-B) decreases induced nitric oxide (NO) production by a human astrocytoma cell line. *J. Neuroimmunol.* **82,** 133–9 (1998).

64. Javed, A. & Reder, A. T. Therapeutic role of beta-interferons in multiple sclerosis. *Pharmacol. Ther.* **110,** 35–56 (2006).

65. Milo, R. Therapeutic strategies targeting B-cells in multiple sclerosis. *Autoimmun. Rev.* **15,** 714–718 (2016).

66. Attwell, D. & Laughlin, S. B. An Energy Budget for Signaling in the Grey Matter of the Brain. *J. Cereb. Blood Flow Metab.* **21,** 1133–1145 (2001).

67. Zlokovic, B. V. Neurovascular pathways to neurodegeneration in Alzheimer's disease and other disorders. *Nat. Rev. Neurosci.* **12,** 723–38 (2011).

68. Zlokovic, B. V. Neurovascular mechanisms of Alzheimer's neurodegeneration. *Trends Neurosci.* **28,** 202–208 (2005).

69. Moskowitz, M. A., Lo, E. H. & Iadecola, C. The science of stroke: mechanisms in search of treatments. *Neuron* **67,** 181–198 (2010).

70. Miyazaki, K. *et al.* Disruption of neurovascular unit prior to motor neuron degeneration in amyotrophic lateral sclerosis. *J. Neurosci. Res.* **89,** 718–28 (2011).

71. Erinjeri, J. P. & Woolsey, T. A. Spatial Integration of Vascular Changes with Neural Activity in Mouse Cortex. *J. Cereb. Blood Flow Metab.* **22,** 353–360 (2002).

72. Faraci, F. M. & Heistad, D. D. Regulation of large cerebral arteries and cerebral microvascular pressure. *Circ. Res.* **66,** 8–17 (1990).

73. Lou, H. C., Edvinsson, L. & MacKenzie, E. T. The concept of coupling blood flow to brain function: revision required? *Ann. Neurol.* **22,** 289–97 (1987).

74. Bélanger, M., Allaman, I. & Magistretti, P. J. Brain energy metabolism: focus on astrocyte-neuron metabolic cooperation. *Cell Metab.* **14,** 724–38 (2011).

75. Whittaker, J. R., Driver, I. D., Bright, M. G. & Murphy, K. NeuroImage The absolute CBF

response to activation is preserved during elevated perfusion : Implications for neurovascular coupling measures. *Neuroimage* **125,** 198–207 (2016).

76. Driver, X. I. D., Whittaker, X. J. R., Bright, X. M. G., Muthukumaraswamy, S. D. & Murphy, X. K. Arterial CO 2 Fluctuations Modulate Neuronal Rhythmicity : Implications for MEG and fMRI Studies of Resting-State Networks. **36,** 8541–8550 (2016).

77. Xu, F. *et al.* The influence of carbon dioxide on brain activity and metabolism in conscious humans. *J. Cereb. Blood Flow & Metab.* **31,** 58–67 (2010).

78. Maandag, N. J. G. *et al.* Energetics of neuronal signaling and fMRI activity. (2007).

79. Hall, E. L. *et al.* NeuroImage The effect of hypercapnia on resting and stimulus induced MEG signals. *Neuroimage* **58,** 1034–1043 (2011).

80. Dulla, C. G. *et al.* Adenosine and ATP Link P CO 2 to Cortical Excitability via pH. **48,** 1011–1023 (2005).

81. Koehler, R. C., Roman, R. J. & Harder, D. R. Astrocytes and the regulation of cerebral blood flow. *Trends Neurosci.* **32,** 160–9 (2009).

82. Bor-Seng-Shu, E. *et al.* Cerebral hemodynamics: concepts of clinical importance. *Arq. Neuropsiquiatr.* **70,** 352–6 (2012).

83. Quaegebeur, A., Lange, C. & Carmeliet, P. The neurovascular link in health and disease: Molecular mechanisms and therapeutic implications. *Neuron* **71,** 406–424 (2011).

84. Petzold, G. C. & Murthy, V. N. Role of astrocytes in neurovascular coupling. *Neuron* **71,** 782–97 (2011).

85. Filosa, J. A., Morrison, H. W., Iddings, J. A., Du, W. & Kim, K. J. Beyond neurovascular coupling, role of astrocytes in the regulation of vascular tone. *Neuroscience* **323,** 96–109 (2016).

86. Attwell, D. *et al.* Glial and neuronal control of brain blood flow. *Nature* **468,** 232–43 (2010).

87. Lourenco, C. F. *et al.* Neurovascular coupling in hippocampus is mediated via diffusion by neuronal-derived nitric oxide. *Free Radic. Biol. Med.* **73,** 421–429 (2014).

88. Sloan, H. L. *et al.* Regional differences in neurovascular coupling in rat brain as determined by fMRI and electrophysiology. *Neuroimage* **53,** 399–411 (2010).

89. Carmignoto, G. & Gómez-Gonzalo, M. The contribution of astrocyte signalling to neurovascular coupling. *Brain Res. Rev.* **63,** 138–48 (2010).

90. Iadecola, C. Neurovascular regulation in the normal brain and in Alzheimer's disease. *Nat. Rev. Neurosci.* **5,** 347–60 (2004).

91. Devonshire, I. M. *et al.* Neurovascular coupling is brain region-dependent. *Neuroimage* **59,** 1997–2006 (2012).

92. Rap??so, C., Luna, R. L. de A., Nunes, A. K. S., Thom??, R. & Peixoto, C. A. Role of iNOS-NO-cGMP signaling in modulation of inflammatory and myelination processes. *Brain Res. Bull.* **104,** 60–73 (2014).

93. Fathi, A. R. *et al.* Carbon dioxide influence on nitric oxide production in endothelial cells and astrocytes: Cellular mechanisms. *Brain Res.* **1386,** 50–57 (2011).

94. Girouard, H. *et al.* Astrocytic endfoot Ca2+ and BK channels determine both arteriolar dilation and constriction. *Proc. Natl. Acad. Sci. U. S. A.* **107,** 3811–3816 (2010).

95. Zonta, M. *et al.* Neuron-to-astrocyte signaling is central to the dynamic control of brain microcirculation. *Nat Neurosci* **6,** 43–50 (2003).

96. Wang, X. *et al.* Astrocytic Ca2+ signaling evoked by sensory stimulation in vivo. *Nat Neurosci* **9,** 816–823 (2006).

97. Neher, E. & Augustine, G. J. Calcium gradients and buffers in bovine chromaffin cells. *J. Physiol.* **450,** 273–301 (1992).

98. Helmchen, F., Imoto, K. & Sakmann, B. Ca2+ buffering and action potential-evoked Ca2+ signaling in dendrites of pyramidal neurons. *Biophys. J.* **70,** 1069–1081 (1996).

99. Reeves, A. M. B., Shigetomi, E. & Khakh, B. S. Bulk Loading of Calcium Indicator Dyes to Study Astrocyte Physiology: Key Limitations and Improvements Using Morphological Maps. *J. Neurosci.* **31,** 9353–9358 (2011).

100. Chaigneau, E. *et al.* The relationship between blood flow and neuronal activity in the rodent olfactory bulb. *J. Neurosci.* **27,** 6452–6460 (2007).

101. Petzold, G. C., Albeanu, D. F., Sato, T. F. & Murthy, V. N. Coupling of Neural Activity to Blood Flow in Olfactory Glomeruli Is Mediated by Astrocytic Pathways. *Neuron* **58,** 897–910 (2008).

102. Takano, T. *et al.* Astrocyte-mediated control of cerebral blood flow. *Nat Neurosci* **9,** 260–267 (2006).

103. Gordon, G. R. J., Choi, H. B., Ellis-Davies, G. C. R. & Macvicar, B. a. Brain metabolic state dictates the polarity of astrocyte control over the cerebrovasculature. *Nature* **11,** 745–749 (2008).

104. Iadecola, C. & Nedergaard, M. Glial regulation of the cerebral microvasculature. *Nat. Neurosci.* **10,** 1369–1376 (2007).

105. Logothetis, N. K. The neural basis of the blood-oxygen-level-dependent functional magnetic resonance imaging signal. *Philos. Trans. R. Soc. Lond. B. Biol. Sci.* **357,** 1003–37 (2002).

106. Logothetis, N. K. What we can do and what we cannot do with fMRI. *Nature* **453,** 869–78 (2008).

107. Lythgoe, D. J., Williams, S. C. R., Cullinane, M. & Markus, H. S. Mapping of Cerebrovascular Reactivity using BOLD Magnetic Resonance Imaging. *Magn. Reson. Imaging* **17,** 495–502 (1999).

108. Olman, C. A., Ugurbil, K., Schrater, P. & Kersten, D. BOLD fMRI and psychophysical measurements of contrast response to broadband images. *Vision Res.* **44,** 669–683 (2004).

109. Vartiainen, J., Liljestro, M., Koskinen, M., Renvall, H. & Salmelin, R. Functional Magnetic Resonance Imaging Blood Oxygenation Level-Dependent Signal and Magnetoencephalography Reading. *J. Neurosci.* **31,** 1048–1058 (2011).

110. Ogawa, S. *et al.* Functional brain mapping by blood oxygenation level-dependent contrast magnetic resonance imaging. *Biophys. J.* **64,** 803–812 (1993).

111. Buxton, R. B. *et al.* A general kinetic model for quantitative perfusion imaging with arterial spin labeling. *Magn. Reson. Med.* **40,** 383–396 (1998).

112. Tjandra, T. *et al.* Quantitative assessment of the reproducibility of functional activation measured with BOLD and MR perfusion imaging: Implications for clinical trial design. *Neuroimage* **27,** 393–401 (2005).

113. MacIntosh, B. J. *et al.* Assessment of arterial arrival times derived from multiple inversion time pulsed arterial spin labeling MRI. *Magn. Reson. Med.* **63,** 641–647 (2010).

114. Gallichan, D. & Jezzard, P. Modeling the effects of dispersion and pulsatility of blood flow in pulsed arterial spin labeling. *Magn. Reson. Med.* **60,** 53–63 (2008).

115. Sarnthein, J., Andersson, M., Zimmermann, M. B. & Zumsteg, D. High test-retest reliability of checkerboard reversal visual evoked potentials (VEP) over 8 months. *Clin. Neurophysiol.* **120,** 1835–40 (2009).

116. Di Russo, F. *et al.* Identification of the neural sources of the pattern-reversal VEP. *Neuroimage* **24,** 874–86 (2005).

117. Janz, C., Heinrich, S. P., Kornmayer, J., Bach, M. & Hennig, J. Coupling of neural activity and BOLD fMRI response: New insights by combination of fMRI and VEP experiments in transition from single events to continuous stimulation. *Magn. Reson. Med.* **46,** 482–486 (2001).

118. Schadow, J. *et al.* Stimulus intensity affects early sensory processing: visual contrast modulates evoked gamma-band activity in human EEG. *Int. J. Psychophysiol.* **66,** 28–36 (2007).

119. Hall, E. L., Robson, S. E., Morris, P. G. & Brookes, M. J. The relationship between MEG and fMRI. *Neuroimage* (2014). doi:10.1016/j.neuroimage.2013.11.005

120. Muthukumaraswamy, S. D. Temporal dynamics of primary motor cortex γ oscillation amplitude and piper corticomuscular coherence changes during motor control. *Exp. Brain Res.* **212,** 623–33 (2011).

121. Perry, G., Hamandi, K., Brindley, L. M., Muthukumaraswamy, S. D. & Singh, K. D. The properties of induced gamma oscillations in human visual cortex show individual variability in their dependence on stimulus size. *Neuroimage* **68,** 83–92 (2013).

122. Muthukumaraswamy, S. D. & Singh, K. D. Functional decoupling of BOLD and gamma-band amplitudes in human primary visual cortex. *Hum. Brain Mapp.* **30,** 2000–7 (2009).

123. Singh, K. D., Barnes, G. R., Hillebrand, A., Forde, E. M. E. & Williams, A. L. Task-Related Changes in Cortical Synchronization Are Spatially Coincident with the Hemodynamic Response. **114,** 103–114 (2002).

124. Winterer, G. *et al.* Complex relationship between BOLD signal and synchronization/desynchronization of human brain MEG oscillations. *Hum. Brain Mapp.* **28,** 805–16 (2007).

125. Muthukumaraswamy, S. D., Singh, K. D., Swettenham, J. B. & Jones, D. K. Visual gamma oscillations and evoked responses: Variability, repeatability and structural MRI correlates. *Neuroimage* **49,** 3349–3357 (2010).

126. Chiacchiaretta, P., Romani, G. L. & Ferretti, A. Sensitivity of BOLD response to increasing visual contrast: spin echo versus gradient echo EPI. *Neuroimage* **82,** 35–43 (2013).

127. Ray, S. & Maunsell, J. H. R. Different origins of gamma rhythm and high-gamma activity in macaque visual cortex. *PLoS Biol.* **9,** e1000610 (2011).

128. Hadjipapas, A., Lowet, E., Roberts, M. J., Peter, A. & De Weerd, P. Parametric variation of gamma frequency and power with luminance contrast: A comparative study of human MEG and monkey LFP and spike responses. *Neuroimage* **112,** 327–340 (2015).

129. Kayser, C., Kim, M., Ugurbil, K. & König, P. A Comparison of Hemodynamic and Neural

Responses in Cat Visual Cortex Using Complex Stimuli. 881–891 (2004). doi:10.1093/cercor/bhh047

130. Brookes, M. J. *et al.* GLM-beamformer method demonstrates stationary field, alpha ERD and gamma ERS co-localisation with fMRI BOLD response in visual cortex. *Neuroimage* **26,** 302–308 (2005).

131. Stevenson, C. M., Brookes, M. J. & Morris, P. G. β-Band correlates of the fMRI BOLD response. *Hum. Brain Mapp.* **32,** 182–97 (2011).

132. Stancák, A. & Pfurtscheller, G. Desynchronization and recovery of beta rhythms during brisk and slow self-paced finger movements in man. *Neurosci. Lett.* **196,** 21–24 (1995).

133. Pfurtscheller, G., Zalaudek, K. & Neuper, C. Event-related beta synchronization after wrist, finger and thumb movement. *Electroencephalogr. Clin. Neurophysiol.* **109,** 154–60 (1998).

134. Lachaux, J. P. *et al.* Relationship between task-related gamma oscillations and BOLD Signal: New insights from combined fMRI and intracranial EEG. *Hum. Brain Mapp.* **28,** 1368–1375 (2007).

135. Swettenham, J. B., Muthukumaraswamy, S. D. & Singh, K. D. BOLD Responses in Human Primary Visual Cortex are Insensitive to Substantial Changes in Neural Activity. *Front. Hum. Neurosci.* **7,** 76 (2013).

136. Yamagishi, N. *et al.* Attentional modulation of oscillatory activity in human visual cortex. *Neuroimage* **20,** 98–113 (2003).

137. Lennert, T., Cipriani, R., Jolicoeur, P., Cheyne, D. & Martinez-Trujillo, J. C. Attentional modulation of neuromagnetic evoked responses in early human visual cortex and parietal lobe following a rank-order rule. *J. Neurosci.* **31,** 17622–36 (2011).

138. Tiesinga, P. & Sejnowski, T. J. Cortical Enlightenment : Are Attentional Gamma Oscillations Driven by ING or PING ? **63,** 727–732 (2009).

139. Whittington, M. A., Cunningham, M. O., LeBeau, F. E. N., Racca, C. & Traub, R. D. Multiple origins of the cortical gamma rhythm. *Dev. Neurobiol.* **71,** 92–106 (2011).

140. Bartos, M., Vida, I. & Jonas, P. Synaptic mechanisms of synchronized gamma oscillations in inhibitory interneuron networks. *Nat Rev Neurosci* **8,** 45–56 (2007).

141. Hillebrand, A., Singh, K. D., Holliday, I. E., Furlong, P. L. & Barnes, G. R. A new approach to neuroimaging with magnetoencephalography. *Human Brain Mapping* **25,** 199–211 (2005).

142. Vrba, J. & Robinson, S. E. Signal processing in magnetoencephalography. *Methods* **25,** 249–71 (2001).

143. Hari, R. & Salmelin, R. Magnetoencephalography: From SQUIDs to neuroscience. Neuroimage 20th Anniversary Special Edition. *Neuroimage* **61,** 386–396 (2012).

144. Brookes, M. J. *et al.* Optimising experimental design for MEG beamformer imaging. *Neuroimage* **39,** 1788–1802 (2008).

145. Marshall, O. *et al.* Impaired Cerebrovascular Reactivity in Multiple Sclerosis. *JAMA Neurol.* **10016,** 1–7 (2014).

146. Carrera, E., Lee, L. K., Giannopoulos, S. & Marshall, R. S. Cerebrovascular reactivity and cerebral autoregulation in normal subjects. *J. Neurol. Sci.* **285,** 191–4 (2009).

147. Cader, S., Cifelli, A., Abu-Omar, Y., Palace, J. & Matthews, P. M. Reduced brain functional

reserve and altered functional connectivity in patients with multiple sclerosis. *Brain* **129,** 527–37 (2006).

148. Lavi, S., Gaitini, D., Milloul, V. & Jacob, G. Impaired cerebral CO2 vasoreactivity: association with endothelial dysfunction. *Am. J. Physiol. Heart Circ. Physiol.* **291,** H1856–H1861 (2006).

149. Alexander, J. S. *et al.* Multiple sclerosis and cerebral endothelial dysfunction: Mechanisms. *Pathophysiology* **18,** 3–12 (2011).

150. D'haeseleer, M., Cambron, M., Vanopdenbosch, L. & De Keyser, J. Vascular aspects of multiple sclerosis. *Lancet Neurol.* **10,** 657–66 (2011).

151. Kastrup, a, Krüger, G., Neumann-Haefelin, T. & Moseley, M. E. Assessment of cerebrovascular reactivity with functional magnetic resonance imaging: comparison of CO(2) and breath holding. *Magn. Reson. Imaging* **19,** 13–20 (2001).

152. Murphy, K., Harris, A. D. & Wise, R. G. Robustly measuring vascular reactivity differences with breath-hold: Normalising stimulus-evoked and resting state BOLD fMRI data. *Neuroimage* **54,** 369–379 (2011).

153. Smith, S. M. *et al.* Advances in functional and structural MR image analysis and implementation as FSL. *Neuroimage* **23 Suppl 1,** S208-19 (2004).

154. Jenkinson, M., Bannister, P., Brady, M. & Smith, S. Improved Optimization for the Robust and Accurate Linear Registration and Motion Correction of Brain Images. *Neuroimage* **17,** 825–841 (2002).

155. Smith, S. M. Robust automated brain extraction. *Neuroimage* **11,** S625 (2000).

156. Smith, S. M. *et al.* Advances in functional and structural MR image analysis and implementation as FSL. *Neuroimage* **23 Suppl 1,** S208-19 (2004).

157. Douaud, G. *et al.* Anatomically related grey and white matter abnormalities in adolescent-onset schizophrenia. *Brain* **130,** 2375–86 (2007).

158. Good, C. D. *et al.* A voxel-based morphometric study of ageing in 465 normal adult human brains. *Neuroimage* **14,** 21–36 (2001).

159. Smith, S. M. *et al.* Tract-based spatial statistics: voxelwise analysis of multi-subject diffusion data. *Neuroimage* **31,** 1487–505 (2006).

160. Smith, S. M. *et al.* Accurate, Robust, and Automated Longitudinal and Cross-Sectional Brain Change Analysis. *Neuroimage* **17,** 479–489 (2002).

161. De Stefano, N. *et al.* Efficacy and safety of subcutaneous interferon β-1a in relapsing-remitting multiple sclerosis: further outcomes from the IMPROVE study. *J. Neurol. Sci.* **312,** 97–101 (2012).

162. Vercellino, M. *et al.* Grey matter pathology in multiple sclerosis. *Acta Neurol. Scand. Suppl.* **183,** 48–50 (2006).

163. Bogdan, C. Nitric oxide and the immune response. *Nat. Immunol.* **2,** 907–16 (2001).

164. Danilov, A. I. *et al.* Nitric oxide metabolite determinations reveal continuous inflammation in multiple sclerosis. *J. Neuroimmunol.* **136,** 112–118 (2003).

165. Ota, M. *et al.* Abnormalities of cerebral blood flow in multiple sclerosis: A pseudocontinuous arterial spin labeling MRI study. *Magn. Reson. Imaging* (2013). doi:10.1016/j.mri.2013.03.016

166. Smith, J. J. *et al.* The role of nitric oxide in the cerebrovascular response to hypercapnia. *Anesth. Analg.* **84,** 363–369 (1997).

167. Ziemann, U., Wahl, M., Hattingen, E. & Tumani, H. Development of biomarkers for multiple sclerosis as a neurodegenerative disorder. *Prog. Neurobiol.* **95,** 670–85 (2011).

168. Sury, M. D. *et al.* Evidence that N-acetylcysteine inhibits TNF-alpha-induced cerebrovascular endothelin-1 upregulation via inhibition of mitogen- and stress-activated protein kinase. *Free Radic. Biol. Med.* **41,** 1372–83 (2006).

169. Guo, F. H. *et al.* Interferon gamma and interleukin 4 stimulate prolonged expression of inducible nitric oxide synthase in human airway epithelium through synthesis of soluble mediators. *J. Clin. Invest.* **100,** 829–38 (1997).

170. Lecrux, C. & Hamel, E. The neurovascular unit in brain function and disease. *Acta Physiol.* **203,** 47–59 (2011).

171. Liang, C. L. *et al.* Luminance contrast of a visual stimulus modulates the BOLD response more than the cerebral blood flow response in the human brain. *Neuroimage* **64,** 104–11 (2013).

172. Diem, R., Tschirne, a & Bähr, M. Decreased amplitudes in multiple sclerosis patients with normal visual acuity: a VEP study. *J. Clin. Neurosci.* **10,** 67–70 (2003).

173. Walsh, J. C., Garrick, R., Cameron, J. & McLeod, J. G. Evoked potential changes in clinically definite multiple sclerosis: a two year follow up study. *J. Neurol. Neurosurg. Psychiatry* **45,** 494–500 (1982).

174. Ghilardi, M. F. *et al.* N70 and P100 can be independently affected in multiple sclerosis. *Electroencephalogr. Clin. Neurophysiol.* **80,** 1–7 (1991).

175. Nakamura, a *et al.* Visual evoked cortical magnetic fields to pattern reversal stimulation. *Brain Res. Cogn. Brain Res.* **6,** 9–22 (1997).

176. Mellow, T. B., Liasis, A., Lyons, R. & Thompson, D. a. The reproducibility of binocular pattern reversal visual evoked potentials: a single subject design. *Doc. Ophthalmol.* **122,** 133–9 (2011).

177. Shors, T. J., Ary, J. P., Eriksen, J. & Wright, jenneth W. P100 Amplitude variability of the pattern visual evoked potential. *Electroencephalogr. Clin. Neurophysiol.* **65,** 316–319 (1986).

178. Di Russo, F., Martinez, A., Sereno, M. I., Pitzalis, S. & Hillyard, S. A. Cortical sources of the early components of the visual evoked potential. *Hum. Brain Mapp.* **15,** 95–111 (2002).

179. Franceschini, M. A. *et al.* Coupling between somatosensory evoked potentials and hemodynamic response in the rat. *Neuroimage* **41,** 189–203 (2008).

180. Mayhew, S. D., Macintosh, B. J., Dirckx, S. G., Iannetti, G. D. & Wise, R. G. Coupling of simultaneously acquired electrophysiological and haemodynamic responses during visual stimulation. *Magn. Reson. Imaging* **28,** 1066–77 (2010).

181. Kwong, K. K. *et al.* Dynamic magnetic resonance imaging of human brain activity during primary sensory stimulation. *Proc. Natl. Acad. Sci. U. S. A.* **89,** 5675–9 (1992).

182. Gauthier, C. J., Madjar, C., Tancredi, F. B., Stefanovic, B. & Hoge, R. D. Elimination of visually evoked BOLD responses during carbogen inhalation: implications for calibrated MRI. *Neuroimage* **54,** 1001–11 (2011).

183. Nakamura, M., Kakigi, R., Okusa, T., Hoshiyama, M. & Watanabe, K. Effects of check size on

pattern reversal visual evoked magnetic field and potential. *Brain Res.* **872,** 77–86 (2000).

184. Tobimatsu, S. Transient and steady-state VEPs—reappraisal. *Int. Congr. Ser.* **1232,** 207–211 (2002).

185. Muthukumaraswamy, S. D., Singh, K. D., Swettenham, J. B. & Jones, D. K. Visual gamma oscillations and evoked responses: variability, repeatability and structural MRI correlates. *Neuroimage* **49,** 3349–57 (2010).

186. Muthukumaraswamy, S. D. & Singh, K. D. Visual gamma oscillations: the effects of stimulus type, visual field coverage and stimulus motion on MEG and EEG recordings. *Neuroimage* **69,** 223–30 (2013).

187. Perry, G., Randle, J. M., Koelewijn, L., Routley, B. C. & Singh, K. D. Linear Tuning of Gamma Amplitude and Frequency to Luminance Contrast: Evidence from a Continuous Mapping Paradigm. *PLoS One* **10,** e0124798 (2015).

188. Koelewijn, L., Dumont, J. R., Muthukumaraswamy, S. D., Rich, A. N. & Singh, K. D. Induced and evoked neural correlates of orientation selectivity in human visual cortex. *Neuroimage* **54,** 2983–93 (2011).

189. Wong, E. C., Buxton, R. B. & Frank, L. R. Quantitative imaging of perfusion using a single subtraction (QUIPSS and QUIPSS II). *Magn. Reson. Med.* **39,** 702–708 (1998).

190. Muthukumaraswamy, S. D. & Singh, K. D. Modulation of the human mirror neuron system during cognitive activity. *Psychophysiology* **45,** 896–905 (2008).

191. Oostenveld, R., Fries, P., Maris, E. & Schoffelen, J.-M. FieldTrip: Open source software for advanced analysis of MEG, EEG, and invasive electrophysiological data. *Comput. Intell. Neurosci.* **2011,** 156869 (2011).

192. Glover, G. H., Li, T. Q. & Ress, D. Image-based method for retrospective correction of physiological motion effects in fMRI: RETROICOR. *Magn. Reson. Med.* **44,** 162–7 (2000).

193. Birn, R. M., Murphy, K., Handwerker, D. a & Bandettini, P. a. fMRI in the presence of task-correlated breathing variations. *Neuroimage* **47,** 1092–104 (2009).

194. Liu, T. T. & Wong, E. C. A signal processing model for arterial spin labeling functional MRI. *Neuroimage* **24,** 207–15 (2005).

195. Souza, G. S., Gomes, B. D., Saito, C. a, da Silva Filho, M. & Silveira, L. C. L. Spatial luminance contrast sensitivity measured with transient VEP: comparison with psychophysics and evidence of multiple mechanisms. *Invest. Ophthalmol. Vis. Sci.* **48,** 3396–404 (2007).

196. Perry, G. *et al.* Retinotopic mapping of the primary visual cortex - a challenge for MEG imaging of the human cortex. *Eur. J. Neurosci.* **34,** 652–661 (2011).

197. Chappell, M. a. *et al.* Separation of macrovascular signal in multi-inversion time arterial spin labelling MRI. *Magn. Reson. Med.* **63,** 1357–1365 (2010).

198. Warnert, E. A. *et al.* In vivo assessment of human brainstem cerebrovascular function: a multi-inversion time pulsed arterial spin labelling study. *J. Cereb. Blood Flow Metab.* **34,** 1–8 (2014).

199. Huang, M. X., Mosher, J. C. & Leahy, R. M. A sensor-weighted overlapping-sphere head model and exhaustive head model comparison for MEG. *Phys. Med. Biol* **44,** 423–440 (1999).

200. Gottesman, J., Rubin, G. S. & Legge, G. E. A power law for perceived contrast in human vision.

Vision Res. **21,** 791–9 (1981).

201. Shrout, P. E. & Fleiss, J. L. Intraclass correlations: uses in assessing rater reliability. *Psychol. Bull.* **86,** 420–428 (1979).

202. Ludbrook, J. Multiple comparison procedures updated. *Clin. Exp. Pharmacol. Physiol.* **25,** 1032–7 (1998).

203. Obrig, H. *et al.* Habituation of the visually evoked potential and its vascular response: implications for neurovascular coupling in the healthy adult. *Neuroimage* **17,** 1–18 (2002).

204. Cohen, E. R., Ugurbil, K. & Kim, S.-G. Effect of basal conditions on the magnitude and dynamics of the blood oxygenation level-dependent fMRI response. *J. Cereb. Blood Flow Metab.* **22,** 1042–53 (2002).

205. Tobimatsu, S. & Celesia, G. G. Studies of human visual pathophysiology with visual evoked potentials. *Clin. Neurophysiol.* **117,** 1414–33 (2006).

206. Fabiani, M. *et al.* Neurovascular coupling in normal aging: A combined optical, ERP and fMRI study. *Neuroimage* **85,** 592–607 (2014).

207. Wan, X. *et al.* The neural basis of the hemodynamic response nonlinearity in human primary visual cortex: Implications for neurovascular coupling mechanism. *Neuroimage* **32,** 616–625 (2006).

208. Xing, D. No Consistent Relationship between Gamma Power and Peak Frequency in Macaque Primary Visual Cortex.pdf. *J. Neurosci.* **33,** 17–25 (2013).

209. Juurlink, B. H. J. The evidence for hypoperfusion as a factor in multiple sclerosis lesion development. *Mult. Scler. Int.* **2013,** 598093 (2013).

210. McPherson, R. W., Kirsch, J. R., Ghaly, R. F. & Traystman, R. J. Effect of Nitric Oxide Synthase Inhibition on the Cerebral Vascular Response to Hypercapnia in Primates. *Stroke* **26,** 682–687 (1995).

211. Hickman, S. J., Raoof, N., McLean, R. J. & Gottlob, I. Vision and multiple sclerosis. *Mult. Scler. Relat. Disord.* **3,** 3–16 (2014).

212. Comi, G. *et al.* Measuring evoked responses in multiple sclerosis. *Mult. Scler.* **5,** 263–267 (1999).

213. Galetta, K. M. & Balcer, L. J. Measures of visual pathway structure and function in MS: Clinical usefulness and role for MS trials. *Mult. Scler. Relat. Disord.* **2,** 172–182 (2013).

214. Filep, J. G., Földes-Filep, E., Rousseau, A., Sirois, P. & Fournier, A. Vascular responses to endothelin-1 following inhibition of nitric oxide synthesis in the conscious rat. *Br. J. Pharmacol.* **110,** 1213–1221 (1993).

215. Hall, S. D. *et al.* The role of GABAergic modulation in motor function related neuronal network activity. *Neuroimage* **56,** 1506–10 (2011).

216. Marshall, O., Chawla, S., Lu, H., Pape, L. & Ge, Y. Cerebral blood flow modulation insufficiency in brain networks in multiple sclerosis: A hypercapnia MRI study. *J. Cereb. Blood Flow Metab.* (2016). doi:10.1177/0271678X16654922

217. Kim SG, Rostrup E, Larsson HB, Ogawa S, P. O. Determination of relative CMRO2 from CBF and BOLD changes: significant increase of oxygen consumption rate during visual stimulation. *Magn Reson Med* **41,** 1152–1161 (1999).

218. Tuan, A. S., Birn, R. M., Bandettini, P. a. & Boynton, G. M. Differential transient MEG and fMRI responses to visual stimulation onset rate. *Int. J. Imaging Syst. Technol.* **18,** 17–28 (2008).

219. Barnikol, U. B. *et al.* Pattern reversal visual evoked responses of V1/V2 and V5/MT as revealed by MEG combined with probabilistic cytoarchitectonic maps. *Neuroimage* **31,** 86–108 (2006).

220. Tobimatsu, S., Kurita-Tashima, S., Nakayama-Hiromatsu, M. & Kato, M. Effect of spatial frequency on transient and steady-state VEPs: stimulation with checkerboard, square-wave grating and sinusoidal grating patterns. *J. Neurol. Sci.* **118,** 17–24 (1993).

221. Tobimatsu, S., Tomoda, H. & Kato, M. Normal variability of the amplitude and phase of steady-state VEPs. *Electroencephalogr. Clin. Neurophysiol.* **100,** 171–6 (1996).

222. Uzuner, N., Özkan, S., Gücüyener, D. & Özdemir, G. Cerebral blood flow velocity changes to visual stimuli in patients with multiple sclerosis. *Mult. Scler.* **8,** 217–221 (2002).

223. Vieira-Gutemberg, J. G., Mendes-Santos, L. C., Cavalcanti-Galdino, M. K., Santos, N. a & DE Bustamante Simas, M. L. Contrast sensitivity in relapsing-remitting multiple sclerosis assessed by sine-wave gratings and angular frequency stimuli. *Vis. Neurosci.* 1–6 (2014). doi:10.1017/S0952523814000182

224. Tekgol Uzuner, G. & Uzuner, N. Neurovascular coupling in patients with relapsing-remitting multiple sclerosis. *Clin. Neurol. Neurosurg.* **146,** 24–28 (2016).

225. Arthurs, O. J., Williams, E. J., Carpenter, T. A., Pickard, J. D. & Boniface, S. J. Linear Coupling Between Functional Magnetic Resonance Imaging and Evoked Potential Amplitude in Human Somatosensory Cortex. *Science (80-.).* **106,** 653–658 (2001).

226. Bartolo, M. J. *et al.* Stimulus-induced dissociation of neuronal firing rates and local field potential gamma power and its relationship to the resonance blood oxygen level-dependent signal in macaque primary visual cortex. *Eur. J. Neurosci.* **34,** 1857–1870 (2011).

227. Willie, C. K., Tzeng, Y.-C., Fisher, J. a & Ainslie, P. N. Integrative regulation of human brain blood flow. *J. Physiol.* **592,** 841–59 (2014).